REPORT DOCUMENTATION PAGE

The public reporting burden for this collection of information is estimated to average 1 hour per response, including the time for reviewing instructions, searching existing data sources, gathering and maintaining the data needed, and completing and reviewing the collection of information. Send comments regarding this burden estimate or any other aspect of this collection of information, including suggestions for reducing the burden, to the Department of Defense, Executive Service Directorate (0704-0188). Respondents should be aware that notwithstanding any other provision of law, no person shall be subject to any penalty for failing to comply with a collection of information if it does not display a currently valid OMB control number.

PLEASE DO NOT RETURN YOUR FORM TO THE ABOVE ORGANIZATION.

1. REPORT DATE (DD-MM-YYYY)	2. REPORT TYPE	3. DATES COVERED (From - To)
30-09-2008	Final	March 2005- June 2008

4. TITLE AND SUBTITLE
Statistical Methods for Turbine Blade Dynamics

5a. CONTRACT NUMBER

5b. GRANT NUMBER
FA9550-05-1-0149

5c. PROGRAM ELEMENT NUMBER

6. AUTHOR(S)
Volovoi, Vitali and Ruzzene, Massimo

5d. PROJECT NUMBER
1606Y05

5e. TASK NUMBER

5f. WORK UNIT NUMBER

7. PERFORMING ORGANIZATION NAME(S) AND ADDRESS(ES)
School of Aerospace Engineering,
Georgia Institute of Technology
Atlanta, GA 30332-0150

8. PERFORMING ORGANIZATION REPORT NUMBER
99806

9. SPONSORING/MONITORING AGENCY NAME(S) AND ADDRESS(ES)
Victor Giurgiutiu PhD FRAeS F.ASME
Structural Mechanics program manager
Air Force Office of Scientific Research (AFOSR)
875 N. Randolph St., Arlington, VA 22203

10. SPONSOR/MONITOR'S ACRONYM(S)

11. SPONSOR/MONITOR'S REPORT NUM AFRL-OSR-VA-TR-2013-0920

12. DISTRIBUTION/AVAILABILITY STATEMENT
Distribution Statement A: approved for public release. Distribution is unlimited

13. SUPPLEMENTARY NOTES
20130918427

14. ABSTRACT
A novel statistical methodology has been designed aimed at quantification of uncertainties embedded in stress/strain prediction of structural performance for turbine engine blades. The developed methodology relies on Bayesian network representation of existing model-based stress/strain predictions that use both analytical/numerical modal information and experimental forced-response data. It accounts in a statistically consistent fashion for the evidence provided both at the input and output levels of the model. The need to incorporate the evidence at the output level is not unique to the considered problem, so the results can be applicable to other fields, such as system identification and model calibration. In addition, various sources of uncertainty were analyzed, namely component geometric and material properties, sensor-induced and data-processing errors. Simulation of uncertainty propagation and sensitivity analyses were conducted to identify the main uncertainty contributors and provide the guidelines for simplifying the Bayesian network. Assessment of the proposed framework and identification of its benefits and drawbacks were performed using experimental data for plate structures obtained using the industry-standard testing procedures for turbine engine blade analysis.

15. SUBJECT TERMS

16. SECURITY CLASSIFICATION OF:			17. LIMITATION OF ABSTRACT	18. NUMBER OF PAGES	19a. NAME OF RESPONSIBLE PERSON
a. REPORT	b. ABSTRACT	c. THIS PAGE			
U	U	U			19b. TELEPHONE NUMBER (Include area code)

Executive Summary

A novel statistical methodology has been designed and investigated. It is aimed at quantification of uncertainties embedded in stress/strain prediction used for structural performance assessment of turbine engine blades. The developed methodology relies on Bayesian belief network representation of existing model-based inference schemes for stress/strain prediction that use both analytical/numerical modal information and experimental forced-response data. It accounts in a statistically consistent fashion for the evidence provided both at the input and output levels of the model. The need to incorporate the evidence at the output level is not unique to the considered problem, so the results can be applicable to other fields, such as system identification and model calibration. In addition, various sources of uncertainty were analyzed, namely component geometric and material properties, sensor-induced errors, data-processing assumptions and parameters. Simulation of uncertainty propagation and sensitivity analyses were conducted to identify the main contributors to uncertainty and provide the guidelines for problem downsizing, both computationally and in terms of the corresponding Bayesian network complexity. Assessment of the proposed statistical framework and identification of its benefits and drawbacks were performed using experimental data for plate structures obtained using the industry-standard testing procedures employed for turbine engine blade analysis. The developed procedures and the improved modeling tools provide a means for uncertainty estimation and reduction, which leads to more accurate stress predictions, as well as guidelines for improvement in instrumentation strategies (e.g., reduction of instrumentation and number of sensors without compromising the fidelity).

Overview of the original proposed tasks and their completion

Task 1: Model development and validation
The reduced order models for the blade and disk assembly have been developed. A simple model based on analytical beam representation of individual blades has been be prepared and used for initial statistical analysis. Upgrades to the model will be then completed to include complex blade geometries and higher order effects. The model has been validated against detailed FE models of bladed disk assemblies. The validated reduced order models have used to construct stress uncertainty estimation models. The detailed FE models have been used as a reference to check for modeling accuracy (see Appendix for full results)

Task 2: Evaluation of uncertainty sources and their sensitivity to uncertainty
The models developed during Task 1 have been used to identify and classify the sources of uncertainty. The task will be supported by an extensive literature search, aimed also at characterizing or eliminating parameters affected by uncertainty. The sensitivity of the sources of uncertainty on stress predictions has been evaluated (see Appendix for full results)

Task 3: Development of uncertainty evaluation process
The objective of this research has been to quantify the level of accuracy within a standard model-based estimation scheme for the calculation of the maximum vibratory response in dynamic structures. For any given physical system being investigated, this inference technique relies on two essential contributors: an analytical model of the system and actual experimentation, both of which are inevitably affected by uncertainties and errors in their results. In order to characterize the statistical interaction between these two contributors and assess the predictive accuracy of the estimation procedure, a structured statistical framework has been developed by means of a Bayesian-network representation of the inference scheme itself. This approach allows for multi-directional propagation and updating of uncertainty, as well as knowledge infusion from available

sources of information at various levels of the analysis. In order to construct the Bayesian network, a simulated-experiment environment equivalent to the procedures used for actual systems was created, where equivalency in this setting implies comparable levels of results' variability and correlation between the physical system and its model. Sensitivity analyses conducted through direct propagation of uncertainty were utilized to identify key uncertainty sources to be included in the network, whether they were the true causes of the variability observed in the actual experiments or a suitable set of surrogate explanatory ones. Finally, uncertainty sources associated with system/model correlation, model parameters, and measurement sensors were modeled probabilistically and integrated in a unified fashion within the network.

The methodology was tested on two structures, a one-dimensional beam and a three-dimensional plate, with results that proved to be promising in light of the assumptions embedded in the process. In fact, in the presence of a limited set of actual test data upon which it may be difficult to draw strong statistical conclusions, the developed Bayesian approach was shown to provide a means to quantify comprehensively the uncertainty in the response estimates based simply upon additional simulated experiments. The level of confidence in the estimated quantities can be assessed and quantified more satisfactorily upon the inclusion of real information from the sensors, a task that the Bayesian-network approach allows to be performed coherently.

Summary of Specific Findings and Conclusions

The scope of this work lies within the realm of methodologies employed in building analytical models for the purpose of system performance prediction. Among the host of potential models, two main distinct categories can be identified: physics-based models and data-driven ones. On the one hand, the former are built upon first principles, and their verification and validation are usually executed as a separate task of reconciliation with appropriate test data. On the other hand, the latter consist of data-based meta-models which may not be derived from physics-based considerations. This second type of system representation lends itself easily to statistical validation, assuming that a large set of relevant data is available, which might or might not be the case. In the presence of these distinct engineering approaches, a need has been identified for a way to integrate experimental and model information capable of addressing the intermediate scenarios and quantifying any residual uncertainty, thus combining the best features of both approaches by relying on the physics-based models and yet allowing for a statistically rigorous incorporation of the evidence into the model. In the field of system identification the problem of model-to-data correlation has been addressed both in a deterministic and a statistical fashion. The contribution of the present research consists of investigating the use of Bayesian networks as a possible means to bridge the gap between physics-based and data-driven approaches and applied to a particular structural-dynamics application where model and experimental data are used concomitantly for the purpose of response prediction. In this context, the Bayesian network itself can be viewed as a statistical surrogate model of the prediction scheme, relating the uncertainty embedded in the estimates to the changing level of available knowledge.

The high complexity of certain structural systems makes the identification and characterizationof the sources of uncertainty embedded in them an involved task which may result in a rather large state space to be modeled within a statistical framework such as a Bayesian network. Therefore, sensitivity studies and network Gaussian-linear statistics were adopted to address the dimensionality issue as well as manage the computational burden. Sensitivity analysis was used to downsize the Bayesian network to its essential elements by means of pinpointing key explanatory factors of uncertainty and discarding quantities responsible for weak causal relationships. Case studies on these scenarios demonstrated that the presence of such quantities causes unnecessary additional topological complexity and may hamper the effect of evidence infusion because of localized insensitivity of the given network.

The assumption of linear Gaussian cause-effect relationships permits, instead, to solve for uncertainty quantification in closed form, with consequent computational savings. As with any modeling technique, however, the analytical simplifications do bound the range of applicability and validity for the proposed framework. More specifically, it may become impossible to model non-linearities using a linear network if the noise level introduced by the linearization process and due to underfitting issues outweighs the impact of any other uncertainty source; or the quantities being modeled may be highly non-Gaussian so that the first two statistical moments become insufficient to fully characterize their probabilistic nature. This loss of accuracy and information could be significantly reduced by appropriately transforming the original variables, derived from physics-based considerations, and consequently using the results of these transformations to construct the Bayesian network. As an example, the logarithmic transformation was suggested because it eliminates the source of non-linearity from the estimation product formula, and may prove beneficial if the gain in accuracy exceeds the consequent loss of probabilistic information due to treating the newly log-transformed quantities as Gaussian random variables. The use of other transformations (e.g., the Rosenblatt transformation or variations of it) could be envisioned to address this last issue.

The effect of evidence infusion led to the discovery of interesting behaviors of the network. Evidence in the form of peak frequency and peak amplitudes was chosen for this type of model-based response prediction in accordance with the existing industrial practice. The effectiveness of the propagation of evidence at a node was observed to be dependent on two important factors: the causal strength of connecting links, and the level of separation between the observed node and a given queried one. As a result of this evidence attenuation, both pieces of measured information on peak frequency and peak response amplitudes were found to be essential for a satisfactory update of the entire network. Furthermore, even with multiple inclusions of evidence, the network was not always able to pinpoint the assumed true state of all the nodes, even though its updated state was indeed consistent with the infused information. This behavior is deemed to originate primarily from the issue of solution non-uniqueness typically encountered when addressing inverse problems (See Appendix for more details)

Impact of the research

The proposed research provides the means for a time and cost effective analysis and interpretation of the test data, by including statistic and uncertainty measures inherently with the models. The outcome of the conducted approach is multifold. First of all, the developed procedure facilitates the identification of vibratory modes and provides information regarding their variations as a result of changes in the most influential parameters (rotor speed, operating temperature, manufacturing tolerances on blades, material properties, etc.). Correct modal identification is the required prerequisite for correct estimation of SAFs and the prediction of the durability of the blade. Moreover, the estimation of uncertainty on estimated and test data facilitate the identification of "rogue blade" responses, caused for example by mistuning phenomena, and to quantify blade-to-blade as well as engine-to-engine variations. The statistically-based model could also be used to isolate statistical outliers, corresponding for example to the stress levels in highly defective or damaged blades. Future developments of the methodology could therefore be coupled with damage detection techniques for turbine bladed-disk. Furthermore, the analysis of the sensitivity to sources of uncertainty can naturally lead to improved testing procedures, whereby the test articles can be exposed to a statistically significant portion of all the controllable influence parameters (e.g. rotor speed, operating temperatures). Finally, the developed modeling approach could be employed as a guide to the reduction of the number of sensors required for durability estimations, and to the improvement of current sensor placement strategies.

Personal involved and Interactions with Arnold Engineering Development Center (AEDC)

Georgia Tech Professors (co-PIs): Vitali Volovoi and Massimo Ruzzene
Graduate Research Assistant: Giorgio Callani (Ph D completed in July 2008 – see Appendix)
AEDC: Rob W. McAmis, Peter F. Cento, Charles Vining, Tom Tibbals

The successful completion of the project relied on the availability of test data on which the proposed methodology can be tested and applied. A close collaboration with the Turbine Engine Test and Evaluation group from the Arnold Engineering Development Center (AEDC) at Arnold Air Force Base has been established to share data and results from the project. Constant communication between Georgia Tech and the AEDC group ensured that the project findings are immediately available for application to test data. Guidance has been sought from the AEDC group during the project for fine tuning the model and the statistical approach, with the objective of reducing the transition time for the developed technology.

Publications

Calanni, G., Ruzzene, M., Volovoi, V., Cento, P. , Vining, C. (2008) Assessment of uncertainty in response estimation for turbine engine bladed disks *Journal of Sound and Vibration* 317 , pp. 625-645.

Calanni, G., Volovoi, V., Ruzzene, M., Vining, C. , Cento, P., (2007). Application of Bayesian Belief Nets for Modeling Uncertainty in Structural Dynamics. Proceedings of GT2007 ASME Turbo Expo 2007: Power for Land, Sea and Air, May 14-17, 2007, Montreal, Canada, v 5, pp. 1135-1149 Paper No. GT2007-27684.

Calanni, G., Ruzzene, M., Volovoi, V., Cento, P., Tibbals, T. Vining, C. (2007) Investigation of Sources of Uncertainty in Stress Prediction in Dynamic Structures. Proceedings of the 48th AIAA/ASME/ASCE/AHS/ASC Structures, Structural Dynamics, and Materials Conference, April 23-27, 2007, Honolulu, Hawaii, pp. 3181-3196

Calanni, G., Volovoi, V., Ruzzene, M., , Cento, P., Vining, C. (2006). Quantification of uncertainty related to stress estimation in turbine engine blades. Proceedings of GT2006 ASME Turbo Expo 2007: Power for Land, Sea and Air, May 8-11, 2006, Barselona, Spain, v 5 PART A, pp. 681-690

Appendix A

PhD Thesis that directly resulted from the sponsored research and contains all the major findings

BAYESIAN NETWORKS FOR UNCERTAINTY ESTIMATION IN THE RESPONSE OF DYNAMIC STRUCTURES

A Dissertation
Presented to
The Academic Faculty

by

Giorgio M. Calanni Fraccone

In Partial Fulfillment
of the Requirements for the Degree
Doctor of Philosophy
in the
School of Aerospace Engineering

Georgia Institute of Technology
August 2008

BAYESIAN NETWORKS FOR UNCERTAINTY ESTIMATION IN THE RESPONSE OF DYNAMIC STRUCTURES

Approved by:

Dr. Vitali Volovoi, Advisor
School of Aerospace Engineering
Georgia Institute of Technology

Dr. Massimo Ruzzene, Co-advisor
School of Aerospace Engineering
Georgia Institute of Technology

Dr. Peter Cento
Aerospace Testing Alliance
*Arnold Engineering Development
Center*

Dr. Dewey Hodges
School of Aerospace Engineering
Georgia Institute of Technology

Dr. Andrew Makeev
School of Aerospace Engineering
Georgia Institute of Technology

Date Approved: 26 June 2008

ACKNOWLEDGEMENTS

It is always difficult to synthesize personal experiences and emotions by means of a few words, as countless events and innumerable people have constantly shaped and steered the course of this journey that is referred to as life. As I conclude my academic experience at this prestigious institution, I cannot however exempt myself from acknowledging the immense help and assistance that I received from my advisors, Dr. Vitali Volovoi and Dr. Massimo Ruzzene, whose knowledge and active guidance have sustained my efforts in the pursuit of my scientific goals and dreams. Their commitment to research and striving for excellence provided an invaluable source of inspiration, something so entirely essential in overcoming the inevitable challenges of graduate school.

Throughout my time at Georgia Tech, I had the privilege to meet and interact with many remarkable individuals; from outstanding faculty members, always willing to share their expertise and wisdom, to fellow students with whom I spent long hours of research and stimulating conversations as well as my limited free time. My sincere thanks go to them as they contributed to expanding my scientific background, enriching my personal horizon, and fostering my deep interest for science and cultural diversity.

Away from Italy, my American and international friends have provided me with a home away from home. To them goes my appreciation, as their care, dependability and generosity, both spiritual and practical, were indispensable elements for my happiness and success here. A special and heartfelt mention goes to Joanna Karamanou for her endless kindness, infinite patience and close friendship.

My acknowledgements would be incomplete without expressing deep gratitude to my family and old friends who, from Europe, have continued to encourage and love me through the years; without their never-ending support, I would not have accomplished as much as I have.

So, having arrived at the end of this leg of the journey, a tiny step for mankind, and yet a great leap for me, I share my doctoral achievement with my dear ones!

TABLE OF CONTENTS

LIST OF TABLES

LIST OF FIGURES

SUMMARY

The dissertation focuses on estimating the uncertainty associated with stress/strain prediction procedures from dynamic test data used in turbine blade analysis. An accurate prediction of a physical component's maximum response levels occurring during in-field operating conditions is essential for evaluating its performance and life characteristics, as well as for investigating how its behavior critically impacts system design and reliability assessment. Currently, stress/strain inference for a dynamic system is based on the combination of experimental data and results from the analytical/numerical model of the component under investigation. Both modeling challenges and testing limitations, however, contribute to the introduction of various sources of uncertainty within the given estimation procedure, and ultimately lead to diminished accuracy and reduced confidence in the predicted response.

The objective of this work is to characterize the uncertainties present in the current response estimation process and provide a means to assess them quantitatively. More specifically, a statistical methodology is proposed that is based on a Bayesian-network representation of the modeling process which allows for a statistically rigorous synthesis of modeling assumptions and information from experimental data. Furthermore, such a framework addresses the problem of multi-directional uncertainty propagation and permits the inclusion within the analysis of newly available test data that can provide indirect evidence on the parameters of the structure's analytical model, as well as lead to a reduction of the residual uncertainty in the predicted quantities.

As part of this research, key sources of uncertainty are investigated and their impact upon system response estimates is assessed through sensitivity studies, the results of which are utilized for the identification of the main contributors to uncertainty to be modeled within the developed Bayesian inference scheme. The appropriate Bayesian network is constructed using data generated in a simulated experimentation environment, statistically equivalent to specified real tests, and is then infused with actual experimental information for the purpose of explaining the uncertainty embedded in the response predictions, as well as quantifying their inherent accuracy.

CHAPTER I

INTRODUCTION

1.1 Overview

This research focuses on the estimation of the vibratory response of dynamic structures, with attention to turbine engine bladed disks. The inevitable presence of inherent sources of uncertainty within any estimation technique negatively impacts the accuracy and the confidence level associated with a system's estimated response, thus limiting how well its performance and life characteristics can be assessed. Broadly speaking, uncertainties and errors originate primarily from two sources: experiments and system analysis. The objective of this work is the formulation of an integrated statistics-based framework built upon the information provided by the aforementioned contributors and capable of assessing the level of uncertainty therein embedded. Ultimately, such framework is aimed at improving the estimation of the maximum stress levels in structural systems.

1.2 Motivation

Extensive studies have been conducted on bladed-disk assemblies as their performance critically affects the reliability of gas turbines and aircraft engines. Typically, tests are conducted to measure the vibratory response of blades or other components under given load conditions, where the measurements are then used in conjunction with a predictive model [76] to infer the critical response levels, and to help in the assessment of a system's fatigue life and failure modes. Measurement data are used to calibrate analytical/numerical models, and to investigate how accurately they can predict a physical system's behavior, which is a major point of interest within the realm of design as well as for model verification and validation [84]. The accuracy of any response inference technique is limited by a number of factors concerning the physical system, its structural modeling, and the test setup. On the one hand, sensor-based constraints (e.g., type of sensors, measurement inaccuracy, bandwidth, and range of operability), validity of measurement data obtained in a controlled

1

test environment (rather than in field conditions), as well as the lack of knowledge of the physical system's true state (e.g., geometric tolerances or unknown boundary conditions), all contribute to the introduction of uncertainty into the measured vibratory response. On the other hand, system models are also affected in their predictive capability by their inherent assumptions and simplifications.

In this realm of modeling, a key aspect for disk assemblies is represented by system complexity associated with the possibly high number of blades comprising a single disk. Ideally, blades are equal to one another, but perfect symmetry is never attained because of manufacturing discrepancies, which can be further exacerbated by different in-field levels of wear and tear occurring on each blade. As a result, disk assemblies may experience the emergence of localized dynamic phenomena (i.e., "rogue" blade responses [9, 14, 18, 36]) characterized by vibratory stress levels higher than the average overall response. The ability to meaningfully evaluate these critical conditions is limited by instrumentation-based constraints as well as analytical/numerical challenges. On the one hand, financial reasons and technical limitations may determine the number of conducted experiments as well as their test set-up and data analysis. A subset of blades is usually instrumented and the measurement locations rarely coincide with the regions of maximum response levels, thus requiring the use of analytical models to perform an extrapolatory assessment of the system's behavior. On the other hand, the loss of structural symmetry in a disk entails significant computational costs, associated with the necessary modeling of the entire disk and all the blades, which often call for a trade-off with respect to model fidelity.

The aforementioned issues, technical limitations and modeling challenges all cause uncertainty and error to be embedded in the estimation of the true response of any disk assembly, as well as other structures. As a consequence, system assessment needs to be robust from a probabilistic viewpoint. A statistics-based use of measurement data and analytical approaches can help quantify uncertainties, assess their propagation and interaction, as well as provide meaningful insight on system-design robustness in terms of quantifiable uncertainty bounds on a system's predicted behavior.

1.3 Literature Review

Following is an overview of various research efforts and approaches addressing the issues of system complexity and uncertainty assessment for structural systems, both at the analytical and experimental level. Although some emphasis has been given to the field of turbomachinery analysis, many of the issues, concepts and techniques herein discussed have sprung from or found applicability in other structural systems and applications.

1.3.1 Structural Analysis of Bladed Disks

Modeling and analysis of turbine engine bladed disks can be computationally intense depending on the required level of detail. Given the geometric and dynamic periodic nature of such systems, the use of cyclic analysis [59, 81, 98] on a limited number of substructures can prove to be very efficient, but it can become impractical to use when localized phenomena are of interest (e.g., localized dynamics due to differences among the substructures). In such instances, analysis of the full structure may be instead necessary due to the loss of cyclicity. The need for extensive simulation, however, calls for a trade-off between accuracy and computational performance. In light of these analytical and computational challenges, several approaches have been presented in the literature to reduce the computational cost while retaining an adequate level of detail.

The techniques available range from model order reduction via spring-mass-damper system representation to reduced finite-element cyclic analysis. In [35, 36, 90, 105, 106], a disk sector is described via an equivalent set of lumped masses where springs simulate blade-to-blade coupling, while dashpots account for energy dissipation phenomena (e.g., aerodynamic damping). It has been demonstrated that lumped-parameter models of disk assemblies are able to spot the presence of localized dynamic phenomena [105], but a more detailed analysis may be required to establish a correlation between the dynamics of the lumped system and the actual assembly. An improvement with respect to lumped systems is to model the blades as continuous media with simpler geometry (e.g., beams or plates) [64], whereas other modeling techniques rely on finite-element solutions. Proposed in [52, 78] is a technique to generate reduced-order models of disk assemblies based on component-mode

approaches [8, 48], where a single blade and the whole rotor are the two modeled components, and where the overall dynamic behavior of a single blade is reconstructed as the combination of a disk-induced static motion and an elastic motion for a fixed-free blade. This approach lowers the computational cost by downsizing the number of finite element degrees of freedom while maintaining the key characteristics of the modes. Model reduction through component modes has been further extended to other turbomachinery investigation problems (e.g., prediction of forced-response in early-stage engine design [87, 88], analysis of shrouded assemblies [9], or assessment of centrifugal stiffening effects [72]) and is at the core of the widely accepted computer code "REDUCE" [10, 11].

The spectrum of available modeling techniques (reduced or not) for turbine engine assemblies is quite varied. All of them, however, are affected by limitations in their capability to accurately capture the physical phenomena under investigation. The results obtained via numerical/analytical analyses have an inherent inaccuracy which ought to be quantified in order to properly predict a system's performance.

1.3.2   Uncertainty in Engineering Applications

Understanding uncertainty is important when assessing any physical system/phenomenon through analytical/numerical modeling. Despite the deterministic nature of a physics-based model, the results obtained from it ought to be treated in a probabilistic manner because of the uncertainty associated with the model's input parameters, structure and predictive accuracy, which also needs to be assessed in a statistical manner.

Uncertainties can be broadly grouped into two main categories: physical uncertainties and model-related ones. The first group originates from the difference between a physical system's true state and its model representation, as well as from the discrepancy between actual and nominal testing conditions, while the second stems from the limited fidelity and approximations of the structural model and analysis. Physical uncertainties include, among others, manufacturing variations, sensor calibration and sensitivity, measurement noise, gauge non-linearities, sampling rate and data processing algorithms. Modeling uncertainties, instead, stem from simplifications in the model geometry, inexact boundary

conditions, finite-element discretization level and element formulation, and any other hypotheses underlying the numerical representation. This categorization is not the only one proposed in the literature and may vary in interpretation as well as in the level of detail and subcategorization [15, 24]. Another classification distinguishes between irreducible uncertainty and epistemic one [92]. The former is related to the very random nature of reality, whereas the latter originates from the lack of knowledge about a physical system being analyzed, and can be reduced by acquiring more information about it.

Of particular interest in the field of turbomachinery is the problem of randomness in blade geometry and material properties (and consequent disk mistuning) induced by manufacturing irregularities. In order to compute the system's response and address its inherent random nature, various approaches have been considered. Stochastic finite-element methods have been developed to address the coupled issues of uncertainty (in the system and its surrounding environment) and geometric/topological complexity. The deterministic discretized physics formulation is made stochastic by randomizing, in accordance with an appropriate probabilistic uncertainty framework, some of its constituting elements (e.g., the mass matrix, or the external loading function) used to generate a system of random equations. These equations are solved using an extensive host of techniques that has been developed throughout the past decades [33, 34, 57]. Techniques based on the Monte Carlo simulation approach [69] are widely used [40, 91] to propagate uncertainty directly from inputs to outputs, but they can be computationally expensive. For this purpose, principal component analysis can be adopted to downsize the set of random variables to a meaningful subset before employing Monte Carlo simulations [14], or, thanks to its ability to represent any type of probability distribution, the polynomial chaos technique [90] has been suggested as an analytical alternative to numerical simulations for the computation of the statistics of a system's response. Other techniques like response surfaces and FORM/SORM (First/Second Order Reliability Method) have been utilized to replace, when possible, the intense computations with fast-running approximations. Response surfaces have been used largely to construct surrogate models linking system inputs to outputs, whereas FORM and SORM have been employed to numerically solve multi-variate probability integrals

over complex domains of integration. In [107], however, the former two techniques have been shown to be unsatisfactory even for the simple nonlinear Duffing oscillator, indicating that a probabilistic characterization of uncertainty might not always be well suited to describe nonlinear systems exhibiting complex (e.g., bifurcating) dynamic behavior.

In quantifying uncertainty, probabilistic methods have been largely used especially to characterize the variability in a system's properties. As done in many stochastic analyses, these techniques involve the assignment of probability functions for the uncertain properties followed by their propagation to determine the probability distributions at the output level. Needless to say, the results obtained via these approaches are meaningful as long as the selected uncertainty models are sound with respect to the available measurement information, in terms of both the selected distribution type as well as the values of its parameters.

In order to address the limitations of the probabilistic approaches in quantifying the variability in a system's parameters and inputs, research has progressed towards a particular group of techniques consisting of the so-called possibilistic methods. In contrast to the probabilistic methods, no probability distribution is assumed for the given parameters. Conversely, the uncertainty in those parameters is represented in terms of a range of possible values. Belonging to this category are methods based on interval arithmetic [68], affine analysis [23], fuzzy analysis [113], and information-gap theory [7, 96].

Analysis based on interval arithmetic is conceptually straightforward and tends to be computationally cheap in terms of the needed number of runs. It suffers, however, from the problem of overestimating the level of uncertainty in the system responses due to the fact that no information about the interdependencies existing among the various uncertain system quantities is retained in the algebraic manipulations. One way to overcome this drawback is to make usage of the affine analysis, through which narrower uncertainty bands can be determined and sensitivity relationships between inputs and outputs can be established in order to identify the stronger uncertainty drivers. Both approaches guarantee that all the worst-case scenarios of a system's response are captured as they all fall inside the computed uncertainty bands. This feature makes interval-based approaches more appealing than the probabilistic techniques, especially in terms of design for robustness. In [31, 83],

6

the use of interval analysis has been demonstrated for the evaluation of the uncertainty bounds on a system's eigenfrequencies associated with material and geometric uncertainties, whereas in [62] real affine analysis has been extended to the complex plane and tested on a simple lumped-element system, while its successful applicability to large complex systems is still an object of research.

Fuzzy analysis builds upon interval arithmetic where various α-cuts are considered for the uncertain quantities. Like for interval analysis, fuzzy analysis also experiences the problem of dependency, but has been proposed for structural uncertainty problems [53, 54] because it offers a way to address the concept of vague and imprecise knowledge with no assumption needed on the random nature of the uncertain parameters. Finally, the information-gap approach becomes useful when probabilistic uncertainty models cannot be constructed due to a scarcity in the measurement data and/or knowledge about the model form. Since the method can build upon limited information, it is considered to be well suited for design processes which emphasize system robustness over performance. This has been shown in [96], where information-gap models of uncertainty sources in a structural system are employed to construct a measure of robustness to be maximized in the presence of competing sources of variability. The potential capabilities of this method are extended further in [7] which suggests the possibility of linking uncertainty models with possible decision-making schemes so as to improve understanding and usage of the newly acquired information.

In [94] a distinction is drawn between system input/parameter uncertainties and modeling uncertainty, exclusively in terms of what their proper characterization should be. In fact, while the former may be treated by modeling each of the system quantities as a random variable, modeling uncertainty stems from the simplifications embedded in the analytical framework and its consequent discrepancy with the physical system, which no change in the system inputs or parameters may be able to eliminate. Therefore, it is argued that parametric probabilistic approaches cannot properly describe this source of uncertainty because of its insensitivity to system inputs and parameters. A non-parametric methodology, based on random-matrix theory, has been suggested, instead, as a valid alternative [93, 94] to

quantify and reduce modeling uncertainty. Furthermore, from a practical standpoint, the use of non-parametric probabilistic methods has also been investigated as a way to address the problem of dimensionality associated with the large number of parameters necessary to fully characterize complex systems (e.g., a blade's random geometry). The size of the problem is reduced by mapping the physical sources of randomness into a set of control parameters instead of modeling them explicitly within a probabilistic scheme. To this end, in [16], a non-parametric approach has been implemented which uses so-called dispersion parameters to control the variability within the bladed-disk's discretized equations of motion (i.e., the system matrices). Another application of the method is presented in [17], where it has been employed to inversely assess the manufacturing tolerances required to limit the mistuned response of an industrial fan.

The need for a large database to quantify uncertainty has also called for a maximal usage of historical databases of analyses and tests, which are especially useful when in-field conditions of interest cannot be reproduced. In [39, 40, 43], the uncertainty embedded in a linear system's model is assessed using a database of similar structures. Covariance-based metrics to quantify modeling uncertainty are derived in terms of uncertain modal quantities (i.e., natural frequencies, modal mass, stiffness and damping), which are normalized and made independent of geometry and frequency scales so that any lacking data can be borrowed from a database of generically related structures. The modeling uncertainty of a particular system can then be obtained by appropriate inverse rescaling. The use of modal quantities is deemed to be useful as their variability can describe the combined effect of several sources of uncertainty (e.g., measurement error associated with indirect measurement of the modal quantities of interest, or experimental errors due to tests being conducted on components rather than on the full assembly [39, 43]). The use of experimental data from structures other than the one under investigation is also beneficial as it accounts for the uncertainty associated with the physical components (e.g., product/manufacturing variability, or measurement scatter across multiple experiments when only data from one test are available). Of course, as more system-specific information is available to replace the generic data, the modeling uncertainty can be computed with higher confidence, where it has been shown

that it reaches a minimum if computed using only structure-specific data sets [42], thus indicating that modeling uncertainty is assessed in a conservative sense. As done for linear structures, this uncertainty-quantification approach has been extended successfully also to nonlinear structures [41, 44] (via the use of singular-value decomposition and principal components), and has been implemented in the commercial package NASTRAN [45].

The use of Bayesian statistics has become widespread in several fields of study, thanks also to its appealing abductive property which facilitates the identification of the likely root causes for observed events. Moreover, its use allows the incorporation of newly available (exogenous) information into the analysis as well as its propagation from any given level or phase of analysis (e.g., test measurements on a system's component) to other levels (e.g., response prediction for the all system) [61]. The use of Bayesian statistics in the field of gas turbines was first suggested more than ten years ago [13] and its popularity has continued to increase ever since in areas like structural model updating and validation, reliability, or damage control [12, 25, 46, 108, 110]. The various Bayesian approaches all rely on the same principle, i.e. the Bayes' theorem; but they differ in the way the probabilities of the quantities of interest are numerically approximated and/or updated in the presence of error-carrying and, often times, limited and/or incomplete evidence (e.g., due to the use of a small set of measurement gauges).

1.3.3   Uncertainty in System Identification, Updating and Validation

In order to analyze, investigate and predict a physical phenomenon or system, a mathematical model is often constructed to describe the interdependencies among the various physical quantities directly involved in the given process. A generic parametric form of such a model is given by

$$\mathbf{g}(\mathbf{z}, \boldsymbol{\theta}) = \mathbf{0} \tag{1}$$

where g represents a $\boldsymbol{\theta}$-parameterized system of equations, of possibly various natures (e.g., algebraic, differential, or integral), describing the relationships between the physical quantities in the vector $\mathbf{z}$, while $\boldsymbol{\theta}$ is a set of parameters whose values are usually unknown *a priori*. Of course, depending on the particular phenomenon or system, the model g can be

further customized by separating the elements of $\mathbf{z}$ in dependent and independent quantities, observable and unobservable, and so forth. In fact, equation (1) could be rewritten in the following form:

$$\mathbf{y} = \mathbf{f}(\mathbf{x}, \boldsymbol{\theta}) \qquad (2)$$

which explicitly describes the relationship between the independent variables $\mathbf{x}$ and the dependent quantities $\mathbf{y}$, which are such that $\mathbf{z} = [\mathbf{x}, \mathbf{y}]$.

The main issue associated with complex systems and their dynamics is indeed to find the proper representation in terms of the physical quantities to be included within $\mathbf{z}$, the causal relationships $\mathbf{g}$ linking them, and the determination of the parameters $\boldsymbol{\theta}$. In the literature, system identification refers to the plethora of methods and approaches developed to perform the task of describing an observed system via analytical/numerical models. As suggested by [74], these methods can be grouped in three categories: white-box, black-box and gray-box models. For the white-box models, there exists a good understanding of the system or process being investigated through which an appropriate physics-based model $\mathbf{g}$ can be rigorously formulated or selected. In this case, system identification translates into the subproblem of parameter estimation for the values of $\boldsymbol{\theta}$ that best correlate the mathematical framework to reality. To this end, the classical methods of least squares and statistically equivalent maximum likelihood have been long used [5, 51]. Black-box approaches are data-driven and come into play when the cause-effect relationships describing a system or a process cannot be readily isolated. This is primarily the case for systems and processes which are complex in nature and/or whose dynamics lies in a high-dimension variable space. These techniques consists of mapping a system's inputs to its outputs based exclusively on the observed/measured data. Data fitting is at the core of this type of system identification, and approaches based on response surfaces [95] or neural networks [19, 20] have been proposed. As suggested by the nomenclature, gray-box models represent, instead, a combination of the previous two types. Extensive surveys on system identification techniques applied to structural dynamics are given in [37, 50, 51, 74, 101, 102], where time-domain, frequency-domain, modal-based, parameter-estimation and data-fitting approaches are discussed and compared with one another. Although the development of a

10

new system identification methodology is not the primary objective of this research, system identification is at its basis, as any analytical model is inherently imperfect and its predictive quality strongly depends on the assumptions embedded in it, as well as on the uncertainty contained in the data utilized to correlate its predictions with the observed reality. In particular, model updating techniques rely on the information regarding observable quantities to identify a suitable model within a class of plausible system representations, and to fine-tune the parameters of that specific representation to better match its response predictions with the measurement data.

In the past decades, various approaches have been developed to update finite-element structural models, a survey of which can be found in [70]. Some of these techniques consist in the optimization of an objective metric, a function of certain model parameters, through standard optimization schemes, like genetic algorithms or simulated annealing [56, 82]. According to [58], however, a distinction between model parameters and model structure, both of which contribute to modeling uncertainty, is deemed necessary in the problem of model updating. In fact, the concern raised is that an update performed only on model parameters may cause the adjusted quantities to no longer carry a physical meaning when their correction is in response to errors and discrepancies with test data for which they are not ultimately responsible. In [58], an approach to include uncertainty due to model structure into model updating practices is also presented, where geometric parameters, namely node coordinates, are optimized together with mass, stiffness and damping properties.

Uncertain model accuracy, quality of the measurements, and limited quantity of the observed information with respect to a model's level of detail, are such that system identification and model updating are often affected by the issues of ill-conditioning and solution nonuniqueness. To address these challenges caused by the embedded variability, statistical inference has been proposed since the 1970's with the idea of superimposing a probabilistic model upon a deterministic structural model [28]. More recently, the use of Bayesian statistics has been suggested to construct a framework for model updating where the aforementioned issues are addressed by considering a class of structural models together with probability models, for parameter and prediction uncertainties, which are then updated

using the available test data via Bayes' theorem [6, 104]. In this context, the plausibility of each structural model, within the chosen class, becomes a function of the available data, according to which either a single most probable/likely and optimal model can be determined (in the case of global identifiability [49]), or several optimal sets of parameters' values and corresponding optimal models exist (in the case of local identifiability [49]), whose contributions are weight-averaged to produce a system's mean prediction of the response. Hence, rather than adopting a single model in the presence of multiple choices, this approach addresses, in a robust sense, the problems of solution nonuniqueness and ill-conditioning by weighing the relative importance of each model according to their plausibility with respect to the observed data, and by assigning a variance to the mean response which accounts for the lack of global identifiability and solution uniqueness.

This model updating technique has been employed, for instance, in the field of health monitoring and damage detection where a time-dependent probabilistic damage measure, constantly updated by means of time-varying newly available measurements, is used to assess the structure's health condition [21, 22, 55, 104, 108, 112]. Moreover, it has been tailored to address various scenarios of measured-data incompleteness, such as unmeasured input conditions and limited number of measured degrees of freedom [108, 111]. In order to address the large computational cost associated with solving the Bayesian probability integrals, various numerical methods have been exploited ranging from an asymptotic approximation [6], whose accuracy degrades as test data become more scarce, to Markov Chain Monte Carlo (MCMC) simulations [109], which are generally inefficient when dealing with high-dimension problems, to Gibbs sampling (a subclass of MCMC simulations) whose sampling dimensionality has been successfully uncorrelated from the number of uncertain parameters being explicitly modeled, thus making the stochastic analysis computationally more manageable [22].

For the purpose of model updating and model prediction assessment, direct uncertainty propagation is also well established. In this context, the probability distributions of certain input parameters of a system are assumed to be known and are employed to compute a corresponding probability distribution for its response. Knowledge of parameter uncertainty,

12

however, may not always be readily available from inspection and/or measurements (e.g., a particular parameter might not be directly measured), therefore any assumption on its statistical nature could be misleading or erroneous. In [29, 30], an inverse method is suggested to extract the missing information on parameter uncertainty from the measurement data themselves. The technique consists of assigning a parametric family of probability distribution functions to the system inputs of interest, of establishing the statistical relationship between system inputs and outputs via a direct propagation scheme (namely a perturbation scheme and Monte Carlo simulations), and of using such a relationship to construct an output-measurement-based likelihood function to be maximized with respect to the parameters characterizing the family of probabilities (e.g., mean and covariance matrix for Gaussian distributions). The estimators for the parameters of a probability family, obtained through this maximization process, identify the probability density function that best agrees with the given test data, and provides a statistical representation for the uncertainty in the corresponding system input parameters.

Despite the insight gained on parameter uncertainty, the method in [29, 30] fails to address the issues of modeling and measurement variability, which condition the quality of the gathered knowledge. These aspects have been tackled in [63, 71] where a stochastic model-updating approach was developed to account explicitly for such uncertainty sources. Given a set of system outputs, multiple data sets of their experimental observations, obtained from seemingly identical yet distinct structures because of production variability, are statistically compared against multiple sets of their simulated predictions, generated, in turn, via direct propagation of *a priori* uncertainty in the chosen set of model parameters. Updated estimates for these parameters' statistics are then derived through a minimization scheme applied to the Euclidean distance between the mean values of the experimental and simulated results, whose reconciliation is deemed to take into consideration the modeling and experimental variabilities in a more exhaustive fashion. Finally, in dealing with the assessment of model uncertainty in model updating, an important issue is the independence of the observations. In particular, when model prediction errors are accounted for in the

updating process, it was shown that the correlation existing among their different realizations reduces, *de facto*, the amount of information contained in them [32]. This loss of information, when not incorporated in the objective or likelihood function used to identify the most likely system model, is deemed to potentially lead to misleading predictions by the model itself.

Model validation, closely related to model updating, also makes use of experimental data, although for a different purpose, which is the evaluation of model prediction capabilities instead of model tuning. Validation and consequent response predictability of a system are evaluated by means of a correlation assessment of test data versus simulated results for the same scenario, where a model is arguably assumed to be validated as long as it is capable of replicating the measurement data themselves [40, 47]. This approach offers no guarantee that the validated model at hand can indeed predict accurately outside of the tested region [47]. Furthermore, the experimental data used for validation are affected by uncertainty, thus requiring results to be characterized, once more, in a statistical fashion. In some cases, this uncertainty is simply included within the already pre-existing modeling uncertainty [40], where experimental results are, instead, treated as the reference condition. In other circumstances, selection from competing models is performed by means of statistical hypothesis testing on a given metric, according to which a proposed analytical model is either accepted or rejected based on observed data affected by errors.

In [60, 61, 85, 114] the Bayes' factor has been used in the context of system model verification and validation, while examples are offered in [3, 103] on how it can also be utilized as a means to address the lack of knowledge, referred to as statistical uncertainty [103], about the uncertainty models themselves (e.g., unknown type of probability distribution and unknown values of its parameters). In fact, given a set of observed data, a host of probability-distribution models may be considered for fitting those data. In the presence of competing models, the Bayes' factor has been shown to facilitate in the selection process when other goodness-of-fit metrics were instead inconclusive in determining which probability distribution was best suited with respect to the observations [103]. Inasmuch as the Bayes' factor is constructed upon some prior knowledge about the problem at hand and

14

constitutes a metric to perform comparisons, various alternative definitions of it have been put forth in the literature to address both the issue of incomplete/missing priors and the problem of having to compare "apples" to "oranges" (i.e., comparison and selection between disjoint sets of models) [3].

In summary, the wealth of methods addressing the issues of uncertainty quantification and propagation appears to be rather substantial, ranging from perturbation/sensitivity techniques and stochastic procedures, to parametric/non-parametric probabilistic and possibilistic approaches, to causality-oriented methods like the Bayesian networks. Each technique has been proposed to tackle a specific source of uncertainty, type of system (e.g., linear or nonlinear), or related computational challenges. Their common ground is the quantification of uncertainties through appropriate measure metrics, and the modeling of their propagation to improve the design of a system safety-wise and reliability-wise, as well as to assess its predictive capability within the desired range of usage and in-field conditions.

1.4   Work Scope and Organization

As appears from the previous sections, the predictive accuracy of a system model is affected by uncertainty introduced by simplifying assumptions, lack of complete knowledge about the physical unit, or other closely related causes. To improve model fidelity, test data are usually correlated with model results for calibration purposes even as the former are affected by uncertainties and errors. As a result, it becomes essential to assess a system's predictive accuracy when several sources of uncertainty, both from modeling and test analysis, are combined together. Within the large field of uncertainty modeling, this research is focused on the probabilistic description of uncertainty present in dynamic structural response predictions. The proposed methodology provides a structured and coherent way to correlate and merge different sources of information to help enhance the quality of the estimation and the assessment of uncertainty. To this end, the research comprises the following steps:

- Isolation, whenever possible, of the sources of uncertainty associated with different contributors (in this context, analytical model and experiments);

- Parameterization of the system's model with respect to the given sources of uncertainty;

- Identification of the main contributors to uncertainty by means of a sensitivity analysis conducted on the system's model and aimed at filtering out those factors that weakly influence the observed uncertainty;

- Assessment of the level of uncertainty present in experimental data sets via model/test correlation analysis;

- Probabilistic representation of uncertain quantities within a Bayesian-network-based response inference scheme;

- Assessment of the impact of the considered uncertainty sources upon system's accuracy; and

- Uncertainty reduction based on the information obtained from (additional) experiments.

Built upon these steps, a unified statistical framework, based on the use of Bayesian networks, has been implemented and investigated as a means to estimate the critical vibratory response of structural systems. The role and relevance of these steps will be elaborated further and become clear in the following chapters.

Including this introduction, this dissertation consists of six chapters. In Chapter 2 the impact of modeling and physical uncertainties associated with structural systems is assessed, where uncertainty in geometry, material properties and test measurements are taken into consideration. A model-based technique for the estimation of the vibratory response of dynamic structures is introduced and propagation of its embedded uncertainty is simulated through the use of probabilistic analyses conducted upon given system and experimental parameters. For this purpose, two modeling approaches were considered to describe bladed disks respectively based on beam theory and lumped dynamic elements, and cyclic analysis. In Chapter 3, the same inference technique is applied to experimental data for a simplified geometry. The impact of experimental uncertainty upon the response estimation is

16

quantified through a correlation analysis of the results from the system's numerical model and the corresponding test data. More specifically, the objective of this investigation is to account for uncertainties associated with sensor accuracy and measurement noise level in an explicit manner. To this end, test measurements from cantilever plates were used so as to limit the effects otherwise related to more complex test setups and system modeling. In Chapter 4, a feasibility study on the application of Bayesian networks to the problem of uncertainty reduction in structural dynamics is presented. In particular, Bayesian belief networks are explored as a potential means to enable the exchange of information between experiments and model. Their use is intended to enable the propagation of any additional information, available, for instance, for certain components of the structure or at different stages of the analysis, throughout the entire response inference process with consequent updating of the estimated quantities. In Chapter 5, a Bayesian-network representation of the model-based response inference procedure is formulated and its performance in terms of uncertainty reduction, through the propagation of additional information, is assessed for a beam and a plate structure, for which the impact upon prediction fidelity of additional sensor measurements is explicitly evaluated. Test and model uncertainties are both taken into consideration together with the lack of knowledge about the physical system in a unified framework, whose underlying assumptions are also discussed. Finally, Chapter 6 provides a summary of the findings and an introduction to the open-ended challenges to be addressed together with possible directions for future work.

CHAPTER II

SIMULATION OF UNCERTAINTY PROPAGATION IN
MODEL-BASED RESPONSE INFERENCE

2.1 Overview

In this chapter, a standard technique to predict a system's vibratory response is presented. Such a process consists of estimating the maximum vibratory response of a system via modal scaling of given peak amplitudes observed in test results. Such a technique involves the direct interaction between modeling and experiment-related uncertainties. Sensitivity analysis is performed to quantify the impact of such sources of uncertainty upon the predicted response's accuracy, and to study the propagation of experimental uncertainties through a numerical model also affected by inaccuracies. More specifically, the effects of unknown model characteristics (e.g., mode shape error), sensor measurement and location are explicitly addressed, while the impact of other uncertainty sources could be implicitly taken into consideration. The interaction among uncertainties and their effects are investigated by means of simulated experimental results for two structures of different complexity: a simple beam-like blade model and a more realistic blade model, described via finite-element analysis.

2.2 Model-based Response Estimation Methodology

In structural dynamics applications (e.g., turbine engine blade testing), maximum stress levels are estimated through the combination of measurements of the system's vibratory response at given sensor locations, and information obtained from the numerical model of the component. The inference technique adopted in this work consists in scaling the mode shape of the system that best approximates its forced response at the frequency of maximum excitation. In fact, at any point $\mathbf{x} = (x, y, z)$ on the structure, the forced response amplitude

$\varepsilon(\omega, \mathbf{x})$, at the excitation frequency ω, can be written as a linear modal expansion:

$$\varepsilon(\omega, \mathbf{x}) = \sum_{j=1}^{\infty} D_j \phi_j(\mathbf{x}) \tag{3}$$

where the quantities $\phi_j(\mathbf{x})$ are the structure's mode shapes, and D_j are the coefficients of modal participation, which, in general, may be functions of frequency and/or time. In a case where the excitation frequency ω approaches the natural frequency ω_n of the system, the forced response may be estimated according to the following approximation:

$$\varepsilon(\omega, \mathbf{x}) \approx D_n \phi_n(\mathbf{x}) \tag{4}$$

The estimation process can be thought of as composed of two steps: the identification of the mode corresponding to a given resonance peak, and the subsequent extrapolation of maximum response values through the combination of available test data and information from the model. These two steps are described in the following sections.

2.2.1 Mode Identification Procedure

It is assumed that a structure's response corresponding to a given frequency peak of the vibratory response is proportional to the corresponding mode. This assumption, which neglects residual contributions from the other modes of the structure, introduces errors in the case of closely-spaced modes, but is commonly used for the estimation of stress levels in turbine engine bladed disks [100]. The identification of the mode corresponding to a given peak p in the response spectra assumes the presence of N_g gauges mounted on the structure at locations $\mathbf{x}_g$ ($g = 1, \ldots, N_g$). Let ω_n be the n-th modal frequency obtained from the numerical model of the component under investigation, with $n = 1, \ldots, N_m$ where N_m is the number of modes in the frequency range of interest. For the purpose of mode identification, a parameter $\psi_{p,n}$ may be defined as follows:

$$\psi_{p,n} = \sum_{i=1}^{N_g} \left\{ |\omega_{p_i} - \omega_n| + \sum_{j=1}^{N_g} \left| \left| \frac{\varepsilon(\omega_{p_i}, \mathbf{x}_i)}{\varepsilon(\omega_{p_j}, \mathbf{x}_j)} \right| - \left| \frac{e_n(\mathbf{x}_i)}{e_n(\mathbf{x}_j)} \right| \right| \right\} \tag{5}$$

where ω_{p_i} denotes the p-th peak frequency recorded at sensor i, $\varepsilon(\omega_{p_i}, \mathbf{x}_i)$ is the measured response amplitude at that frequency, while $e_n(\mathbf{x}_i)$ is the modal quantity corresponding to the measured response, evaluated at the sensor location $\mathbf{x}_i$. The parameter $\psi_{p,n}$ is a measure

of the proximity between a numerical mode and corresponding frequency and measured peak response amplitudes and frequencies. Given a numerical mode n, the corresponding resonating mode in the measured data can be found by minimizing $\psi_{p,n}$, for $p = 1, \ldots, N_p$.

2.2.2 Estimation of Maximum Response

The modal identification procedure described above can be used to combine measured information at the sensor location with modal data obtained from the model. The modal data together with the assumption that a single mode contributes to the measured response at the considered resonance peak permits the estimation of response amplitudes at a location different from where a sensor is mounted. In principle, response amplitudes can be estimated over the entire structure, and maximum values can be easily extrapolated. For instance, assuming that strains are measured, the strain at a generic location $\mathbf{x}$ can be obtained from the measured strain at location $\mathbf{x}_g$ through the following relation:

$$\varepsilon_g^*(\omega_p, \mathbf{x}) = \frac{e_p(\mathbf{x})}{e_p(\mathbf{x}_g)} \ \varepsilon(\omega_p, \mathbf{x}_g) \tag{6}$$

where ε is the measured strain amplitude at frequency ω_p, e_p is the modal strain value in the same direction of the measured strain, and ε_g^* denotes the estimated strain value at $\mathbf{x}$ based on the strain measurement at location $\mathbf{x}_g$. The modal strain is selected from the modal results in the model in accordance with the identification procedure described in the previous section. Hence, the subscript p denotes the mode shape out of the set of N_m modes which minimizes the coefficient $\psi_{p,n}$ in equation (5) for the selected peak frequency ω_p. Additional processing on the modal data also allows the estimation of equivalent strains, calculated, for instance, according to the Von Mises criterion [2, 27]. The equivalent Von Mises (VM) strain at location $\mathbf{x}$ and frequency ω_p can be simply calculated as follows:

$$\varepsilon_{VM_g}^*(\omega_p, \mathbf{x}) = \frac{e_{VM_p}(\mathbf{x})}{e_p(\mathbf{x}_g)} \ \varepsilon(\omega_p, \mathbf{x}_g) \tag{7}$$

where $\varepsilon_{VM_g}^*(\omega_p, \mathbf{x})$ is the estimated Von Mises strain at point $\mathbf{x}$ computed using the strain amplitude at frequency ω_p measured at location $\mathbf{x}_g$, and $e_{VM_p}(\mathbf{x})$ is the corresponding Von Mises modal strain.

The information obtained from all the gauges can then be combined to compute the

overall maximum amplitude ε_M^{p*} of the vibratory response metric at the p-th peak (e.g., equivalent strain, equivalent stress or displacement amplitude):

$$\varepsilon_M^{p*} = \max\left\{\max_{\mathbf{x}}\varepsilon_1^*(\omega_p, \mathbf{x}), \ldots, \max_{\mathbf{x}}\varepsilon_{N_g}^*(\omega_p, \mathbf{x})\right\} \tag{8}$$

where, ideally, the quantities $\max_{\mathbf{x}}\left\{\varepsilon_g^*(\omega_p, \mathbf{x})\right\}$ $(g = 1, \ldots, N_g)$ would be near in value. It is worth noting that the response inference technique is independent of the type of response being estimated. The nature of the measured response $\varepsilon(\omega_p, \mathbf{x}_i)$ and corresponding modal quantity $e_n(\mathbf{x}_i)$ will, of course, depend on the type of sensors (e.g., strain gauges, displacement sensors, or other) used in a given experiment. As a consequence of that, consistent modal quantities and test data are to be utilized within equations (5)-(8). Equations (6) and (8) are herein used as the basis for the analysis of various sources of uncertainty in structural dynamics.

2.3   System Modeling of a Bladed Disk

As mentioned in Section 1.3.1, several approaches are available to reduce the analysis complexity associated with bladed disks. Next, the two approaches considered in this study are presented. They are based on elementary beam theory and cyclic symmetry, respectively.

2.3.1   Reduced-order Models

A reduced-order idealization of bladed-disk assemblies is shown in Figure 1. In the given configuration, each blade is described as a beam connected to a support representing the rotor. The flexibility of the rotor is accounted for by means of concentrated translational and torsional spring elements (k_{T_r} and k_r) located at the blade-disk interfaces. Blade-to-blade coupling effects induced by aerodynamic interaction and rotor flexibility are also treated, as a first-order approximation, via translational springs (k_c). Furthermore, the centrifugal stiffening of the blades due to their precession (Ω_o) about the shaft axis is modeled according to standard theoretical approaches for rotating beams [66]. At this stage, this model only accounts for simplified boundary and loading conditions. More realistic ones, such as blade attachments and pressure loads, were not taken into account here, but would need to be included in more advanced models.
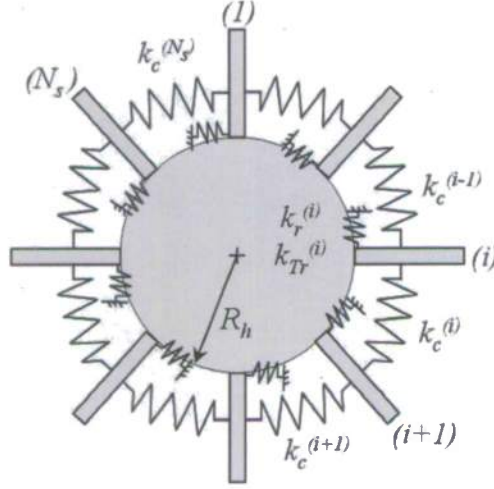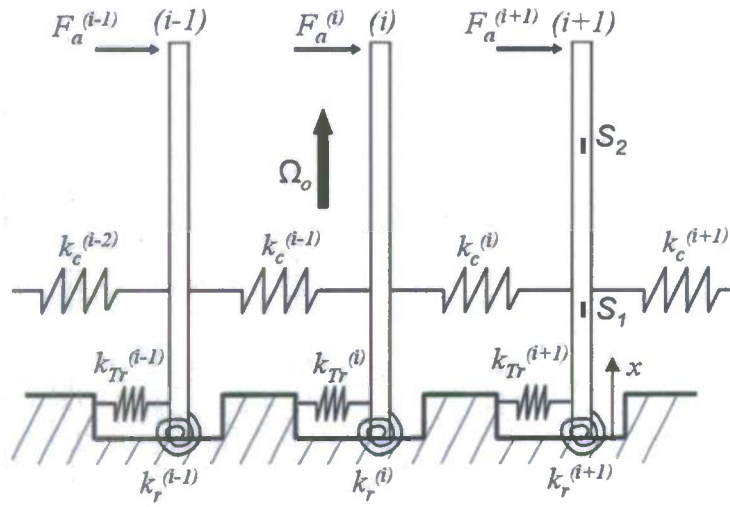
Figure 1: Schematics of simplified models of a bladed disk.
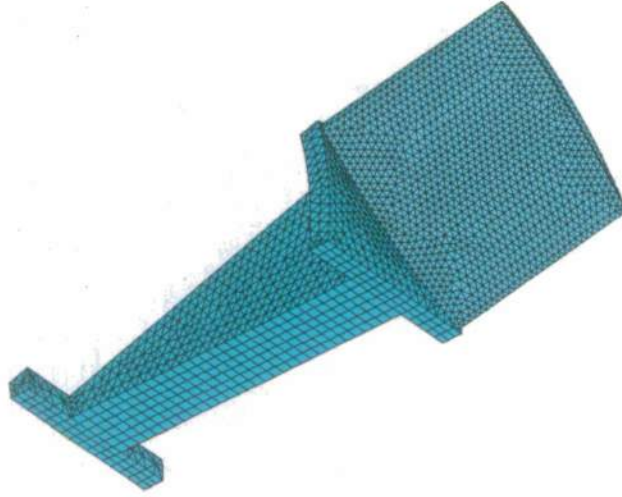
Figure 2: Finite-element model of a disk sector.

2.3.2 Finite-element Model

The other system under investigation is a disk composed of 19 nominally identical bladed sectors ($N_s = 19$). A single sector is modeled in the commercial finite-element package ANSYS©, using the mesh depicted in Figure 2. The model is discretized using SOLID95 elements, where blades and disk are considered as a single integral unit, while zero-displacement conditions are imposed at the disk-shaft interface. The structure's cyclic nature is taken into account by imposing compatibility constraints in the form of a set of periodic boundary conditions on the sector sides, similar to the ones discussed in [59, 81]. Using the duplicate-sector approach, such boundary conditions can be expressed as follows:

$$
\left\{ \begin{array}{c} U_B \\ U_D \end{array} \right\}_{side\ 2} = \left[\begin{array}{cc} \cos k\alpha & \sin k\alpha \\ -\sin k\alpha & \cos k\alpha \end{array} \right] \left\{ \begin{array}{c} U_B \\ U_D \end{array} \right\}_{side\ 1} \tag{9}
$$

where B and D represent the basic sector and its duplicate, respectively, with one exactly overlapped onto the other. Equation (9) establishes a constraint between the degrees of freedom U (i.e., displacements and rotations) of corresponding nodes on the sides of the two sectors, where each nodal U is to be expressed in a local cylindrical reference frame

23

having one axis parallel to the disk's axis of rotation and one of the others oriented in the radial direction. Moreover, $\alpha = 2\pi/N_s$ represents the sector angle in radians, while the harmonic index k is defined as:

$$
k = \begin{cases}
0, 1, \ldots, \frac{N_s}{2} & N_s \text{ even} \\
\\
0, 1, \ldots, \frac{N_s - 1}{2} & N_s \text{ odd}
\end{cases}
\tag{10}
$$

Given an external load applied on the j-th sector, a Fourier transformation process is used to convert it into an equivalent set of loads applied on the basic and duplicate sectors, whose displacement fields $[(U_B)_k, (U_D)_k]$ are computed individually for each value of the harmonic index. The displacement field for the entire structure is obtained via superposition of the single contributions [2]:

$$
\begin{aligned}
U_j = \sum_{k=0}^{\max(k)} & (U_B)_k \cos\left[(j-1)k\alpha\right] \\
& - (U_D)_k \sin\left[(j-1)k\alpha\right], \quad j = 1, \ldots, N_s
\end{aligned}
\tag{11}
$$

where the relationship also holds for the stress and strain field.

In order to excite the cyclic structure at a natural frequency $\omega_{n,k}$, a forcing function $\mathbf{F}$ of the following form is to be applied on the disk sectors:

$$
\mathbf{F}_j = \mathbf{F}_o e^{\left[\omega t + 2\pi k \frac{(j-1)}{N_s} + \frac{2\pi}{N_s}\lambda\right]}, \quad j = 1, \ldots, N_s
\tag{12}
$$

where $\mathbf{F}_o$ is the force amplitude, ω is the excitation frequency, and the integer λ accounts for the arbitrariness that is still available phase-wise, after the coordinate system is assigned for the entire disk model, due to the possibility of arbitrary numbering of the sectors. The effect associated with such an angular shift is a rigid rotation of the forced-response deformation by an amount $\alpha\lambda$, which represents an additional degree of freedom within the response estimation procedure. A similar arbitrariness also appears in the modal analysis, where two modes associated with the same natural frequency $\omega_{n,k}$ may exist. The relationship between these so-called double modes, $\phi_{n,k}^{(1)}$ and $\phi_{n,k}^{(2)}$, is given by

$$
\phi_{n,k}^{(1)} = \phi_{n,k}^{(2)} e^{i\frac{2\pi}{N_s}\gamma}, \quad \gamma = \text{arbitrary integer}
\tag{13}
$$

where, in general, $\gamma \neq \lambda$.

In a case where two modes with the same frequency are excited, it is necessary to account for the angular shifts between the repeated modes and the forced deformation itself, before the maximum vibratory response can be estimated via modal scaling. This situation is from henceforth referred to as a double-mode case. In such a scenario, according to equation (4), the forced response at the peak frequency ω_p near the natural frequency $\omega_{\bar{n},\bar{k}}$ can be approximated, at any point $\mathbf{x}$ of the structure, as:

$$\varepsilon(\omega_p, \mathbf{x}) = \beta_1 \phi_{\bar{n},\bar{k}}^{(1)}(\mathbf{x}) + \beta_2 \phi_{\bar{n},\bar{k}}^{(2)}(\mathbf{x}) \, , \, (\beta_1, \beta_2) \in (\Re, \Re) \tag{14}$$

where the two sensor measurements, $\varepsilon(\omega_p, \mathbf{x}_b)$ and $\varepsilon(\omega_p, \mathbf{x}_c)$ $(1 \leq b, c \leq N_g)$, are sufficient to compute the coefficients β_1 and β_2:

$$\left\{ \begin{array}{c} \bar{\beta}_1 \\ \bar{\beta}_2 \end{array} \right\} = \left[\begin{array}{cc} \phi_{\bar{n},\bar{k}}^{(1)}(\mathbf{x}_b) & \phi_{\bar{n},\bar{k}}^{(2)}(\mathbf{x}_b) \\ \phi_{\bar{n},\bar{k}}^{(1)}(\mathbf{x}_c) & \phi_{\bar{n},\bar{k}}^{(2)}(\mathbf{x}_c) \end{array} \right]^{-1} \left\{ \begin{array}{c} \varepsilon(\omega_p, \mathbf{x}_b) \\ \varepsilon(\omega_p, \mathbf{x}_c) \end{array} \right\} \tag{15}$$

The two gauges are not to be placed on the same sector so as not to have a redundant set of equations. Finally, the estimated maximum vibratory condition ε_M^{p*} can be obtained through maximization of equation (14):

$$\varepsilon_M^{p*} = \max_{\mathbf{x}} \| \bar{\beta}_1 \phi_{\bar{n},\bar{k}}^{(1)}(\mathbf{x}) + \bar{\beta}_2 \phi_{\bar{n},\bar{k}}^{(2)}(\mathbf{x}) \| \tag{16}$$

which, in the special case of double modes, substitutes equation (8) within the response inference process.

2.4   Sources of Uncertainty

At this stage, the types of uncertainties being considered include sensor-based, modeling and input uncertainties. The first type is associated with the limited knowledge of system dimensions (for instance, due to tolerances) and material characteristics. The second and third kind are introduced, respectively, to account for several sources of uncertainty due to out-of-control experimental conditions and/or instrumentation limitations (e.g., measurement inaccuracy, sensor sensitivity to external conditions), and to study the effect of a discrepancy between the physical system and the analytical (or numerical) model.

25

2.4.1 Input Uncertainty

Uncertainty in a physical system's material characteristics (e.g., Young's modulus or density) and dimensions due, for instance, to manufacturing imprecision and machine tolerances can cause the "true" (but unknown) inputs to the model to deviate from the "nominal" values (i.e., used in the model), thus leading to a difference in response between the actual system and the prediction model.

2.4.2 Sensor-based Uncertainties

The estimation of a system's maximum response also is affected both by uncertainty in the amplitudes read by the sensor, and by limited knowledge of its exact placement. Uncertainty in a sensor's reading can be caused by several factors, which include, among others, measurement noise, response non-linearity, and/or a strain gauge's imperfection in its adhesion to the component. The impact of a sensor measurement error on the response estimation has been investigated by perturbing the recorded amplitude $\varepsilon(\omega, \mathbf{x}_g)$ by a random error $A\,\eta_g$. More specifically, the following formulation has been adopted:

$$\hat{\varepsilon}(\omega, \mathbf{x}_g) = \varepsilon(\omega, \mathbf{x}_g) + A\,\eta_g \tag{17}$$

$$\eta_g \sim N\left(0, \sigma_g\right), \quad g = 1, \ldots, N_g$$

where $\hat{\varepsilon}(\omega, \mathbf{x}_g)$ defines the perturbation of the measured vibratory amplitude with respect to the nominal value $\varepsilon(\mathbf{x}_g, \omega)$, and η_g has been assumed to be a normally distributed non--dimensional quantity with zero mean and standard deviation σ_g. Uncertainty is introduced through the sensor's noise parameter A, defined herein as a percentage of the maximum response amplitude for the mode identified by the estimation process defined in equation (5). This definition is an attempt to account for uncertainty in the sensor measurements, while at the same time removing the dependence of A upon the sensor's reading and, indirectly, position on the component. In fact, in a test, sensors of the same type, placed at different locations, may be subject to quite different conditions (e.g., pressure, temperature, or loads) which may significantly affect their accuracy across the same measurement range. At present, no specific type of sensor (e.g., NSMS, strain gauges or accelerometers) has

been taken into consideration. A more *ad hoc* definition for η_g may be needed, however, when considering a given sensor type so as to account for its specific characteristics and gain better and more realistic insight.

Uncertainty associated with sensor location can be introduced in a similar fashion, i.e. by perturbing the modal information at the gauges' positions before using it in equation (6):

$$\hat{e}_p(\mathbf{x}_g) = e_p(\mathbf{x}_g + \boldsymbol{\zeta}_g), \quad g = 1, \dots, N_g \tag{18}$$

where $\boldsymbol{\zeta}_g$ represents the difference between nominal and actual position of the sensor on the structure. Since the real sensor's location is uncertain, $\boldsymbol{\zeta}_g$ is treated as a random quantity, which, however, still needs to satisfy given geometry constraints (e.g., surface contact between strain gauge and component). Given the geometry-dependent nature of this approach, more detailed discussions are provided in subsequent sections, where specific geometric configurations are addressed.

2.4.3 Modeling Uncertainty

Another source of uncertainty that may affect the effectiveness of the inference process is represented by the limited accuracy of the system model at hand. Among the several factors influencing model fidelity, attention is given to the effect of a mismatch between experimental and numerical mode shapes used to perform the estimation. Such a discrepancy is reproduced by perturbing the model mode shapes so as to simulate those circumstances in which the model is not capable of capturing entirely the behavior of the tested unit. Given the experimental mode shape $\phi_i^{(e)}$ and the corresponding model mode shape $\phi_i^{(m)}$ ($i = 1, 2, \dots, N_m$), the mismatch between the two is introduced as follows:

$$\phi_i^{(e)} = \sum_{j=-1}^{1} w_{i-j} \phi_{i-j}^{(m)} \tag{19}$$

In this case, the experimental mode $\phi_i^{(e)}$ is expressed as a linear combination of the i-th mode shape and its immediate neighbors in frequency, through the set of weights (w_{i-1}, w_i, w_{i+1}).

The correlation between experimental and model modes (or between perturbed and unperturbed modes in case of computer simulated experiments) can be established through

27

the Modal Assurance Criterion (MAC) [1]:

$$MAC_{q,t} = \frac{\left| \phi_q^{(e)T} \phi_t^{(m)} \right|^2}{\left| \phi_q^{(e)T} \phi_q^{(e)} \right| \left| \phi_t^{(m)T} \phi_t^{(m)} \right|}, \ q, \ t = 1, 2, \ldots, N_m \tag{20}$$

The MAC matrix is close to an identity matrix when good correlation exists between the two sets of mass-normalized mode shapes. In this particular setting of simulated experiments, it also offers a way to quantify the amount of perturbation introduced by a given set of weights.

2.5 *Uncertainty Propagation in the Beam-like Blade Model*

The response estimation methodology introduced in Section 2.2 has been evaluated against the input, modeling, and measurement-based uncertainties introduced previously, first in the case of a beam-like blade and then for a realistic disk sector, both instrumented with two sensors, S_1 and S_2.

The beam-like blade being considered is part of the simplified rotor model shown in Figure 1. Stresses and displacements in the blades are computed for assigned inputs and loading conditions (i.e., amplitude, excitation frequency ω, and point of application along the blade), engine operating condition (i.e., the angular velocity Ω_o), as well as the blade geometry and material characteristics (Table 1). It is standard practice to synthesize stresses and displacements in the form of Campbell diagrams, which summarize the response amplitudes over the considered ranges of excitation frequencies and rotor speeds. An example of a typical Campbell diagram is given in [4] and reproduced in Figure 3, where regions of high stress levels, so-called "resonance blossoms", can be identified for the rotating system under investigation. Each of these resonance responses originates from the intersection of an engine order excitation with one of the structure's natural frequencies. A system's maximum vibratory response obtained from the Campbell diagram can then be combined with its static response in a Goodman diagram to assess the risk of fatigue failure.

2.5.1 Input Uncertainty

The effect of an input uncertainty propagation is addressed through a sensitivity study
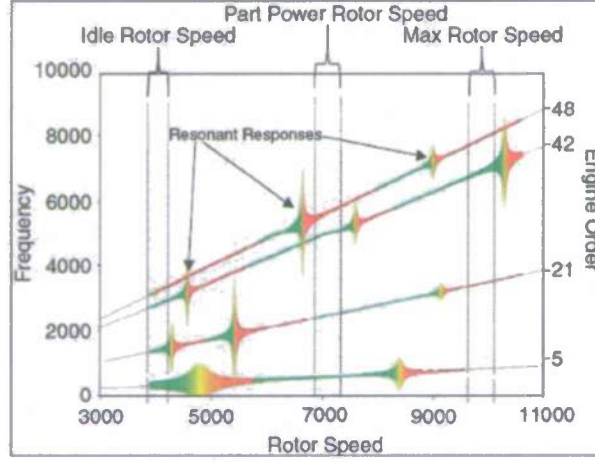
Figure 3: Typical Campbell diagram for a rotating system.

Table 1: Beam geometry and properties.

Quantity	Symbol	Value
Length	L_o	22.5 cm
Thickness	T_o	2 cm
Chord	C_o	15.3 cm
Density	ρ_o	4430 Kg/m^3
Young's modulus	E_o	114 GPa

on the Goodman diagram, where variations both in geometry (i.e., length L_o, cross-section dimensions T_o and C_o) and material properties (i.e., E_o and ρ_o) have been evaluated using the system model of Table 1. For this particular system, a point Σ on the Goodman diagram is identified as:

$$\Sigma = \left(\sigma_{a_M}, \sigma_m \right) \tag{21}$$

where the maximum longitudinal alternating stress σ_{a_M} on the blade is herein defined as

$$\sigma_{a_M} = \max_{\Omega_o, \omega} \left(\max_x |\sigma_a(x)| \right), \quad 0 \le x \le L_o \tag{22}$$

so as to account for both the operating condition Ω_o and the excitation frequency of the forcing function. The mean stress σ_m corresponds, instead, to an equivalent mean load statically applied at the blade's tip. As an example, illustrated in Figure 4 is the effect of a 2% variation in chord and thickness, where the perturbations have been assumed to

29

(a) Overview   (b) Detail
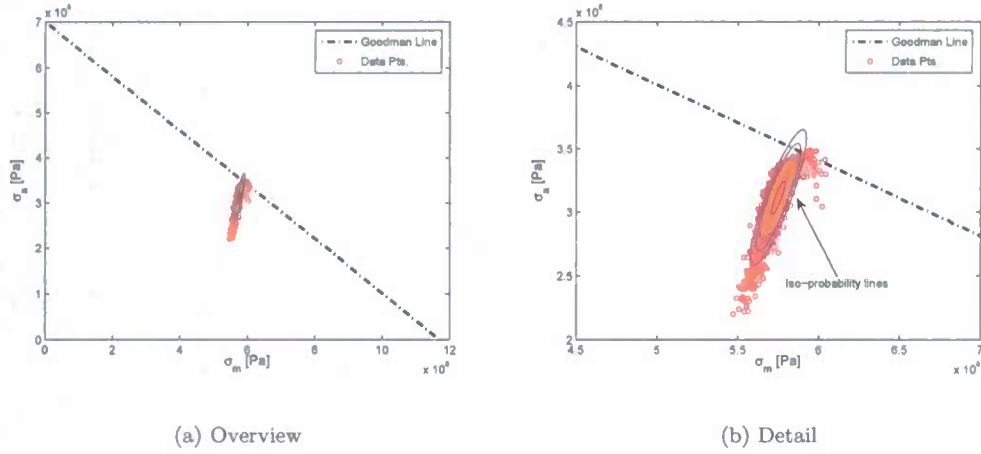
Figure 4: Goodman diagram for a single beam-like blade: effect of uncertainty in C_o and T_o upon the stress levels.

have a normal distribution. As can be observed from the plot, some combinations of beam cross-section dimensions may cause the structure to be significantly close to its fatigue limit or to exceed it. A sensitivity study on beam length produced a similar spread of the stress levels, whereas no significant scatter in the response was observed when varying the material properties.

2.5.2 Sensor-related Uncertainties

Uncertainty in sensors' readings and locations have been investigated via 10,000-run Monte Carlo simulations. The effect of a sensor measurement error upon the estimate of a system's response has been introduced according to equation (17) with the assumption that $\sigma_{g=1,2} = \sigma = 0.01$. Furthermore, taking into account the one-dimensional nature of the beam analysis, uncertainty in the location of the g-th sensor is expressed by means of equation (18) with the nominal position x_g being perturbed in the following manner:

$$
\begin{aligned}
\hat{x}_g &= x_g + L_r\, \zeta_g \\
\zeta_g &\sim N\left(0, \sigma_g\right), \quad g = 1, 2
\end{aligned}
\tag{23}
$$

where $x_1 = 0.25 L_o$, $x_2 = 0.75 L_o$ and the perturbed location $\hat{x}_g$ is computed in terms of a reference length L_r, chosen to be equal to half of the blade span L_o.

30
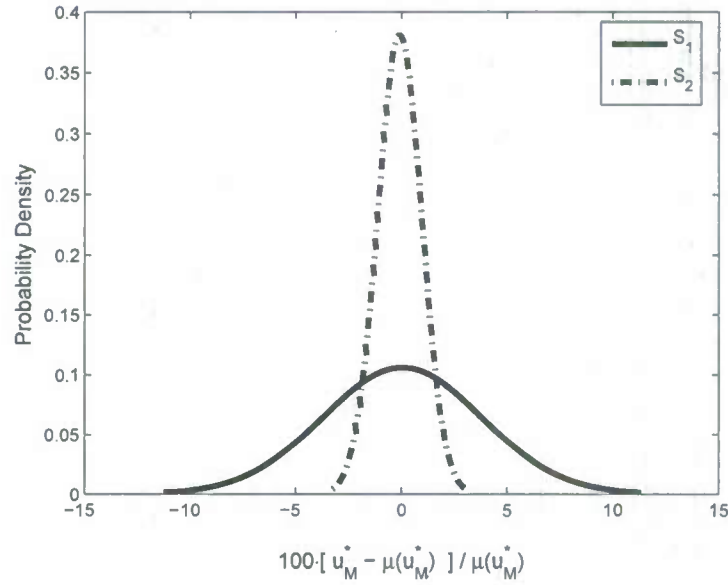
Figure 5: Beam: variability in the maximum-displacement estimate due to uncertainty in the sensor locations perturbed separately ($\sigma = 0.01$).

In order to address their individual impact upon estimation accuracy, uncertainties in sensor measurement and position have been addressed separately. Despite the fact that this distinction may be somewhat hard to make in real test conditions, it still offers valuable insight with respect to uncertainty propagation. The effect of each source of uncertainty has been investigated and quantified through 10,000-run Monte Carlo simulations, where a non-dimensional variance σ^2 equal to 0.01^2 has been assumed for all the case studies. Furthermore, results are presented in the form of a variability in the absolute error, defined as the difference between the estimate obtained from the inference process and the actual response resulting from a forced harmonic analysis conducted on the system model.

Shown in Figures 5 and 6 is the variability, due to uncertainty in sensor positions, in the estimates of the maximum displacement u_M^* and maximum axial stress amplitude $\sigma_{x_M}^*$, both computed according to equation (8) at the second resonance condition (i.e., the omitted superscript $p = 2$). Each plot compares the uncertainty resulting from the perturbation of each sensor separately. Of course, this one-at-a-time approach is an idealization, whereas

31
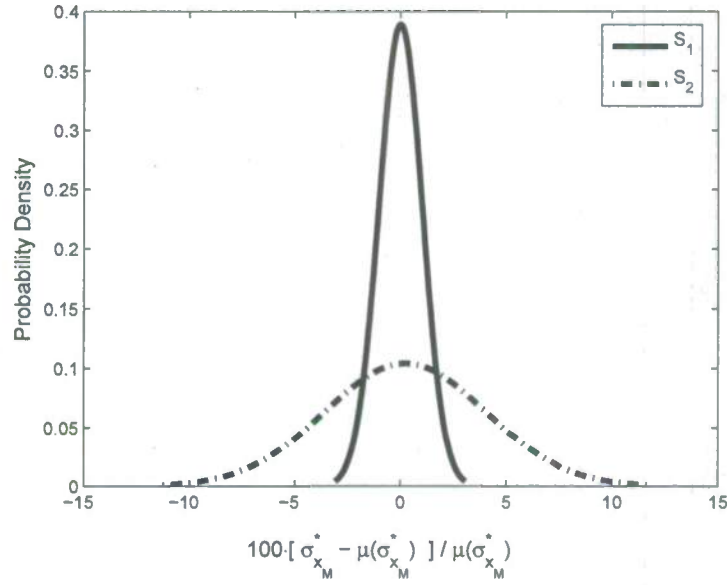
Figure 6: Beam: variability in the maximum-stress estimate due to uncertainty in the sensor locations perturbed separately ($\sigma = 0.01$).

a larger uncertainty may result from both sensors being in non-nominal conditions at the same time, which could affect the mode identification process through the ratio $\frac{e(x_1)}{e(x_2)}$, as well as the accuracy of the estimates due to the coupling between the perturbed sensor position $\hat{x}_g$ and the amplitude $e_p(x)$ of the selected mode at that location. Illustrated in Figure 7 is the case in which both sensors' positions have been randomly varied simultaneously. In this circumstance, the estimates' variability appears to be skewed. This behavior, however, has no physical basis, but it is merely due to the discrete nature of equation (8), where one estimate was probabilistically higher than the others, hence prevailing in the maximization process. When treated individually, each estimate exhibited a normally distributed trend similar to that of Figures 5 and 6. Overall, despite their limited validity due to the simple nature of the system and the sensor's point representation, these results highlight how the variability in stress and displacement estimates depends significantly upon the location where measurements are taken, thus suggesting the need for optimal placement of the instruments together with a better and more accurate description of their characteristics
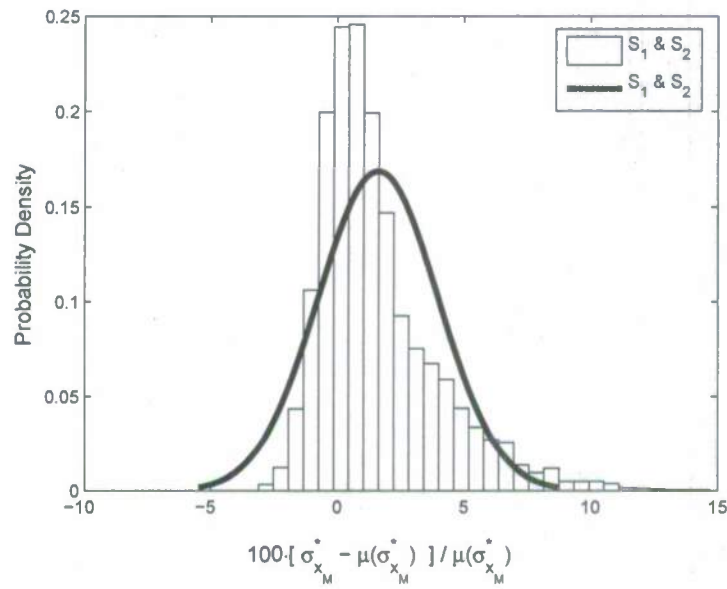
Figure 7: Beam: variability in the maximum-stress estimate due to uncertainty in both sensor locations ($\sigma = 0.01$).

[75, 89].

The effect of an uncertainty in sensor readings is illustrated in Figure 8. The results were obtained by varying only one measurement data set at a time, while assuming a 100% accuracy for the other sensor. Similarly to what was observed when varying the sensor locations, the results show that the response estimates are characterized by a different level of variability for each of the sensors, which could be related to the difference in the signal-to-noise ratio at the various instrumented locations. Therefore, this behavior suggests that the effect of a measurement uncertainty could also depend upon sensor placement, thus making any distinction between the two sources of uncertainty more difficult to draw. Finally, when both sensors' measurements were varied simultaneously, results similar to those depicted in Figure 8 were observed. This is exclusively due to the fact that the estimates in equation (8) are only coupled through $e_p(x)$, and the same mode shape was always selected regardless of whether only one or both sensor readings were being perturbed.
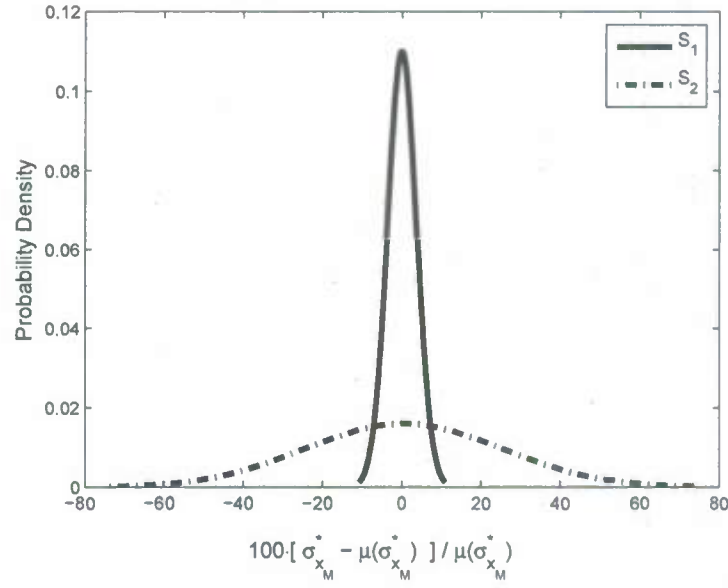
Figure 8: Beam: variability in the maximum-stress estimate due to uncertainty in the sensor readings perturbed separately ($\sigma = 0.01$).

2.5.3 Modeling Uncertainty

In order to study the effect of modeling uncertainty for the beam-like blade system, its mode shapes were perturbed using two sets of weights in equation (19), where each group of weights represented a model of different accuracy. The nominal and perturbed system models were compared by means of their MAC matrices, depicted in Figure 9, according to which configuration MAC_2 indicates a better correlation between perturbed and unperturbed quantities. The MAC is a common and widely accepted means to assess the degree of correlation between perturbed and unperturbed modes, or between a physical system and its analytical representation. In order to evaluate the effect of modeling uncertainty on the prediction of a system's response, the perturbed modes $\phi^{(e)}(x)$ were used in conjunction with a random variation of the sensor locations:

$$
\hat{\phi}_i^{(e)}(x_g) = \phi_i^{(e)}\left(x_g + L_r\zeta_g\right), \quad i = 1, \ldots, N_m
$$
$$
\zeta_g \sim N\left(0, \sigma_g\right), \quad g = 1, 2
$$

(24)

where the Gaussian quantity ζ_g represents the variability associated with the g-th sensor
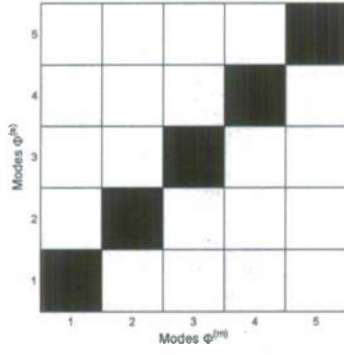
(a) MAC$_1$: $w_{-1} = 0$, $w_0 = 1$, $w_1 = 0$
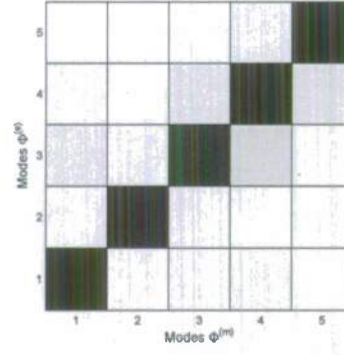
(b) MAC$_2$: $w_{-1} = 0.1$, $w_0 = 0.8$, $w_1 = 0.1$
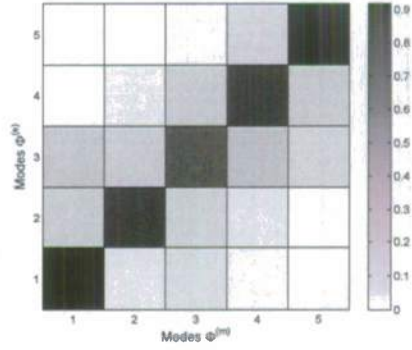
(c) MAC$_3$: $w_{-1} = 0.15$, $w_0 = 0.7$, $w_1 = 0.15$

Figure 9: Beam: MAC matrices for modeling uncertainty ($N_m = 5$).

position. Depicted in Figure 10 are three probability density functions for the stress quantity $\sigma^*_{x_M}$, corresponding to the three MAC matrices of Figure 9 and obtained via Monte Carlo simulations with $\sigma_{g=1,2} = \sigma = 0.01$. The beam was assumed to be instrumented with only one strain gauge, and the response estimates were obtained by substituting equation (24) into equation (8). For this simple model, Figure 10 indicates that less modeling uncertainty yields lower variability in the response estimates, hence higher prediction confidence.
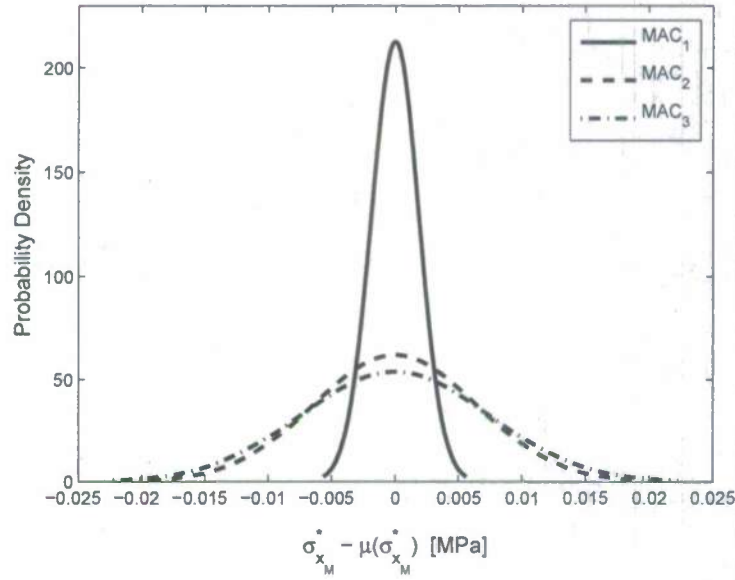
Figure 10: Beam: variability in the maximum-stress estimate due to modeling uncertainty via mode shape perturbation.

2.6 Uncertainty Propagation in the Bladed Disk Model

The same analysis process illustrated earlier has also been employed for the estimation of the critical vibratory response of a compressor rotor disk representative of the system treated in [86], whose characteristics are listed in Table 2. Due to the lack of experimental data, harmonic analyses with various cyclic loading conditions have been conducted on the finite-element model of Figure 2 to simulate different testing conditions. Measurement data were obtained for different ranges of the excitation frequency, where periodic loads of the form given by equation (12) were applied on the blades' tips in radial or transverse direction. Two sensors, S_1 and S_2, were considered at locations on the outward part of the blade's span, one on the pressure surface and the other on the suction surface of two distinct blades, four sectors apart. The other set of information needed for the estimation of the maximum forced response was obtained through modal analysis. Listed in Table 3 are the structure's natural frequencies obtained through the finite-element model, while depicted in Figure 11 is one pair of its double mode shapes.

Table 2: Bladed disk characteristics.

Quantity	Symbol	Value
Blade height	H_b	5.08 cm
Blade chord	C_b	12.7 cm
Disk outer radius	R_h	10.16 cm
Shaft radius	R_s	1.27 cm
Disk thickness	T_d	1.52 cm
Material	Ti-6-4	-

Table 3: Bladed disk natural frequencies.

$$\omega_{n,k} \ [\text{Hz}]$$

	Harmonic Index			
Mode	$k = 0$	$k = 1$	$k = 2$	$k = 3$
$n = 1$	1071.9	839.37	1190.1	1414.5
$n = 2$	1231.4	839.37	1190.1	1414.5
$n = 3$	1946.1	1609	1846.4	3085.1
$n = 4$	3378.4	1609	1846.4	3085.1
$n = 5$	5434.6	3374.4	3390.6	3499.8
$n = 6$	6977.6	3374.4	3390.6	3499.8
Mode	$k = 4$	$k = 5$	$k = 6$	$k = 7$
$n = 1$	1441.6	1449.2	1452.1	1453.2
$n = 2$	1441.6	1449.2	1452.1	1453.2
$n = 3$	3346.2	3361.3	3366.4	3368.9
$n = 4$	3346.2	3361.3	3366.4	3368.9
$n = 5$	4554.3	5428.7	5987.5	6333.4
$n = 6$	4554.3	5428.7	5987.5	6333.4

Presented next are some case studies which illustrate the effects of sensor-related uncertainties, modeling accuracy as well as their combined impact and propagation, where the vibratory response of the structure has been investigated in the form of Von Mises stresses at various resonance conditions. The predicted maximum Von Mises stress $\sigma^*_{VM_M}$ has been computed through equation (8) for a single-mode case, or via equation (16) for double-mode cases.
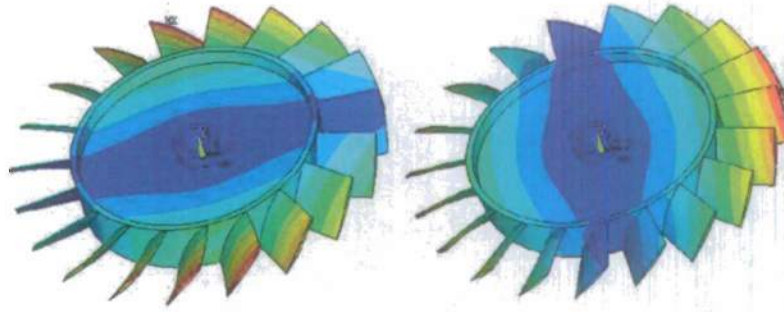
Figure 11: Bladed disk: double modes at $\omega_{1,1} = \omega_{2,1} = 839.37$ Hz.

2.6.1 Sensor Measurement Error and Location Uncertainty

Measurement errors are herein introduced according to equation (17) described in Section 2.4.2, where the perturbation to the nominal measurements is assumed to be normally distributed with $\sigma = 0.01$, while the gauge noise A is considered equal for all the sensors. Shown in Figure 12 is the variability of $\sigma^*_{VM_M}$ obtained via a Monte Carlo simulation in which only the readings of sensor S_1 were assumed to be affected by uncertainty. As it can be observed, the interpolated probability distribution fits the simulation histogram data quite well. Depicted in Figures 13 and 14 is instead a comparison between the probability density functions of the two estimates, with sensor measurements perturbed separately and concomitantly. Figure 13 reveals that a reading uncertainty affecting only sensor S_2 causes the stress estimate's relative error to have a smaller spread when compared with the estimate's variability associated with just a measurement error in the other sensor. An opposite result can, instead, be observed in Figure 14. Of course, in the particular case of a double mode being excited, both sensor readings do play a role in the estimation process via equation (15), thus making it difficult to assess their relative impact on the resulting uncertainty. Furthermore, the effect of sensor positioning is also present through the values of the modal quantities at the given locations, which could reduce or amplify a given uncertainty. Finally, illustrated in Figure 14 is also the effect of both sensor readings being varied at the same time, for which case the overall spread of the estimated forced response appears to worsen.
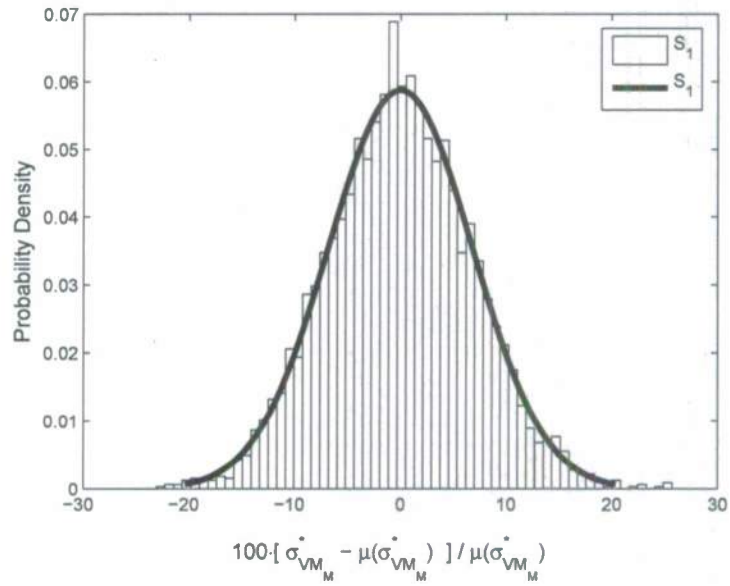
Figure 12: Bladed disk: variability in the maximum-stress estimate due to uncertainty in the reading of sensor S_1 ($\omega_{1,0} = 1071.9$ Hz).
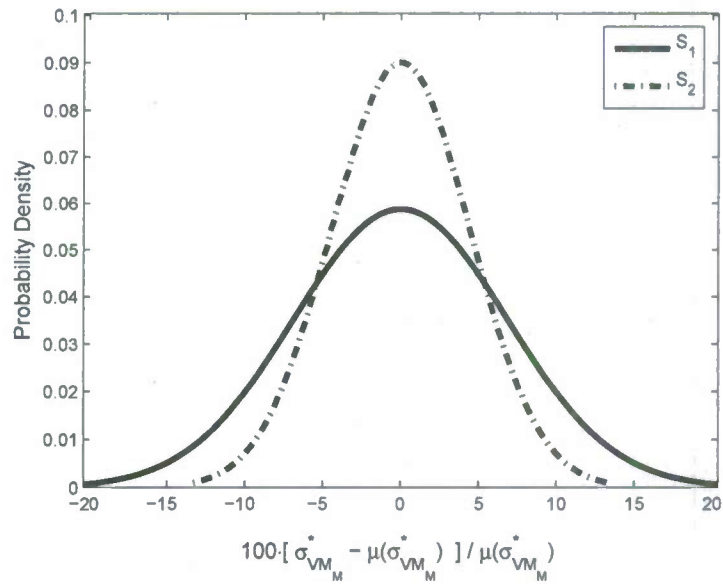
Figure 13: Bladed disk: sensor-based comparison of variabilities in the maximum-stress estimate due to uncertainty in the sensor readings perturbed separately ($\omega_{1,0} = 1071.9$ Hz).
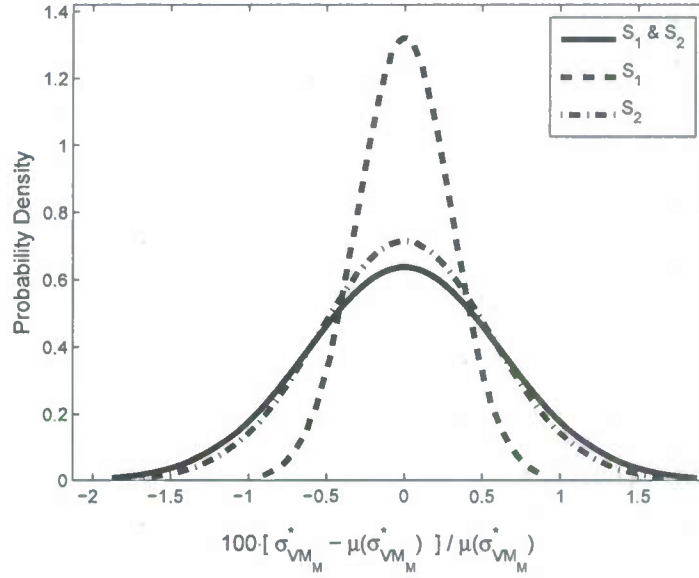
Figure 14: Bladed disk: sensor-based comparison of variabilities in the maximum-stress estimate due to uncertainty in the sensor readings ($\omega_{3,6} = \omega_{4,6} = 3366.4$ Hz).

Uncertainty in sensor location is introduced by replacing the modal information corresponding to the sensors' nominal locations with modal values associated with their perturbed positions. In this instance, however, sensors were placed on the suction and/or pressure surfaces of the blade for which no analytical formulation was available, thus requiring numerical interpolation. The nominal position of a sensor, (x_o, y_o, z_o), is such that

$$z_o = f(x_o, y_o) \tag{25}$$

where $f(x, y)$ represents the equation of the blade's suction or pressure surface in the xy plane perpendicular to the disk rotational axis. The suction and pressure surfaces are treated separately simply to have a well-posed problem, since f^{-1} cannot otherwise be defined univocally. Obviously, any perturbed position $(\hat{x}_o, \hat{y}_o, \hat{z}_o)$ needs also satisfy such a constraint so as to guarantee full contact between blade and sensor as well as to preserve the condition of zero-intersection between them. That is achieved by computing $\hat{z}_o = f(\hat{x}_o, \hat{y}_o)$ via linear interpolation over the surface finite-element mesh. Uncertainty in sensor locations has been implemented by generating a statistical realization around the projection onto the

xy plane of each sensor's position and by computing the corresponding modal information to be used within the estimation process. In order to avoid the results being artificially skewed due to the orientation of the blade with respect to the xy plane, the two-dimensional and normally-distributed realization is such as to be bounded by the projection of a circle of radius L_r centered at (x_o, y_o, z_o) and tangent to the blade. In mathematical terms, in a coordinate system $x'y'$, centered and aligned with the axes of the ellipse created by the circle's projection onto the xy plane, the realization can be written as follows:

$$\hat{x}_o' \sim N(0, r_{x'}/3)$$
$$\hat{y}_o' \sim N(0, r_{y'}/3)$$

(26)

where $r_{x'}$ and $r_{y'}$ are the measures of the ellipse's semi-axes, and a 3σ limit has been utilized. Such a technique has been employed because of its simplicity as well as its capability to control the statistical realization so that it covers the area around a sensor's nominal position in a more regular fashion, without introducing extraneous sources of asymmetry in the estimates.

A study on the impact of sensor location's uncertainty on the accuracy of the estimation technique was performed through Monte Carlo simulations where both sensors were perturbed, according to equation (26), with a reference radius $L_r = 0.15$ cm. A sample of the results is given in Figure 15. Illustrated in the figure is the histogram of the stress estimate's relative error associated with sensor S_2 together with its representative probability density function, constructed under the assumption that the sample data are part of a normally distributed population. The formulated assumption is, however, somewhat in contradiction with the skewness shown by the bar chart. The primary cause of such a behavior is twofold: on the one hand, the modal quantities being perturbed (and interpolated upon) appear in the denominator of equation (6), which causes the scaling modal ratios to no longer have a normal distribution; on the other hand, the estimates' distributions are a one-dimensional synthesis of at least a two-dimensional spatial uncertainty, whose effect depends on the mode shapes and is furthermore filtered by the interpolation scheme. As a matter of fact, it was also determined that if the sensor's nominal position falls in the vicinity of a maximum or minimum of the excited mode shape, the estimates' histograms
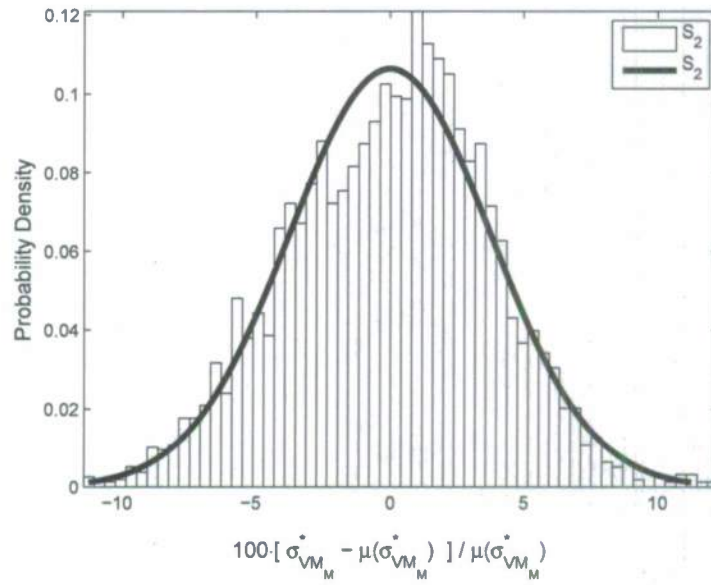
Figure 15: Bladed disk: variability in the maximum-stress estimate due to uncertainty in the sensor locations ($\omega_{1,0} = 1071.9$ Hz).

become even more skewed, thus making the assumption of normality less appropriate, and the estimation itself less meaningful.

As shown by the previous results, response estimates are affected by sensor location. In order to investigate this aspect further, a sensitivity study was also conducted, where nine different nominal positions for each sensor were considered and perturbed as described earlier. The sensors were placed one on each blade surface, where three different nominal positions were considered chord-wise at three locations along the span. Depicted in Figure 16 are the various nominal positions and realizations on the pressure surface for sensor S_1, while Figure 17 shows the corresponding uncertainty levels in the response prediction, with the histograms associated with the probability curves not displayed for the sake of clarity. As observed also for the beam case, results show a dependence of the response estimate's accuracy upon a sensor location, with the relative error ranging from 5% up to 15%, in this particular case. Of course, this raises the issue of optimal positioning of the instrumentation to achieve better accuracy. It can be rather difficult to draw a clear-cut conclusion on where
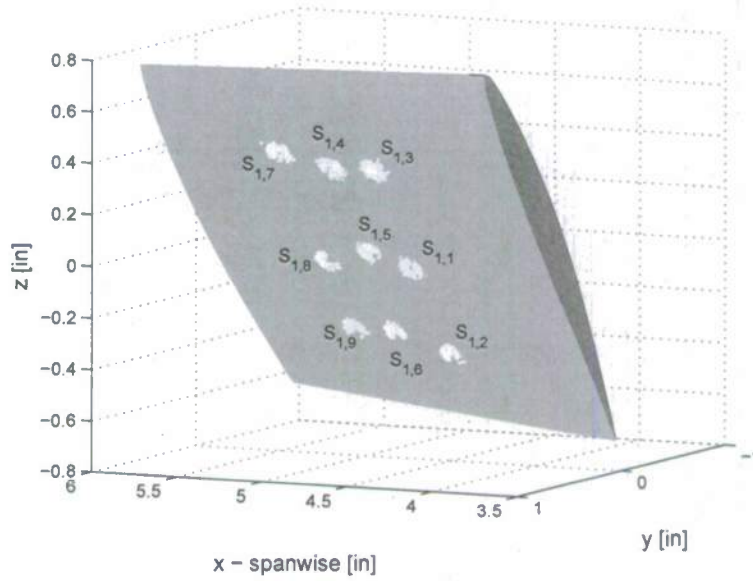
Figure 16: Bladed disk: realization of the position $S_{1,l}$ ($l = 1, \ldots, 9$) of sensor S_1 on the blade's pressure surface.

to place a sensor so as to minimize the error in the inference process. In fact, several factors may come into play, such as magnitudes of the modal quantities near the sensor locations or corresponding gradients, which may not be known *a priori* and typically are unknown until more information is available about the external forcing function or about which mode will presumably be excited. Regions of very low magnitude or strong gradients give rise to very large spreads in the estimates, whereas the prediction process fails when a sensor is placed rather close to a node of the given selected mode. Predicting the sensors' optimal positions can become even more challenging when double modes are excited, as the manner in which they superpose is dictated by equation (15) containing an implicit dependence upon the sensor locations for which optimization is indeed being pursued. On the other hand, modal ratios at the sensor positions could provide initial insight in the case of single modes.

2.6.2 Modeling Uncertainty

As previously exemplified for the beam-like blade, uncertainty in the finite-element model of the disk is introduced by perturbing the model mode shapes according to equation
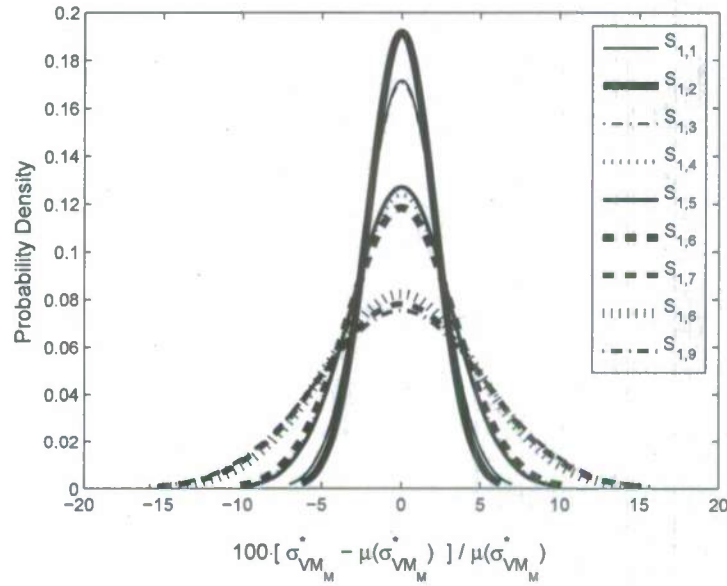
Figure 17: Bladed disk: variability in the maximum-stress estimate due to uncertainty in the location $S_{1,l}$ $(l = 1, \ldots, 9)$ of sensor S_1 $(\omega_{1,0} = 1071.9$ Hz$)$.

(19) and by using the modified quantities within the inference procedure. Three MAC configurations, each of which represents a different level of perturbation of the model mass-normalized modes, are shown in Figure 18, where the presence of numerical noise in the finite-element solution is also highlighted by the non-zero off-diagonal terms of the matrix corresponding to the no-perturbation scenario. The combined effect of sensor reading error and modeling uncertainty is depicted in Figures 19 and 20 for the double-mode case at frequency 839.37 Hz, where the only difference between the two graphs is the different normalization scheme used for the estimate. In this circumstance, according to Figure 19, distinct MAC configurations result in very similar spreads in the relative error of the stress estimate, while Figure 20 illustrates how a higher modal perturbation results in higher bias and lower variance. This was not always the observed trend, as other cases instead showed an increase both in bias and spread for the inferred stresses. An example of such a situation is illustrated in Figures 21 and 22 for the double mode at natural frequency 3366.4 Hz.
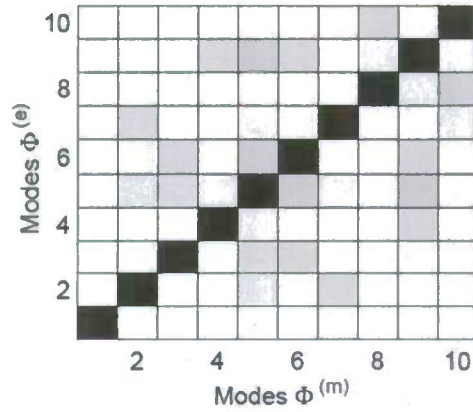
(a) MAC_1: $w_{-1} = 0$, $w_0 = 1$, $w_1 = 0$
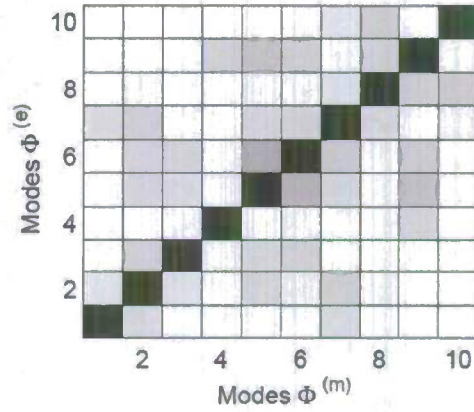
(b) MAC_2: $w_{-1} = 0.075$, $w_0 = 0.85$, $w_1 = 0.075$
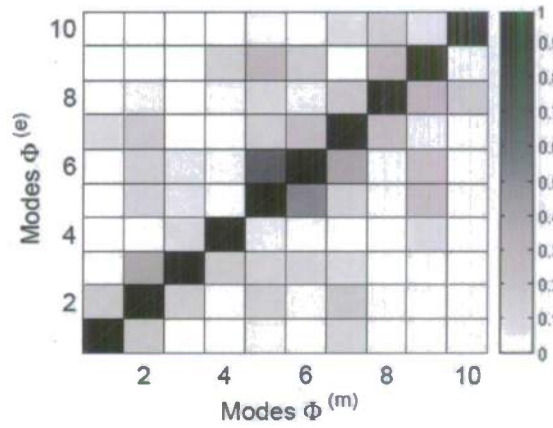
(c) MAC_3: $w_{-1} = 0.15$, $w_0 = 0.70$, $w_1 = 0.15$

Figure 18: Bladed disk: MAC matrices representing three levels of modeling uncertainty ($N_m = 10$).
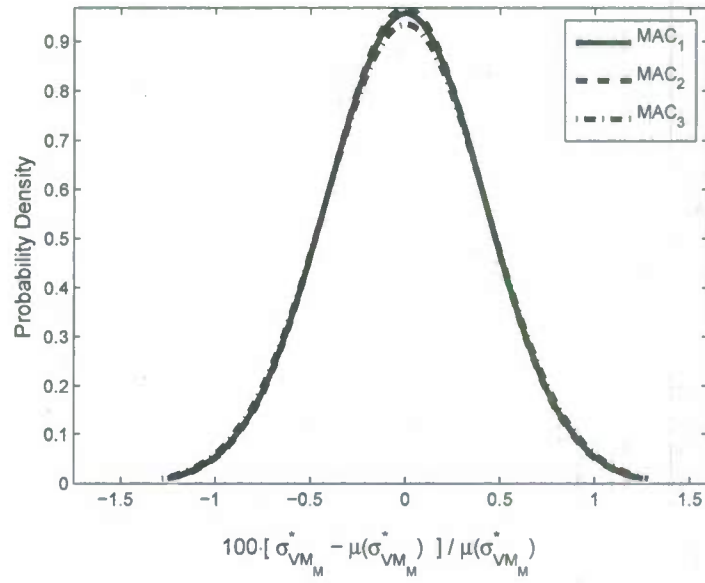
Figure 19: Bladed disk: variability in the maximum-stress estimate for different MAC matrices ($\omega_{1,1} = \omega_{2,1} = 839.37$ Hz).
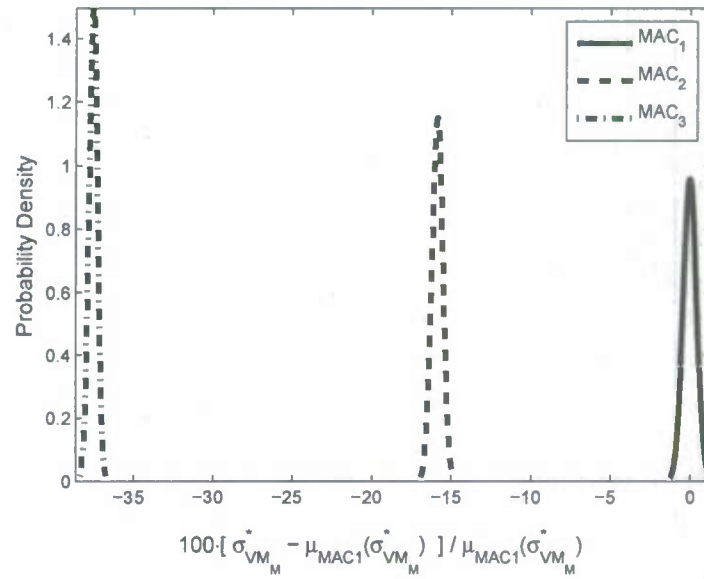
Figure 20: Bladed disk: variability in the maximum-stress estimate for different MAC matrices ($\omega_{1,1} = \dot{\omega}_{2,1} = 839.37$ Hz).
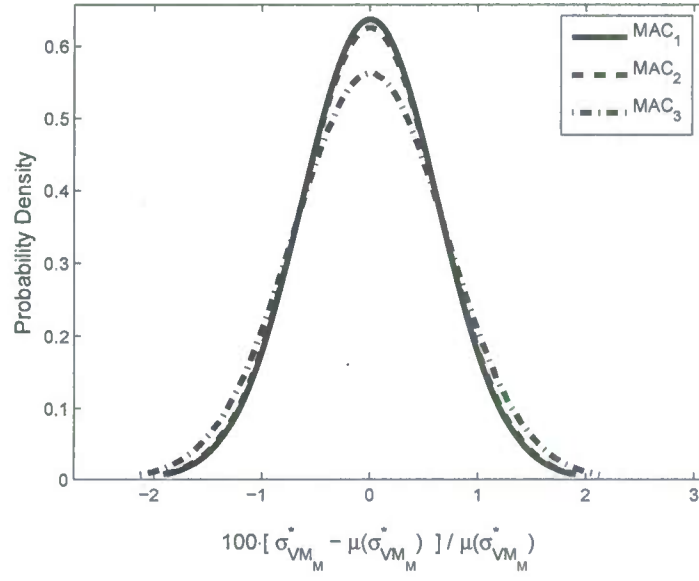
Figure 21: Bladed disk: variability in the maximum-stress estimate for different MAC matrices ($\omega_{3,6} = \omega_{4,6} = 3366.4$ Hz).
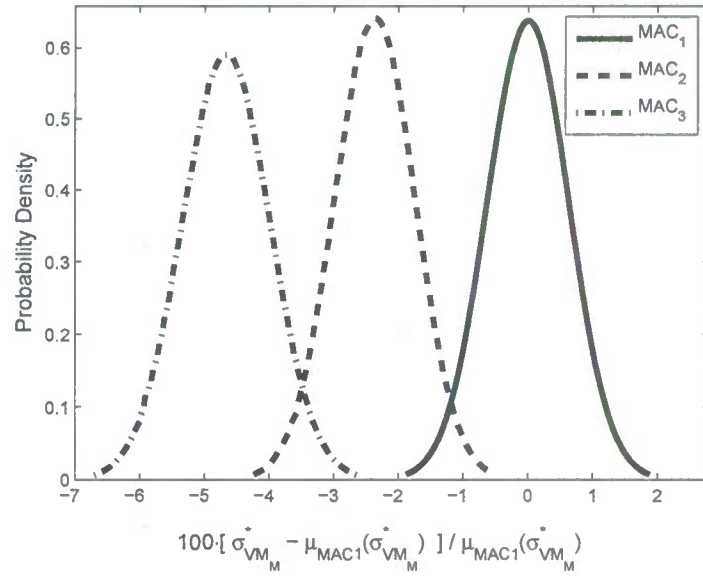
Figure 22: Bladed disk: variability in the maximum-stress estimate for different MAC matrices ($\omega_{3,6} = \omega_{4,6} = 3366.4$ Hz).

2.7 Summary

The impact of uncertainty upon a model-based approach for the prediction of a system's vibratory response has been assessed for two distinct models. Among the several classes of uncertainty that exist, attention was given primarily to instrumentation-based and system model inaccuracies, through a variation of sensor locations, measurement data, and mode shapes. Uncertainties have been modeled by randomly perturbing the nominal values of given quantities (e.g., test data or model input parameters) and their impact has been investigated through a probabilistic analysis via Monte Carlo simulations.

The existence of sensor-based uncertainties highlighted the fact that an instrument's location may affect the accuracy and confidence level of a given response estimate both explicitly and implicitly. More in detail, in the presence of only measurement errors, the difference among the resulting variabilities in the estimated quantities is similar to the one observed in the case of only sensor location uncertainty. This trend originates from the locations themselves at which the response is measured and it indicates that the effects of both sources of uncertainty may not always be clearly separated. Of course, a more complex system geometry and the presence of double mode shapes make it more difficult to anticipate how uncertainty and inaccuracies propagate within the response inference process.

System model assumptions and limitations constitute another source of uncertainty, as the model itself may be incapable of describing the real component in a complete and exhaustive fashion. Based on the obtained results, an increasing mismatch between the physical system's measured behavior and its numerical representation contributes to the amplification of the impact for any other source of uncertainty already affecting the accuracy of the prediction procedure. More specifically, a growing modeling uncertainty was observed to cause an increase in the estimate's bias and spread, or an increase in bias accompanied by a counterintuitive shrinking of its spread. Overall, modeling uncertainties result in a further lessening of the confidence level associated with the response estimates.

CHAPTER III

STATISTICAL ANALYSIS OF VARIABILITY IN EXPERIMENTAL DATA

3.1 Overview

The previous chapter demonstrated the sensitivity of the stress prediction process to uncertainty in sensor location and geometric/material properties, where simulated measurement data were employed. Of course, in practical applications, the vibratory response of a dynamic structure is computed by means of a combination of both experimental and analytical results. Therefore, the analysis is herein extended and applied to real test data, so that the inherent physical uncertainties related to sensor placement, accuracy and orientation, gauge sensitivity and calibration, as well as the presence of noise in the data can be explicitly accounted for. Moreover, in the presence of real experimental data, any existing discrepancy between the physical system and its numerical model is emphasized further, thus making explicit the impact of modeling approximations upon the estimates' accuracy. The process is demonstrated on a set of experimental data obtained from tests on simple plate structures, and processed according to procedures used for engine blade testing. The analysis is aimed at providing initial insight in terms of isolating the various sources of uncertainty and error in a real experimental setting.

3.2 Experimental Setup

In the absence of experimental data for turbine blades, a series of experiments were conducted on three distinct $9 \times 4 \times 0.125$ inch plates, each made of a different material, i.e. brass, copper and steel. Each plate was cantilevered along one of its width sides and instrumented with $N_g = 11$ Vishay uniaxial strain gauges, where sensor locations and orientations were maintained constant across all the experiments. Furthermore, the structure was excited by means of a Ling shaker with a maximum excitation frequency of up to 3000 Hz for the brass and steel plates, and 4900 Hz for the copper structure. The sampling

frequency was set to 9766 samples/sec, and various types of windows were employed for the excitation signal. Data acquisition was performed using the CADDMAS system [99], whereas the sensors were modeled using the software GAGEMAP II [27]. The freeware EDAS-DV [27] was instead used to analyze the experimental results acquired and processed by the CADDMAS software. The data blocks from the various acquisitions are used to construct the envelope spectra of the strains measured at every sensor, where each envelope is an amplitude plot displaying the maximum peak-to-peak value at each frequency, obtained via sweeping across all the data blocks. Moreover, Q-curve fitting is employed to fit the recorded points against a second-order curve so as to reconstruct the missing information. Listed in Tables 4 and 5 are the material properties and the sensors' position and orientation, while Figure 23 depicts a model of the structure together with the sensor locations. Moreover, the test equipment and setup are shown in Figure 24 (courtesy of [99]).

Table 4: Material properties and geometry.

	Brass	Copper	Steel
Young's modulus E_o [psi]	15×10^6	17×10^6	29×10^6
Density ρ_o [lb/in^3]	0.3077	0.3227	0.2837
Poisson ratio ν_o	0.34	0.343	0.32
Length L_o [in]	9	9	9
Width W_o [in]	4	4	4
Thickness T_o [in]	0.125	0.125	0.125

The test data were utilized to investigate the impact of various uncertainty sources (both experiment-based and model-driven ones) upon the confidence level associated with the estimated vibratory response, as well as their interaction with one another.
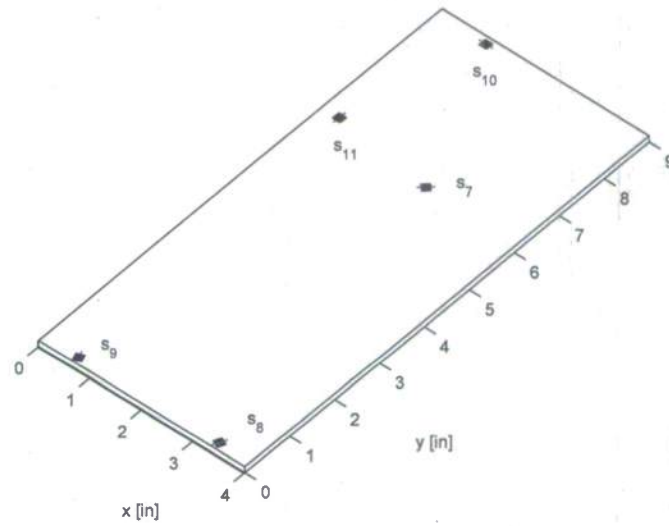
(a) Top surface
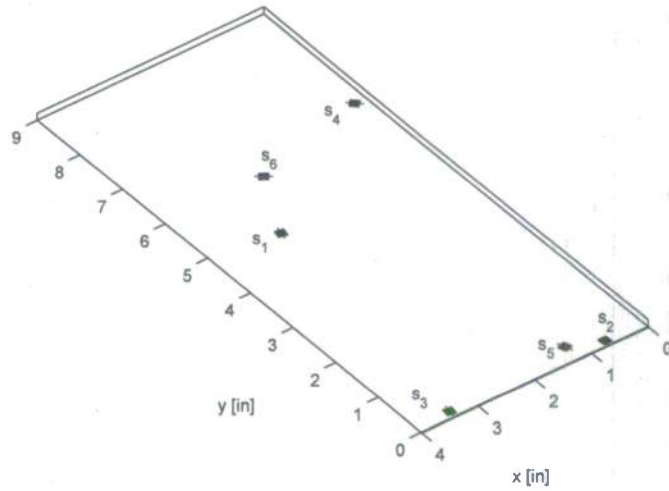
(b) Bottom surface

Figure 23: Model of the plate structure and sensor locations.

Table 5: Experiment setup.

Gauge No.	Position			Measurement Direction $\vec{u}$		
	x [in]	y [in]	z [in]	u_x	u_y	u_z
1	3.2307	4.8375	0.0	0.2071	-0.9783	0.0000
2	0.7693	0.1125	0.0	-0.0360	-0.9994	0.0000
3	3.8814	0.1334	0.0	0.1360	-0.9907	0.0000
4	0.2339	6.6028	0.0	-0.7161	-0.6980	0.0000
5	1.3846	0.3375	0.0	-0.3249	-0.9457	0.0000
6	2.5535	6.0379	0.0	0.8061	0.5918	-0.0000
7	2.5533	6.0676	0.125	0.7047	0.7095	-0.0000
8	3.8818	0.1291	0.125	-0.4205	-0.9073	0.0000
9	0.7725	0.1188	0.125	0.3503	-0.9366	-0.0000
10	1.1013	8.8642	0.125	1.0000	-0.0000	-0.0000
11	0.3866	6.3202	0.125	0.0361	0.9993	0.0000

Figure 24: Test equipment.

3.3   Estimation Results

In order to infer the critical vibratory response for the given plate structures, the response estimation procedure described in Section 2.2 was employed. The experiments were conducted without the use of strain rosettes, hence only one strain component was measured at each gauge location. Therefore, equivalent strain values were computed using equation (7) and converted into equivalent stresses upon multiplication by Young's modulus E_o in accordance with the procedure implemented in [2], with the understanding that the resulting estimated stresses are representative of an equivalent uniaxial strain-stress state. At every peak frequency, various predictions of the maximum Von Mises stress can then be computed by means of a maximization process, performed separately on the information from each sensor.

Results are herein illustrated in detail for the experimental data relative to the brass plate, whereas only a summary of the estimation results is provided for the copper and steel plates. Furthermore, the symbol for the estimated maximum Von Mises stress has been abbreviated to $\sigma^*_{VM_M}$, where references to sensor and peak numbers have been dropped for the sake of clarity.

3.3.1   Mode Identification Results

The inference technique consists of two steps: identification of the peak responses and corresponding best-fitting mode shapes, and estimation of the system's most critical response via combination and extrapolation from the model information and the available test data. For a given experiment, in order to identify the response peaks, the frequency spectra recorded by the sensors were combined into an averaged spectrum whose significant peaks were isolated by filtering out any sensor-averaged strain amplitude smaller than 1/4 of the maximum averaged one. The process is illustrated for a single experiment conducted on the brass plate data in Figure 25, where the recorded spectra $\varepsilon(\omega, \mathbf{x}_g)$ $(g = 1, \ldots, N_g)$ and the sensor-averaged spectrum $\varepsilon_{avg}(\omega)$ are depicted together with the selected strain peak magnitudes. Since the threshold depends on the maximum averaged amplitude, it is worth noting that the number of peaks being detected and retained could vary from

experiment to experiment if sensor measurements were to exhibit a meaningful variability across them. Furthermore, the recorded peak frequencies ω_p may also show a scatter across sensors as well as across repeated experiments. As a consequence of that, for each test, sensor-averaged peak amplitudes, identified by means of the averaged spectrum, are used to isolate the corresponding peak conditions on each of the measured spectra. Figure 26 depicts the scatter in the recorded peak frequencies ω_{p_g} $(g = 1, \ldots, N_g)$ corresponding to the averaged peaks of Figure 25, where each set of peak frequencies is plotted against the natural frequency ω_n of the corresponding mode shape, identified by means of equation (5) and illustrated in Figure 27. As it can be easily observed, the sensors consistently identify the various resonance conditions, which, however, are different from the natural frequencies computed by the system's finite-element model. A numerical quantification of the observed trend is given in Table 6, where mean μ and standard deviation σ are calculated sensor-wise for each detected resonance condition p. The low scatter σ in the measured peak frequencies indicates a proper installation and functioning of the various gauges, but provides no information in terms of quality and accuracy associated with the corresponding strain peak amplitudes.

Table 6: Natural and sensor-averaged measured peak frequencies.

Peak No.	$\mu(\omega_{p_g})$ [Hz]*	$\sigma(\omega_{p_g})$ [Hz]	ω_n [Hz]	
p=1	30.87	1.48	35.31	(1st mode)
p=2	181.20	0	164.10	(2nd mode)
p=3	524.54	0	617.00	(5th mode)
p=4	1030.01	0	999.87	(7th mode)
p=5	1138.64	2.96	1161.70	(8th mode)

*$g = 1, \ldots, 11$

3.3.2 Analysis of Estimation Correlation Results

The availability of various sensors on the component under investigation allows for estimating the accuracy of the estimation procedure described in Section 2.2, and assessing the effects of simplifying assumptions (e.g., the single-mode contribution at resonance) as
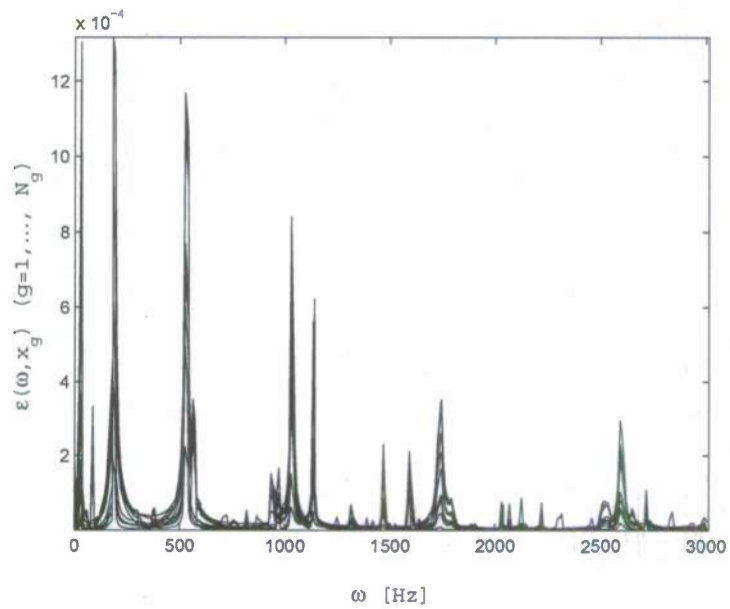
(a) Sensors' frequency spectra
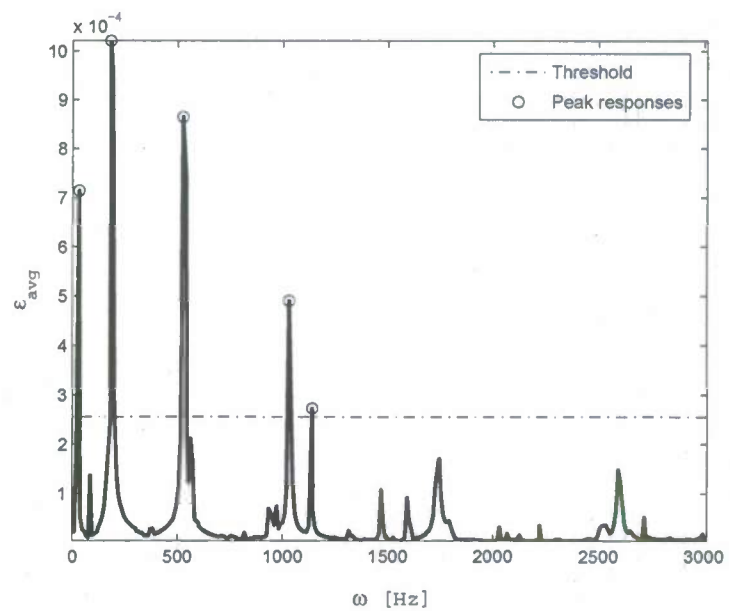
(b) Sensor-averaged frequency spectrum

Figure 25: Peak identification procedure.
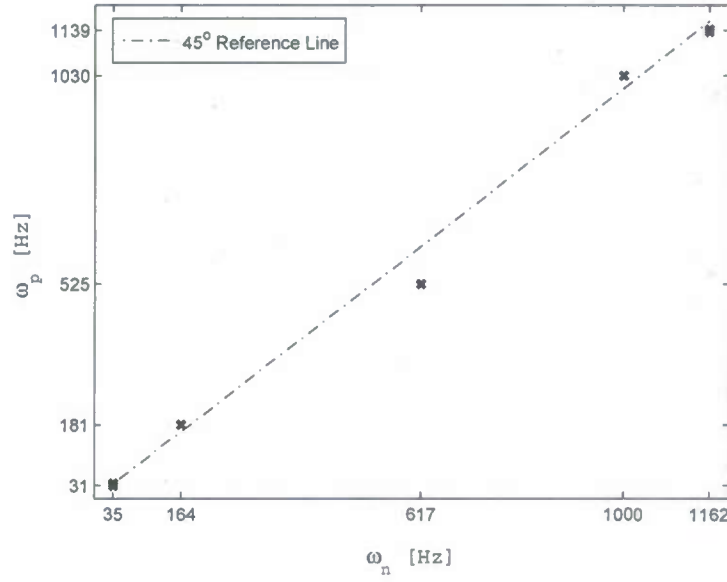
Figure 26: Measured peak frequencies vs. natural frequencies.

well as various other sources of errors and uncertainty. These include, among others, measurement noise, location of the sensors, inaccuracies of the model, and differences between a measured quantity (e.g., strain averaged over the sensor area) and its effective local value.

The quality of the estimates can be quantified through a direct comparison between the measured quantity at the i-th sensor's location $\mathbf{x}_i$, and its estimate based on the measurement at location $\mathbf{x}_j$ of the j-th gauge, which according to equation (6) is given by:

$$\varepsilon_{i,j}^{p*} = \frac{e_p(\mathbf{x}_i)}{e_p(\mathbf{x}_j)} \ \varepsilon_j^p \tag{27}$$

where the notation introduced in Section 2.2.2 is abbreviated as follows:

$$\varepsilon_{i,j}^{p*} = \varepsilon_j^*(\omega_p, \mathbf{x}_i) \tag{28}$$

$$\varepsilon_j^p = \varepsilon(\omega_p, \mathbf{x}_j)$$

Consequently, an estimation coefficient ξ_{ij} can be defined as:

$$\xi_{ij} = \frac{\varepsilon_{i,j}^{p*}}{\varepsilon_i^p} \tag{29}$$

where $i, j = 1, \ldots, N_g$. This coefficient should be equal to one in the case of perfect correlation between estimated and measured values, whereas the larger the deviation from

56
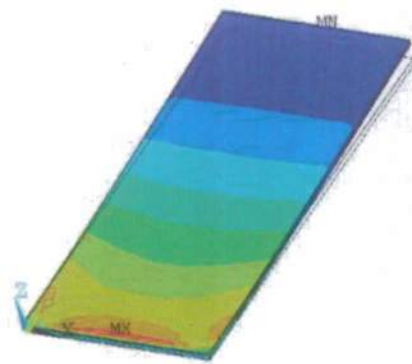
(a) 1st mode
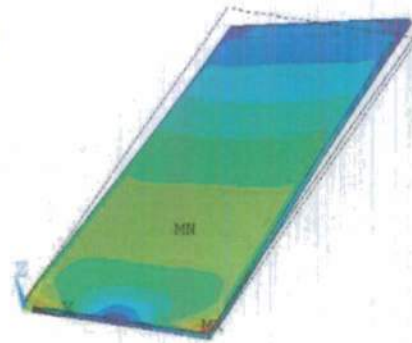
(b) 2nd mode
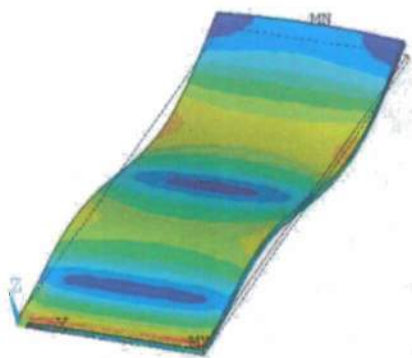
(c) 5th mode
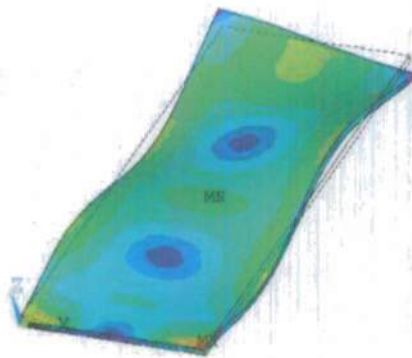
(d) 7th mode
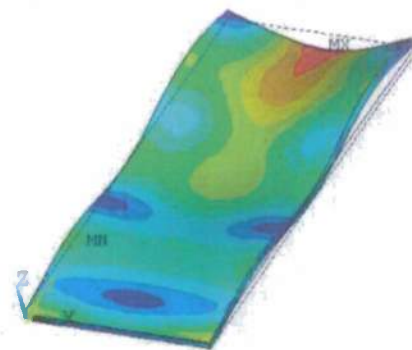
(e) 8th mode

Figure 27: Plate structure: mode shapes and Von Mises modal strain fields.

that value is, the higher the error introduced by the estimation process becomes. Coefficients obtained for varying $i, j = 1, \ldots, N_g$ populate a square matrix Ξ of size $N_g \times N_g$, which contains all possible combinations and whose components are related by the following relationship:

$$\xi_{ij} = \frac{1}{\xi_{ji}} \tag{30}$$

The correlation matrix Ξ can be used to determine the presence of malfunctioning gauges, measurement outliers or sources of strong mismatch, due, for instance, to a sensor mounted near a modal node or a region with strong gradients for the measured quantity.

Once the peak responses are isolated, the correlation matrix Ξ can be constructed for each of them to evaluate how well the test results agree with the numerical analysis at that resonance condition. As an example, shown in Figures 28 and 29 are the results for two different peak frequencies, whose corresponding data of measured amplitudes are analyzed in two different ways. In one case, a detailed investigation is carried out for each pair of sensors by means of the matrix $|\log_e(\Xi)|$, where the operator $|\log_e(.)|$ has been utilized to convert Ξ into a symmetric matrix and take into account the relationship between ξ_{ij} and ξ_{ji} given in equation (30). Of course, as a result of the transformation, $\log_e(\xi_{ij})$ and $\log_e(\xi_{ji})$ $(i, j = 1, \ldots, N_g)$ are equally distant from the perfect-match condition (i.e., a $N_g \times N_g$ zero matrix), while that is not the case for ξ_{ij} and ξ_{ji}. In the other case, a histogram is used to represent the overall agreement between test and model, where a log-normal distribution function has been employed to characterize the data.

As it can be observed from the charts of Figures 28 and 29, the level of agreement between measured and estimated quantities may change significantly from peak to peak. More in detail, the estimate-to-measurement ratios range from 0.5 to 3 for the first peak, whereas the level of mismatch is overall higher for the fourth peak, especially for the fourth, fifth and seventh strain gauges. For a given sensor, this varying performance can be mostly associated with the fact that the sensor itself responds differently to different mode shapes. In fact, the sensor may be in a nodal area (where the level of noise may become comparable to the measured signal) or in a region of high strain gradient (where the measurement is affected by a higher error due to the averaging process over the contact surface of the strain

(a) $|\log_e(\Xi)|$
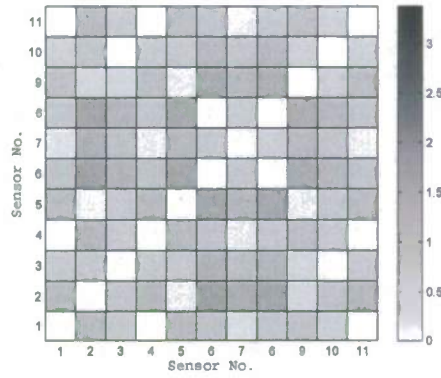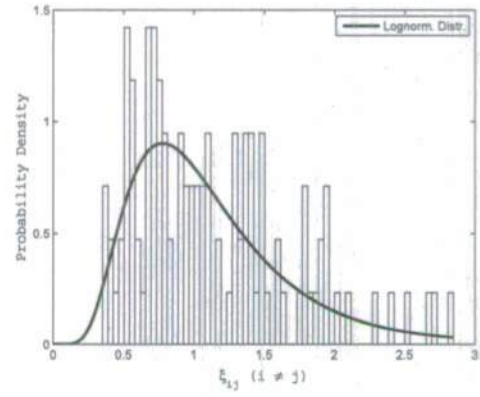
(b) Probability density

Figure 28: $|\log_e(\Xi)|$ matrix (a) and probability density (b) for the first peak frequency.

(a) $|\log_e(\Xi)|$
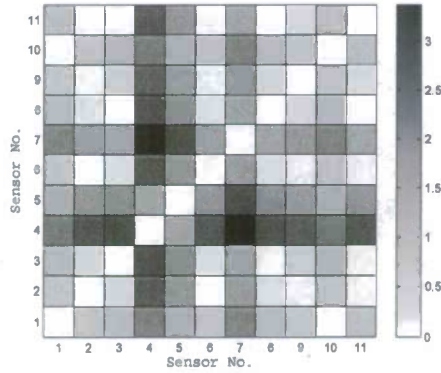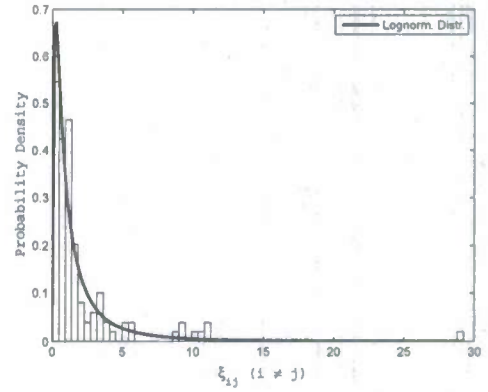
(b) Probability density

Figure 29: $|\log_e(\Xi)|$ matrix (a) and probability density (b) for the fourth peak frequency.

gauge). Of course, other more subtle issues may also add to the change in performance (e.g., dependence upon mutating environmental conditions at different load conditions, or varying model accuracy in the computation of different mode shapes).

Another source of uncertainty and, hence, of reduced accuracy is given by the discrepancy in the measurements obtained from different, yet consistent, experiments. In the presence of a significant variability in a sensor's measurements across several experimental tests, it is safe to argue that the given sensor may be malfunctioning or incapable of fully capturing the physical behavior of the structure under the given load and environmental conditions. As a consequence, these measurements may need to be filtered out or weighed differently to account for the anomaly. As an example, illustrated in Figure 30 is the scatter in the strain amplitudes at the first and fourth peak of Table 6, measured by the same sensors in a series of distinct experiments. Moreover, Figure 31 shows a similar measurement variability for various resonance conditions, recorded in the same set of tests by the fifth and the eighth sensor. Despite the good agreement, across distinct experiments, among the recorded values for any given peak frequency, the measurements for the corresponding peak amplitude may still be affected by some significant variability. In fact, the measured data is not identical from test to test, and any existing difference may be further amplified by errors and approximations introduced through data-processing (e.g., the error due to the interpolation needed to reconstruct the spectrum from sampled noise-carrying information). More in detail, according to Figure 30, near the first resonance frequency, the eighth sensor exhibits a much larger spread in the measurements compared to the other gauges. Such a singular behavior highlights the possibility that the given sensor's readings could be erroneous in some tests, and that they could be treated as potential outliers. The placement of such gauge in a region of high strain gradients may strongly impact the quality of its measurements, but may not be identified as a key source of error because of the comparatively lower variability exhibited by similarly placed sensors. In the case of the fourth peak, instead, significant scatter can be observed for all sensors. In this circumstance, sensor 8 is again characterized by the largest measurement variability, but this behavior may not be univocally explained with measurement issues strictly related to that single gauge.

(a) 1st peak   (b) 4th peak
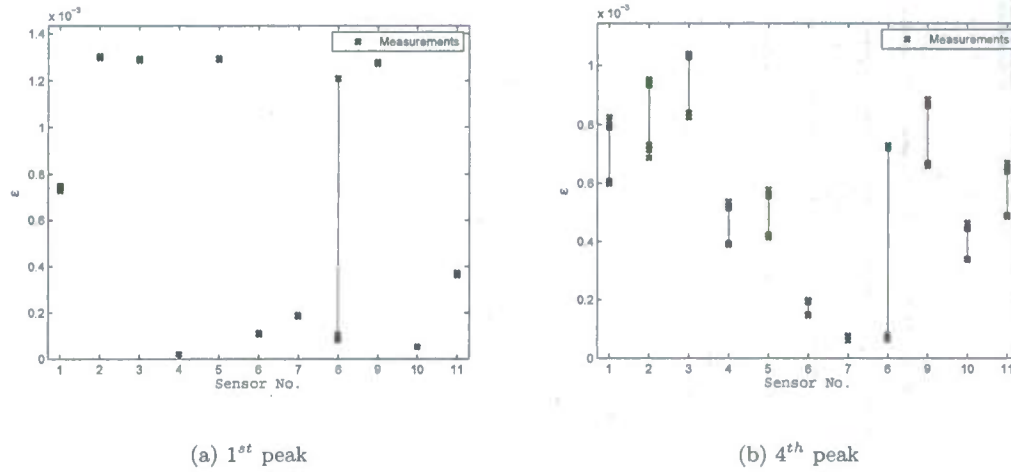
Figure 30: Variability in the strain amplitudes at the first (a) and fourth (b) peak, measured by each sensor in seven distinct experiments.

Moreover, from a qualitative standpoint, the relative orders of magnitude among the measurements appear to be in agreement with the strain field for the seventh mode of Figure 27.

Illustrated in Figure 31 is the measurement scatter exhibited by sensors 5 and 8 at various peak frequencies. As pointed out by Figure 29, both sensors are characterized by some disagreement between estimated and recorded quantities, where that result was, of course, relative to a single test. The consistency in measurement across various experiments that is shown in Figure 31 seems to suggest that the aforementioned mismatch at sensor 5 could be due to an actual discrepancy with the model results, as this sensor behaves similarly to other gauges. As for the eighth strain gauge, its prominently changing behavior across experiments and excitation frequencies hints, instead, to the presence of a potential problem with the readings *per se*. As a matter of fact, this sensor is located near the plate's clamped edge where high strain gradients can be experienced for some of the resonance conditions, as indicated by Figure 27. As a consequence, its recordings may suffer further from the error introduced by measurement averaging over its contact surface.

As it can be observed, the combination of all these pieces of information can prove to be a valuable tool to identify sources of uncertainty and errors, as well as pinpoint outliers,
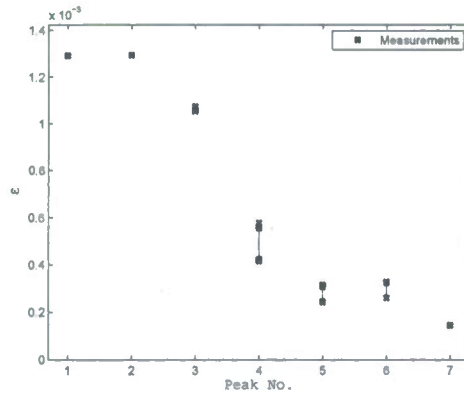
(a) 5th strain gauge
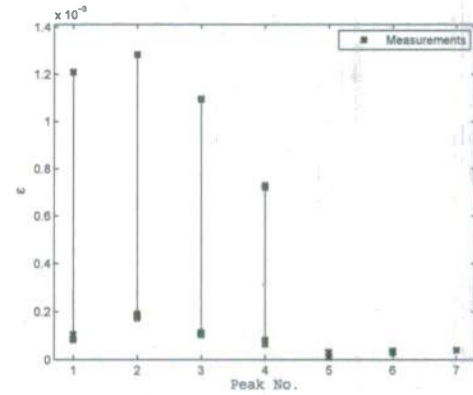
(b) 8th strain gauge

Figure 31: Variability in the strain amplitudes at various resonance conditions, measured by the fifth (a) and eighth (b) gauge in seven distinct experiments.

whose isolation is deemed to be necessary to increase the level of confidence associated with the estimated response.

3.3.3 Analysis of Maximum-response Estimates

Up to this point, the goodness of the experimental results has been investigated together with their agreement with the model at the sensor locations themselves. The next step is to infer the system's response at other locations as well. As a result, the level of accuracy associated with these new estimates cannot be assessed, as previously done, by direct comparison, thus implying an inherently lower level of confidence in their values. In order to compensate for this aspect, a benchmark response value was computed for each experiment as a weighted average of an appropriately selected subset of estimates. More specifically, the response predictions associated with sensors i and j were assumed to be acceptable provided that:

$$\log_e(0.8) \leq \log_e \xi_{ij} \leq \log_e(1.2) \tag{31}$$

where a 20% level of mismatch between experiment and model was deemed to be within the norm. Furthermore, the predicted quantities were divided into groups, and weights for each of them were computed based on the size of their corresponding group. More in detail,

62
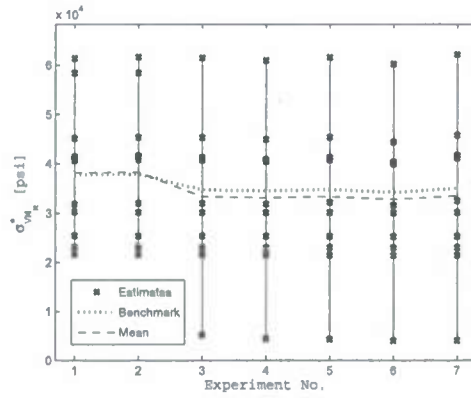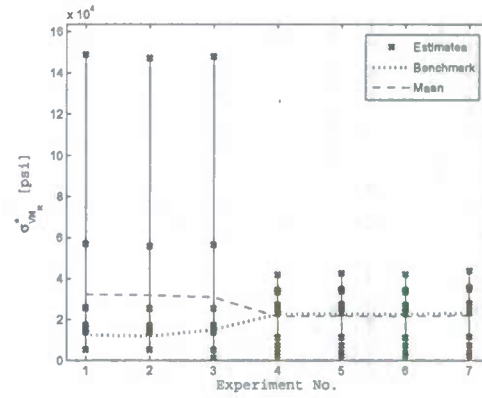
(a) 1st peak (30.87 Hz)   (b) 4th peak (1030.01 Hz)

Figure 32: Estimation of the maximum Von Mises stress $\sigma^*_{VM_M}$ at the first (a) and fourth (b) peak, computed using sensor measurements from seven experiments.

for each sensor i a set of predictions was constructed encompassing the estimate from the j-th gauge only if the constraint equation (31) were satisfied. Therefore, the estimates belonging to a larger group were weighted more in light of the fact that more sensors were in agreement with one another. The result of this procedure is illustrated in Figure 32, where predictions for the maximum Von Mises stress are compared with the computed benchmark values (dotted line). More specifically, for a given peak condition, the eleven strain measurements from each experiment were combined using the procedure of Section 2.2.2 with appropriate modal ratios to estimate the maximum response. For the first peak, it can be observed that the dashed mean-value line, computed using all the estimates, agrees fairly well with the benchmark line; in fact, in agreement with the results of Figure 30, only sensor 8 was excluded based on equation (31), while the use of a weighted average did not seem to have a strong impact. Overall, all the experiments agree well with one another exhibiting consistent variability in the stress predictions. Results, instead, show more scatter in the estimated response near the fourth peak frequency. The first three experiments are characterized by a spread which is more than double compared to the others. Furthermore, the estimates' mean and the benchmark value differ by the same order of magnitude suggesting the fact that some sensor measurements may be erroneous or in strong disagreement with

the model. As a consequence of these observations, the level of accuracy associated with such estimates becomes diminished. It is important to note, however, that the experiments were not conducted identically to one another, and that the change in spread could also be caused, to some extent, by differences in the measurement setup (e.g., tuning of the data-acquisition parameters).

The results depicted in Figure 33 are exactly the same as those shown in Figure 32, except that they are grouped by sensors instead of by experiments. The observed trends clearly indicate a problem with sensors 4 and 8; the former is located near a nodal region for the 7th mode, while the latter is in a high-gradient zone for the 1st mode, hence potential inaccuracies in the finite-element solution at those locations may cause an amplification of any existing measurement variability. Findings also show that the response estimate may vary significantly when computed using different gauges. Besides the underlying measurement variability shown in Figures 30, the scatter is also caused by the extrapolation process involving locations on the structure for which the level of agreement between model and experiments is not known *a priori* and cannot be quantified better unless more gauges are placed on the component. In light of this, and in the presence of significant variability across sensors, it may become difficult to quantify the confidence level associated with any given estimate.

Finally, the same analysis, described for the brass plate, was also conducted on a steel and a copper plate, whose results from the estimation procedure are summarized in Figures 34 and 35 and highlight similar trends.
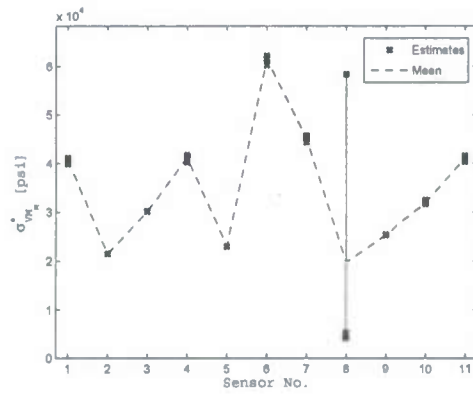
(a) 1st peak (30.87 Hz)
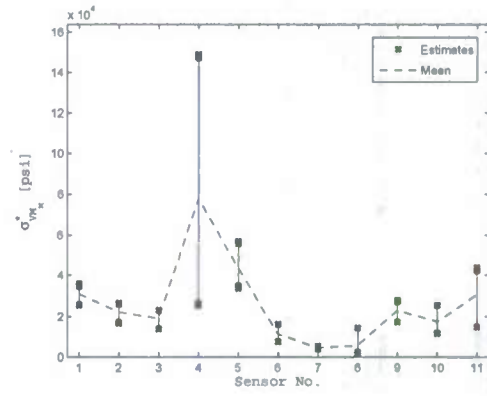
(b) 4th peak (1030.01 Hz)

Figure 33: Estimation of the maximum Von Mises stress $\sigma^*_{VM_M}$ at the first (a) and fourth (b) peak, computed using sensor measurements from seven experiments.
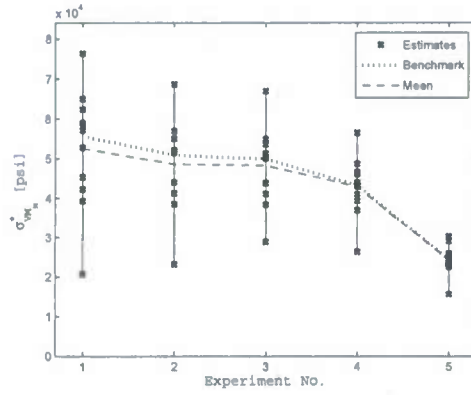
(a) 1st peak (48.80 Hz)
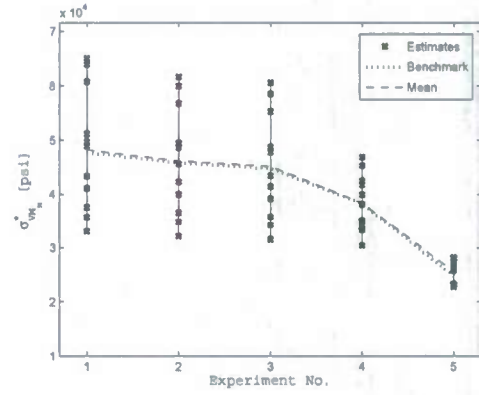
(b) 2nd peak (314.72 Hz)
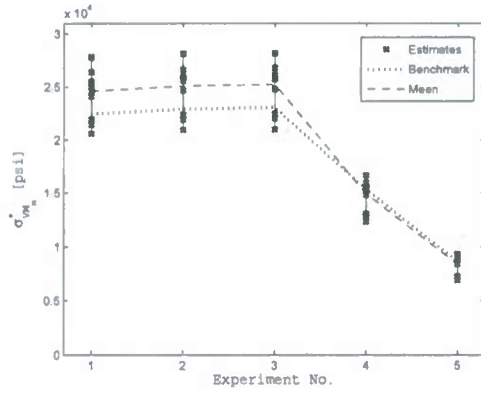
(c) 3rd peak (886.95 Hz)
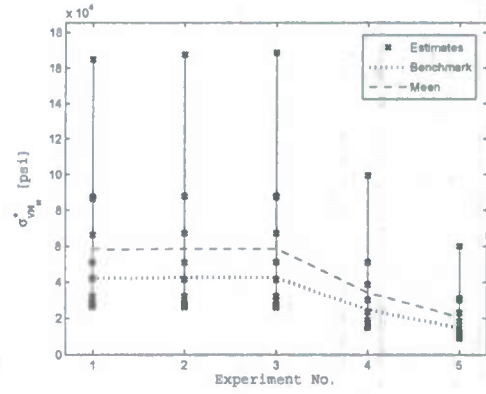
(d) 4th peak (1697.60 Hz)

Figure 34: Estimation of the maximum Von Mises stress $\sigma^*_{VM_M}$ for a steel plate, computed using measurement data from five experiments.
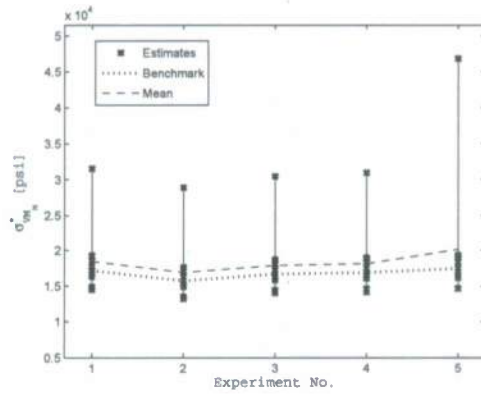
(a) 1st peak (36.72 Hz)
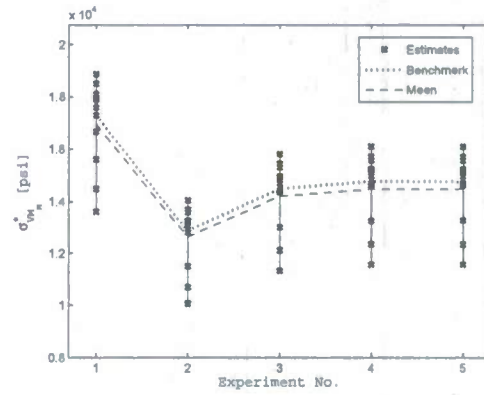
(b) 2nd peak (219.35 Hz)
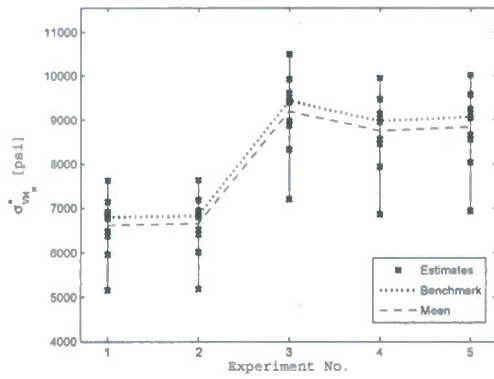
(c) 3rd peak (629.45 Hz)
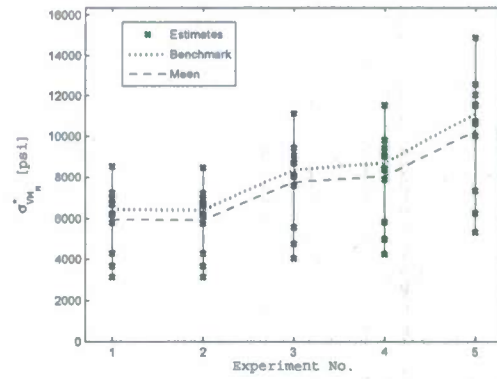
(d) 4th peak (1211.21 Hz)

Figure 35: Estimation of the maximum Von Mises stress $\sigma^*_{VM_M}$ for a copper plate, computed using measurement data from five experiments.

67

3.4 Data Processing

The experimental data utilized in the previous sections for correlation analysis and response estimation were obtained via the data-processing procedure briefly outlined in Section 3.2. More in detail, each sensor's peak-hold spectrum was obtained by considering the envelope of a series of Fourier transforms performed upon a sequence of sample blocks comprising the response in time of the plate structures. Furthermore, the block size was chosen to be 8192 samples per block, while the Blackman-Harris window was selected for the windowing process of the output signal. Obviously, these choices are not unique, but are often based on the experimenter's judgement and expertise.

Presented next is a discussion on spectrum variability associated with such choices, specifically the one due to two data-processing parameters: window type and block size.

3.4.1 Windowing

Windowing is one of the techniques used to alleviate the problem of leakage affecting the quality of the frequency spectrum of a signal truncated in time. It consists of combining a specified known signal $w(t)$ with the signal $m(t)$ recorded by the data-acquisition device [26]:

$$\widetilde{m}(t_n) = w(t)_{|t=t_n} \cdot m(t_n) \tag{32}$$

in which $\widetilde{m}(t)$ is the windowed signal and $m(t)$ is the measured quantity, both known only at the sample time instants $t_n = n\Delta t$, where Δt is the time interval between two consecutive measurement acquisitions. Given the Fourier transforms $M(\omega)$ and $W(\omega)$ of $m(t)$ and $w(t)$, respectively, the spectrum $\widetilde{M}(\omega)$ of the windowed signal is equal to

$$\widetilde{M}(\omega) = M(\omega) \odot W(\omega) \tag{33}$$

where the symbol $\odot$ indicates the convolution-integral operator. In order to reconstruct the response's actual magnitude, $\widetilde{M}(\omega)$ must be multiplied by a window-specific gain G_w so as to compensate for the effect of signal attenuation due to windowing [38].

The impact of window selection in the processing of a system response's measured amplitudes is here investigated by considering six types of windows, which are depicted in

68

Table 7: Windows.

Name	Definition
Rectangular	$w(n) = 1 \,,\ 0 \leq n \leq N-1$
Hann	$w(n) = 0.5 \left[1 - \cos\left(\frac{2\pi n}{N-1}\right)\right] \,,\ 0 \leq n \leq N-1$
Blackman	$w(n) = \quad 0.42 - 0.5\cos\left(\frac{2\pi n}{N-1}\right) + 0.08\cos\left(\frac{4\pi n}{N-1}\right)$ $0 \leq n \leq N-1$
Blackman-Harris	$w(n) = \quad a_0 + a_1\cos(\frac{2\pi n}{N-1}) + a_2\cos(\frac{4\pi n}{N-1}) + a_3\cos(\frac{6\pi n}{N-1})$ $-(N-1)/2 \leq n \leq (N-1)/2$ $(a_0 = 0.35875,\ a_1 = 0.48829,\ a_2 = 0.14128,\ a_3 = 0.01168)$
Bohman	$w(n) = \quad \left(1 - \frac{2\lvert n\rvert}{N-1}\right)\cos\left(\frac{2\pi\lvert n\rvert}{N-1}\right) + \frac{1}{\pi}\sin\left(\frac{2\pi\lvert n\rvert}{N-1}\right)$ $0 \leq \lvert n \rvert \leq (N-1)/2$
Tukey	$w(n) = \begin{cases} 1 & 0 \leq \lvert n\rvert \leq \alpha\frac{N-1}{2} \\ \frac{1}{2} + \frac{1}{2}\cos\left(\pi\frac{n - \frac{\alpha}{2}(N-1)}{(1-\alpha)(N-1)}\right) & \alpha\frac{N-1}{2} \leq \lvert n\rvert \leq \frac{N-1}{2} \end{cases}$ $(\alpha = 0.5)$

Figure 36 and whose discretized definitions in terms of time index n and sample size N are given in Table 7 [97]. Illustrated in Table 8 and Figures 37-38 is the effect of windowing upon the brass plate's peak strains, obtained at the fifth and eighth sensor locations using different windows types, whereas the results for the other sensors are reported in Table 9. In oder to evaluate the scatter at each gauge g and resonance p of Table 6, the percentage relative errors δ, computed with respect to the mean values, and the coefficients of variation σ/μ of the strain amplitudes were used as figures of merit. Shown in Figures 37(b)-(c) and 38(b)-(c) are the mean and standard-deviation spectra constructed considering all six window-specific spectra, while Figures 37(d) and 38(d) depict the dependence upon window type of the strain peak amplitudes ε_5^p and ε_8^p at the p-th resonance condition identified in Figures 37(a) and 38(a), respectively. The data reported in the tables, instead, were computed without considering the rectangular window to distinguish between windowed and non-windowed signals. The use of a different window, as shown, has no impact on

69
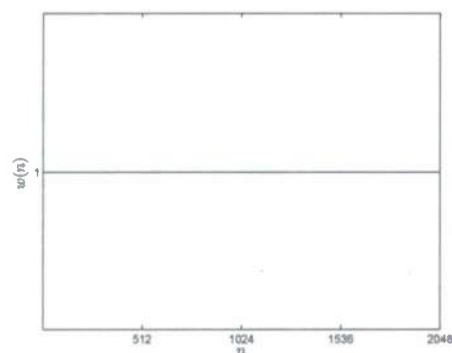
(a) Rectangular window
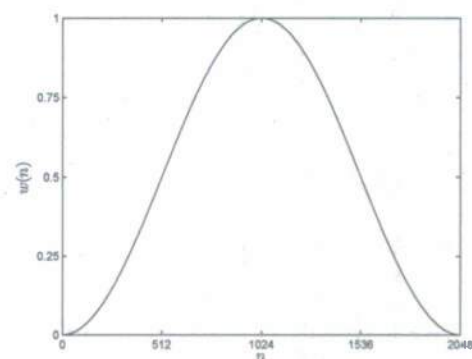
(b) Hann window
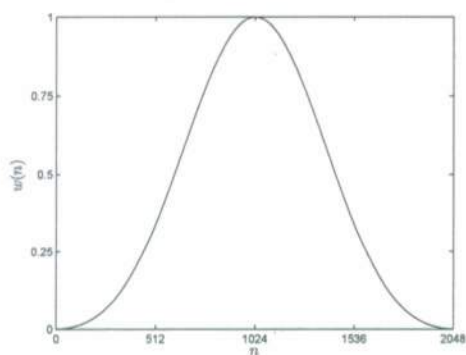
(c) Blackman window
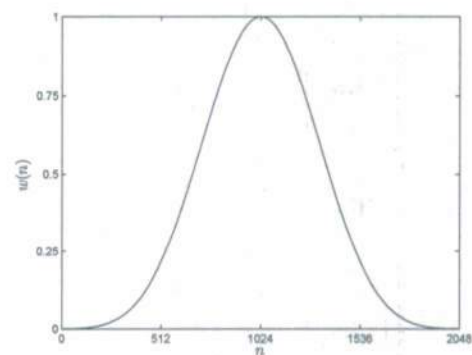
(d) Blackman-Harris window
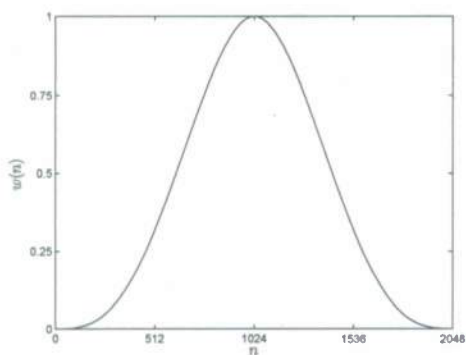
(e) Bohman window
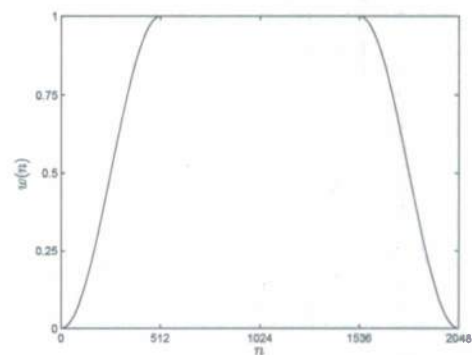
(f) Tukey window

Figure 36: Windows (sample size $N = 2048$).

the peak frequencies, but it introduces additional variability in the strain peak amplitudes, whose accuracy is already affected by measurement errors. As suggested by the tabulated results, the percentage relative error due to windowing can fluctuate significantly with peak values as high as about 26%. Figures 37(d) and 38(d) show how window selection seems to have a stronger impact in the case of lower-amplitude peaks: the higher the measured peak amplitude, the smaller its variability due to the use of a different window. Based on the difference in response amplitudes obtained with the rectangular window (i.e., the no-- window case) and the other ones, Figure 38(d) also highlights how the effect of windowing is somewhat mitigated in the case of the lowest-amplitude fourth peak, if compared with its impact at the other resonance conditions. This absolute low impact, however, can still be responsible of a non-negligible variability when compared with the low signature of the measured signal.

Overall, a particular window may rescale the peak amplitudes in such a way that the error being introduced in the processed data could become comparable with other sources of uncertainty. Of course, the numerical variability that was observed depends on the specific windows being considered, where the use of other window types may generate a different variability level in the peak amplitudes. The importance of the information at hand, however, is that, while windowing addresses the problem of leakage in signal processing, window selection can play an important role in terms of accuracy of the results.

Table 8: Variability in measured strain amplitudes due to windowing: 5th and 8th gauge.

Gauge No.	Peak No.	$\min(|\delta|)$ [%]	$\max(|\delta|)$ [%]	$\frac{\sigma}{\mu}$ [%]
	1	5.89	10.42	6.38
5	2	1.88	3.45	2.11
	3	14.15	23.96	14.81
	1	6.51	11.38	6.99
8	2	1.91	3.50	2.14
	3	13.60	22.99	14.22
	4	10.83	11.15	8.16

Results based on a single experiment. Case of rectangular window excluded.

Table 9: Variability in measured strain peak amplitudes due to windowing.

Gauge No.	Peak No.	$\min(|\delta|)$ [%]	$\max(|\delta|)$ [%]	$\frac{\sigma}{\mu}$ [%]
1	1	5.46	9.59	5.88
	2	1.86	3.41	2.09
	3	15.19	25.31	15.70
	4	10.26	10.59	7.75
2	1	5.81	10.28	6.30
	2	1.70	3.12	1.91
	3	12.38	21.16	13.05
	4	13.01	14.31	10.29
3	1	5.86	10.36	6.35
	2	1.67	3.07	1.88
	3	12.70	21.41	13.25
	4	13.41	14.94	10.68
4	2	2.93	5.38	3.28
	3	15.37	25.68	15.92
	4	10.55	10.97	7.98
6	2	2.95	5.41	3.30
	3	15.50	25.90	16.06
	5	3.21	6.37	3.82
7	1	5.45	9.56	5.87
	2	3.00	5.47	3.35
	3	15.45	25.78	15.99
	5	3.22	6.39	3.83
9	1	6.01	10.63	6.51
	2	1.79	3.28	2.00
	3	13.25	22.49	13.89
	4	9.94	10.37	7.55
10	2	2.90	5.27	3.22
	3	15.27	25.32	15.73
	4	10.78	11.10	8.13
	5	3.13	6.22	3.73
11	1	5.45	9.56	5.87
	2	2.30	4.20	2.57
	3	12.80	21.69	13.41
	4	11.00	11.18	8.22

Results based on a single experiment. Case of rectangular window excluded.
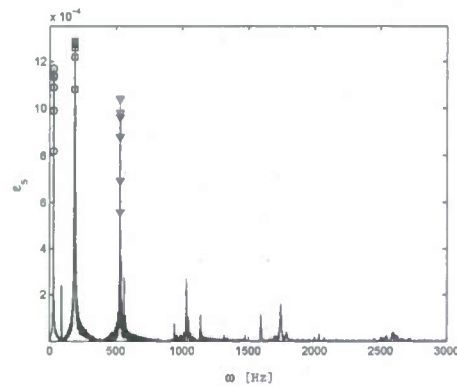
(a) Window-dependent spectra
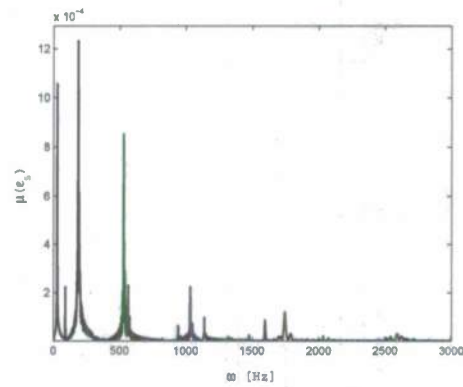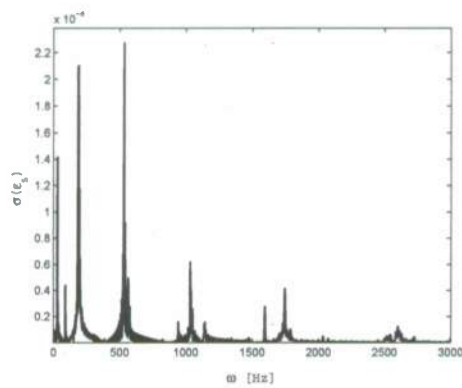
(b) Mean spectrum

(c) Standard-deviation spectrum
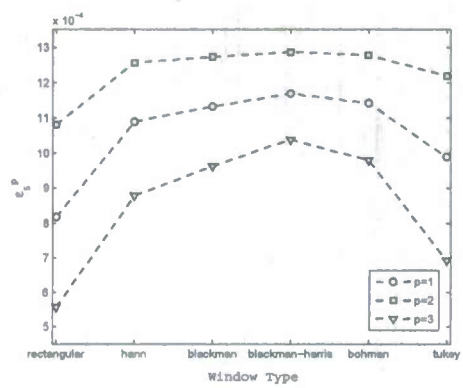
(d) Strain amplitude at the p-th resonance

Figure 37: Variability due to window selection: spectral information from measurements at the 5th strain gauge.
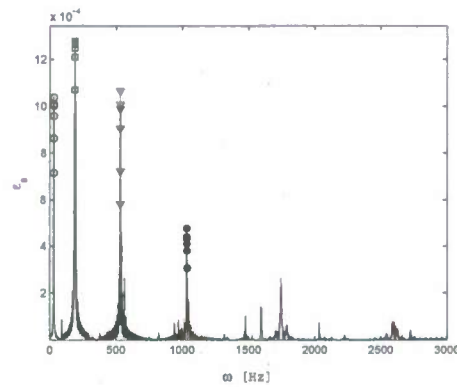
(a) Window-dependent spectra
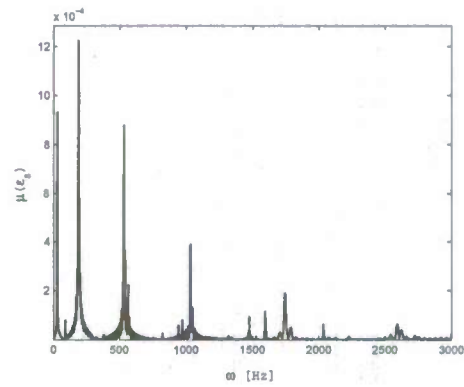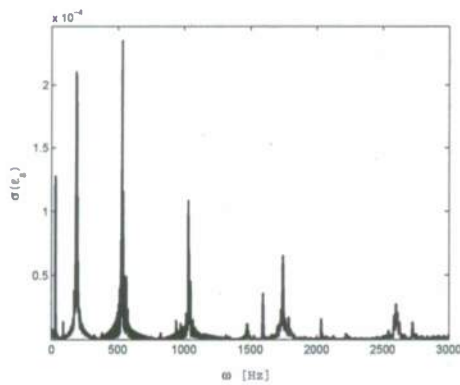
(b) Mean spectrum

(c) Standard-deviation spectrum
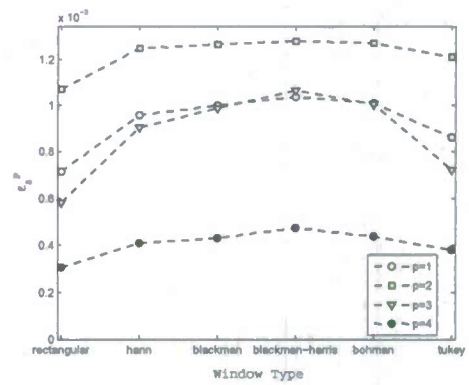
(d) Strain amplitude at the p-th resonance

Figure 38: Variability due to window selection: spectral information from measurements at the 8th strain gauge.

3.4.2 Block Sizing

The frequency resolution of a spectrum is a function of block size, where the larger the size of the blocks is, the higher the resolution of the block spectra becomes, thus leading ideally to a more accurate computation of the resonance peaks. In order to quantify the effect of block-size selection, six different values were considered, namely 512, 1024, 4096, 8192 and 16384 samples per block. Larger block sizes were not considered so as to avoid the issue of flattening of a spectrum's magnitude induced by the necessary normalization of the Fourier transform with respect to the number of samples utilized for its computation.

The effect of changes in this parameter is illustrated in Figure 39 for the strains recorded by the 5th and the 8th sensor and corresponding to the same peak conditions identified in Figures 37(a) and 38(a). Beyond a certain block size, it can be observed that the gain in frequency resolution is outweighed by a loss of information in terms of computed peak amplitudes. This phenomenon can be ascribed to the fact that blocks of different size have distinct frequency contents. Therefore, in contrast to the case of a frequency content equally present throughout the entire time signal, such lack of frequency-wise equivalency among the various blocks may cause the Fourier transform to distort the measured information and further misestimate the peak conditions. Moreover, the figure also indicates that this effect is not uniform across the various sensors and resonances; hence, it cannot be easily predicted. Listed in Table 10 are the percentage relative errors and the coefficients of variation associated with the peaks recorded at all strain gauges, where results were computed without the case of 16384 samples/block as it was found to be responsible for large excursions in the error. Under this assumption, the selection of the block size may imply a maximum relative error of the order of 20% in most cases. Although other worse scenarios were observed, these were not included in the current analysis either because of the poor signal-to-noise ratios for certain combinations of peak and gauge, or because the variability was such that an experienced experimenter would adjust the data-processing parameters so as to avoid those occurrences.

(a) 5th gauge
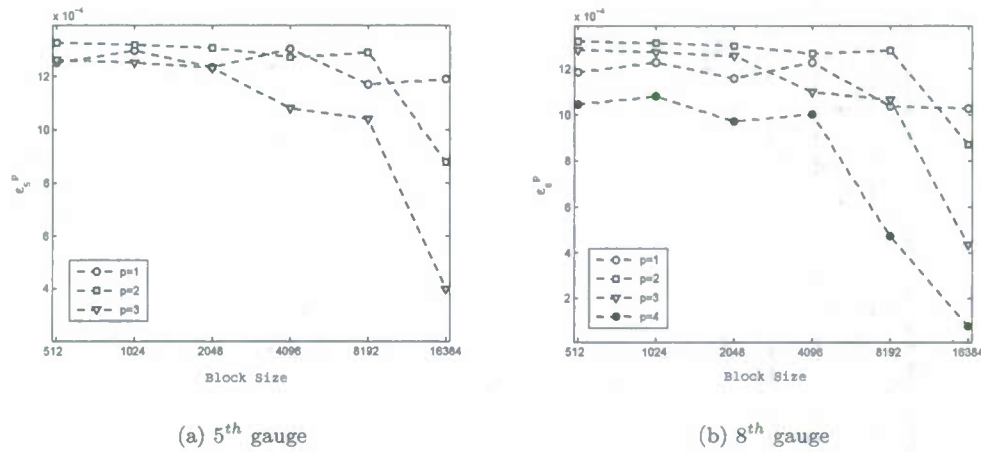
(b) 8th gauge

Figure 39: Variability in measured strain amplitude for the p-th resonance due to block sizing: 5th and 8th gauge.

3.5 Summary

The experimental assessment of uncertainty propagation has shown how measurement errors, data-processing and model approximations can all result in a significant variability for the estimated response. In some cases, the spread in measurement (and hence in the estimates) across experiments for a given sensor could suggest a possible problem associated with that particular gauge or acquisition channel, whereas other scenarios may be more difficult to explain. In fact, despite consistent recordings throughout several experiments for a group of sensors, a scatter in the estimates may still occur, the cause of which may be a disagreement between analytical and test results (due, for instance, to inaccurate modeling or poor selection of the best-fitting mode shape), a non-uniform distribution of the measurement errors among the gauges (e.g., due to suboptimal sensor placement), or some combination of those and other causes. In all these circumstances, the use of cross validation for the inference technique at the sensor locations proves to be a suitable first--order tool to assess the overall goodness of the estimation procedure, as well as to identify and exclude some potential outliers. Benchmark values give also a valuable qualitative insight in terms of estimates' consistency within an experiment or across distinct tests,

as well as permit to assess the combined impact of different sources of uncertainty in the absence of other means of comparison. Moreover, despite the fact that measured peak frequencies are often used alone to match the forced response with a specific mode shape, the good uniformity in their measurements across various sensors and tests did not prove to constitute a comprehensive assessment of the overall goodness of the experimental results. Lastly, data-processing parameters together with the related issues of frequency resolution and leakage may also cause a reduction in the correlation between model and test data, and may lead to additional variability in the inferred response.

The proper source of error or uncertainty may not always be clearly isolated due to strong intertwining among the various contributors. These findings, therefore, need to be integrated with a more thorough statistical characterization of the response prediction process, for which purpose Bayesian networks are investigated in the following chapters.

Table 10: Variability in measured strain peak amplitudes due to block sizing.

Gauge No.	Peak No.	min($|\delta|$) [%]	max($|\delta|$) [%]	$\frac{\sigma}{\mu}$ [%]
	1	8.42	20.73	11.86
1	2	1.78	2.32	1.68
	3	16.03	21.62	16.25
	1	3.79	6.42	4.17
2	2	1.61	2.49	1.61
	3	6.72	13.06	8.07
	1	3.80	6.47	4.19
3	2	1.45	2.31	1.49
	3	5.79	10.69	7.33
4	2	9.29	15.44	9.95
	3	14.28	17.64	14.57
	1	4.17	6.40	4.29
5	2	1.82	2.31	1.70
	3	7.58	11.33	8.91
	1	8.58	20.96	12.00
6	2	9.37	15.43	9.94
	3	14.69	17.82	14.77
	1	8.39	20.85	11.92
7	2	8.49	14.20	9.10
	3	15.10	19.13	15.29
	1	5.20	11.08	6.69
8	2	1.87	2.25	1.72
	3	7.21	10.79	8.63
	4	18.16	48.22	27.33
	1	3.47	7.70	4.91
9	2	1.73	2.38	1.65
	3	5.93	11.04	7.40
	1	8.17	20.23	11.57
10	2	7.61	11.95	7.86
	3	16.07	22.82	16.94
	1	8.49	20.69	11.85
11	2	2.01	2.21	1.95
	3	5.52	10.78	7.10

Results based on a single experiment. The case of 16384 samples/block not included in the calculations.

CHAPTER IV

UNCERTAINTY MODELING VIA BAYESIAN NETWORKS

4.1 Overview

To date, uncertainty has been usually quantified by means of uncertainty propagation techniques (e.g., Monte Carlo simulations), where a statistical realization of a system's input parameters is propagated through a numerical model to construct the statistics of the system's outputs. As shown in the previous chapters, this approach of unidirectional propagation of uncertainties works well for sensitivity studies, but some limitations arise when data are available at the output level (as in the case of experiments) or at some intermediate stage within the analysis. In such cases, the consequent backward propagation of information ought to be taken into consideration and properly modeled when using the given data to fine-tune the analysis. The feasibility of using a Bayesian Network (BN) to model multi-directional uncertainty propagation is herein investigated for the estimation of the modal parameters of a structural system with uncertain parameters. Estimation is performed through the usage of an analytical/numerical model of the system, with the assumption that a limited set of experimental data, available on input or output parameters, can be introduced as evidence to reduce any residual uncertainty. The procedure is first tested on a simple beam structure, and then extended to an evaluation of the modal quantities of a bladed-disk sector.

4.2 Bayesian Networks

A Bayesian network is a directed acyclic graph consisting of nodes representing relevant properties of a given system or process, and directed arcs (links) describing the probabilistic dependence between pairs of nodes [77, 79]. Each node is characterized with a set of exhaustive and mutually exclusive values (either discrete or continuous ones) which represent alternative states of the property corresponding to that node. The direction of each node-to-node connection indicates a parent-child relationship, where no directed cycles are allowed

in the network. Nodes without parents are referred to as root nodes, whose marginal probabilities or density are specified for each of their admissible discrete or continuous value, respectively. Conditional probabilities are specified for non-root nodes for each possible combination of its parent nodes' values, where conditional probability tables and distributions are used for discrete and continuous variables, respectively. Both prior probabilities at the root nodes and conditional probabilities at the child nodes can be obtained by means of statistical learning [73]. A state space of the described nodes (i.e., the full joint probability) is then uniquely defined for all the nodes. The property of a Bayesian network most relevant to the problem at hand consists, however, in its ability to update the marginal probability distributions of all the nodes if new evidence is introduced at some node(s). This process is called abductive inference [80], and its use is suggested to update an initial estimate of uncertainty based on the introduced test results (evidence). For continuous variables, links are commonly assumed to be linear Gaussian, which means that any given child node is assumed to be a random variable X with a normal distribution $N(\mu, \sigma)$, where the mean μ is linearly dependent upon the parent nodes' values, while the standard deviation σ is independent of those parents. In this study, all physical quantities being considered are continuous and the aforementioned assumption has been adopted.

In the presence of observed events, evidence is introduced in the form of assigned single-instance values for the corresponding nodes, which are therefore treated as deterministic quantities. These deterministic values are utilized to update the conditional probabilities associated with the remaining nodes, as well as to compute the posterior full joint probabilities of all the variables. In practice, evidence is also affected by uncertainty (e.g., inaccuracy in test measurements) and should be assessed in a statistical sense as well. Their deterministic treatment is determined by the software package in use and such a limitation could be removed, for example, by adding to the network extra nodes describing the uncertainties inherently present within any evidence. This strategy has not been pursued at this stage so as to isolate other trends of interest and preserve the simple structure of the networks under consideration. Since the causal relationships among the physical parameters of the dynamical structural systems under consideration are already known, the network shall be

trained only to establish the conditional probabilities, while its dependence structure is already defined. The Bayesian statistical analysis has been conducted using the open-source Matlab®-based Bayesian Net Toolbox (BNT) [73], where a parameter training algorithm based on the maximum-likelihood criterion was employed together with training data generated via Monte Carlo simulations performed on given finite-element system models.

4.3 BN-based Uncertainty Analysis on a Beam Structure

The estimation of a beam's natural frequencies and their dependence upon system characteristics is considered here to investigate the effects of uncertainty both in the analytical model and in the model input parameters. A Bayesian network can be utilized to establish a statistical relationship among the data samples of input parameters and modal performance parameters, whose realizations may be obtained, for instance, via direct probabilistic simulation. Furthermore, Bayesian networks also allow for the assessment of multi-directional propagation of uncertainty as well as evidence, available, for instance, through experimental measurements of any subset of system input or output properties. Once its structure is established, the Bayesian network is trained using a given sample data set resulting from a Monte Carlo simulation in which normal distributions are assumed for the network root-node variables corresponding to the system input parameters describing the finite-element model.

First, the effectiveness of uncertainty quantification via Bayesian networks is studied by investigating the effect of input uncertainty propagation on the natural frequencies. The propagation is modeled through two networks, whose structures depend upon the number of uncertain inputs being considered. In the first case, the parent node of a one-root-node network represents the material Young's modulus, while in the second configuration the cross sectional dimensions (thickness and width) are also included as parent nodes of a three-root-node network. Both networks have ten child nodes, each of which represents a natural frequency. Schematic representations of the two networks are shown in Figure 40.

Before proceeding with uncertainty quantification, the fidelity associated with the network's probabilistic inference needs to be assessed with respect to the loss of accuracy due
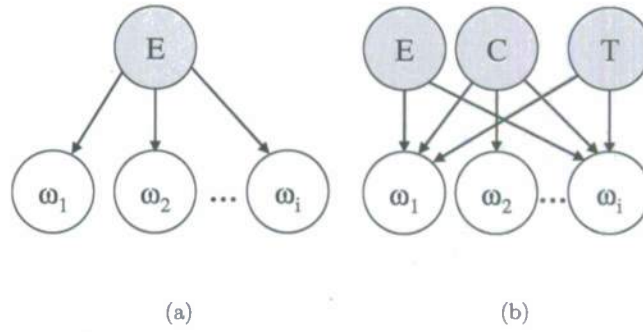
Figure 40: One-root-node (a) and three-root-node (b) network topologies.

to network modeling assumptions and erroneous training data. When connected to one another, two nodes are herein assumed to be linked through a linear Gaussian relationship, where this postulation may lead to non-negligible modeling inaccuracies in the presence of non-linear dependencies among the system's physical variables. To address the impact of this assumption on network accuracy, the one-root-node network depicted in Figure 40 has been trained with two sets of training data, where a square-root transformation on the values of E has been considered in one of the sets. The training data has been generated via a Monte Carlo simulation, where the input parameter E has been assigned a normal distribution with a standard deviation $\sigma(E) = 0.02\mu(E)$. As an initial analysis, given the fast computation associated with such a simple structure, two different sample sizes were considered (i.e., 1000 and 5000 runs per simulation) to investigate their impact upon the parameter learning algorithm. It was observed that a larger sample size did not provide any significant improvement in the results' accuracy, but instead caused a more intense computational effort for convergence to be reached. As a consequence, all the Monte Carlo simulations carried out henceforth consisted of 1000 runs, in light also of the demanding computational cost associated with much more complex structures to be investigated next.

Shown in Figure 41 is the comparison between the trained networks at the 2nd natural frequency. The results are also compared with the probability density function of the training data themselves, obtained from the Monte Carlo simulation. Despite the theoretical linear relationship between natural frequencies and $\sqrt{E}$ for the beam structure, the

power transformation seems to increase the discrepancy between the parameters' distributions before and after training, where no evidence was included to compute the marginal probabilities of the child nodes. This apparent incongruity is due to the fact that the square root of a Gaussian quantity is not Gaussian. It is, however, useful to notice that the error introduced by linearly regressing a non-linear relationship seems lower than the one generated by the use of a non-Gaussian training data set to fit a perfectly linear relationship. In light of this deterioration in the parameters' statistical description, as well as the fact that the nature of the training data may, at times, be out of the analyst's control, no power transformation has been used for any of the following results, where linear regression becomes therefore the main source of error in the network training process.

Another important aspect to be taken into account is the capability of the network to accurately estimate system parameters even when the training data is affected by error, e.g. a bias. That being the case, the network could be recalibrated by redefining the prior probability for any of the root nodes. The effect of a biased training data set upon the estimation error has been studied for the one-root-node network of Figure 40. The network has been initially trained with a biased data set corresponding to $E \sim N(\mu, \sigma) = N(0.90 \times 114\,\mathrm{GPa}, 0.018 \times 114\,\mathrm{GPa})$, while the prior probability of the root node has then been changed to $E \sim N(\mu, \sigma) = N(114\,\mathrm{GPa}, 0.02 \times 114\,\mathrm{GPa})$, with a 10% bias being assumed for both the mean and the standard deviation. Depicted in Figure 42, the results of this recalibration indicate that an update of the prior probability causes a reduction in the bias associated with the natural frequencies, thus showing the capability of the network to overcome the effect of inaccurate biased training. Moreover, this reveals the ability of the network to establish consistent relationships among the node quantities, provided that all the training data sets are biased and/or skewed in a consistent way so that the intrinsic relationships between the variables are being preserved. Presented in the following sections are the results addressing direct and indirect propagation of uncertainty and evidence associated with both the one-root-node and the three-root-node Bayesian networks.
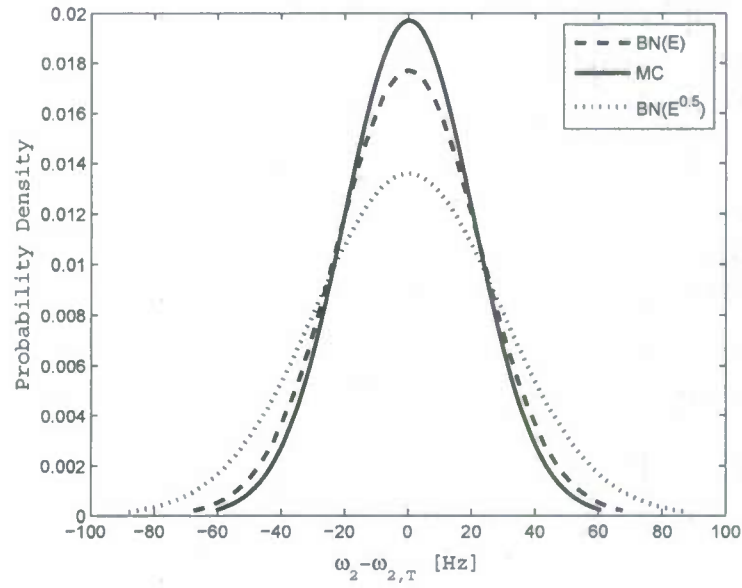
Figure 41: Beam: effect of network training; error between ω_2 and its reference value $\omega_{2,T}$.
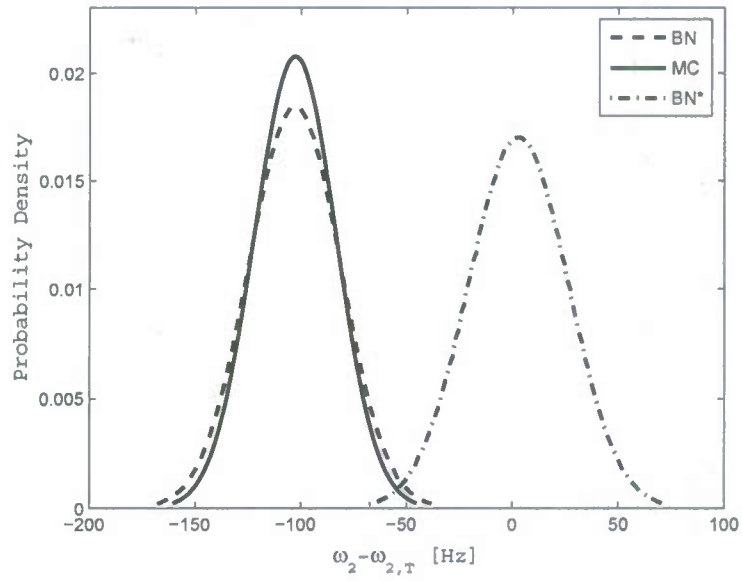
Figure 42: Beam: effect of a modified prior probability (BN*) on a trained network (BN).

4.3.1 One-root-node Bayesian Network

The one-root-node Bayesian network consists of eleven nodes. It represents a structural problem where an input parameter uncertainty is assumed for the beam's modulus of elasticity E and its impact on the first ten natural frequencies is investigated. The training data set has been obtained via Monte Carlo simulations on the finite-element model, under the assumption of normally distributed uncertainty for E. Furthermore, an intentional bias error has been introduced as a difference between the mean value of the normal distribution used in the Monte Carlo simulation itself, and the same quantity's value for the actual physical system, whose input and performance parameters are supposedly observed via other means (e.g., experiments) and treated as deterministic in nature. As a note, results associated with the simulated physical system's quantities will be herein referred to as "reference" or "true" values and identified by the subscript T.

4.3.1.1 Direct Problem

In the case of the simple Bayesian network of Figure 40, direct propagation of evidence corresponds to fixing Young's modulus E, the parent node, to the value 114 GPa, and computing the marginal probabilities associated with the natural frequencies, i.e. the child nodes. Table 11 illustrates the effect of such evidence inclusion on the nodes' statistical moments μ and σ for a network initially affected by some bias, where the percentage relative error δ for ω_i is defined as follows:

$$\delta_{\omega_i} = 100 \times \frac{\mu(\omega_i) - \omega_{i,T}}{\omega_{i,T}} \tag{34}$$

where the same definition is also used for the system input parameters. The effect is twofold: the bias is strongly diminished and the variability of almost all the frequencies is also reduced. Better improvement can be observed for the higher modes, while the variability associated with the first mode has changed only slightly. As indicated by Figures 41 and 42, this effect is due to the training procedure. In fact, network training causes a change in the distributions of the various quantities with respect to their Monte Carlo simulation results, where this discrepancy is higher for the lower modes and practically vanishes for

Table 11: Beam: effect of evidence on root-node E upon the child nodes' marginal probabilities.

BN with no evidence

Reference Value $\omega_{i,T}$ [Hz]	$\mu(\omega_i)$ [Hz]	δ [%]	$\sigma(\omega_i)$ [Hz]
323.25	306.67	-5.13	10.47
2007.5	1904.52	-5.13	21.61
5541.5	5257.24	-5.13	53.83
5636.5	5347.35	-5.13	54.72
10643	10096.72	-5.13	102.08
16911	16042.95	-5.13	161.72
17159	16278.85	-5.13	164.09
24897	23620.1	-5.13	237.86
28187	26741.31	-5.13	269.24
33663	31936.24	-5.13	321.48

$i = 1, \ldots, 10$

BN with evidence $E = 114$ GPa

Reference Value $\omega_{i,T}$ [Hz]	$\mu(\omega_i)$ [Hz]	δ [%]	$\sigma(\omega_i)$ [Hz]
323.25	323.68	0.13	10
2007.5	2010.23	0.14	10
5541.5	5549.05	0.14	10.01
5636.5	5644.16	0.14	10.01
10643	10657.15	0.13	10.02
16911	16933.44	0.13	10.06
17159	17182.43	0.14	10.06
24897	24931.16	0.14	10.12
28187	28225.62	0.14	10.16
33663	33708.9	0.14	10.22

$i = 1, \ldots, 10$

the higher ones. Due to the symmetric structure of the network, this behavior could be ascribed to the different orders of magnitude associated with each child node and its impact within the network. Moreover, as expected, the percentage relative error δ is the same for all the nodes because of the network's symmetric layout and the nature of the relationship relating E to each natural frequency of the beam, where their numerical order is purely descriptive. A similar reasoning applies to the trend of the frequencies' variability once evidence is introduced.

4.3.1.2 Inverse Problem

As observed for the case of direct propagation, the introduction of evidence at the parent node can help the Bayesian network to better estimate the statistical parameters associated with any child node. The inverse problem consists of introducing a piece of evidence at some child node. In order to propagate throughout the entire network, the infused information has to travel backwards with respect to the nominal direction of certain node-to-node links. Despite the fact that the inverse problem is usually more complex to handle, it may be more useful in terms of updating a model's parameters, especially since evidence is often available at the output level. As an example, illustrated in Figures 43-46 is the impact of evidence infusion at the child nodes (i.e., known values of frequencies) upon the distributions of E and the 10th natural frequency. As the number of observations increases, i.e. the values of more natural frequencies are made available, the mean values of E and the remaining unknown natural frequencies approach closer to their corresponding reference values together with a steady reduction in their standard deviation. Of course, evidence becomes significantly more important when the network is affected by uncertainty in the training data (e.g., bias due to measurement inaccuracy). In the specific case, two training data sets are being compared, corresponding to $E \sim N(\mu, \sigma) = N(0.90 \times 114\,\mathrm{GPa}, 0.018 \times 114\,\mathrm{GPa})$ (biased case) and $E \sim N(\mu, \sigma) = N(114\,\mathrm{GPa}, 0.02 \times 114\,\mathrm{GPa})$ (unbiased case). In the case of no bias within the training data, the effect of evidence is primarily focused on the variability associated with a given node's estimate (i.e., its mean value), whereas both mean and standard deviation of a node do benefit from the introduction of more and more evidence in the presence of bias. With regards to Figures 44 and 46, it is worth noting that the discrepancy in standard deviation between the bias and no-bias cases is exclusively due to different $\sigma(E)$'s employed to generate the two training data sets.

4.3.2 Three-root-node Bayesian Network

In the three-root-node Bayesian network, shown in Figure 40, the parent nodes represent Young's modulus E and the beam cross-section dimensions, width C and thickness T. The training data used to establish the links in the network have been generated via a Monte
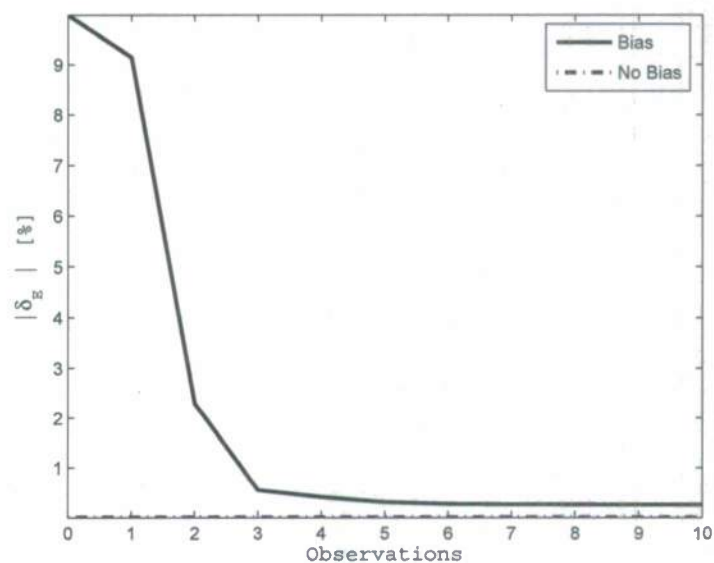
Figure 43: Beam: effect of evidence on the child nodes upon the relative error on E.
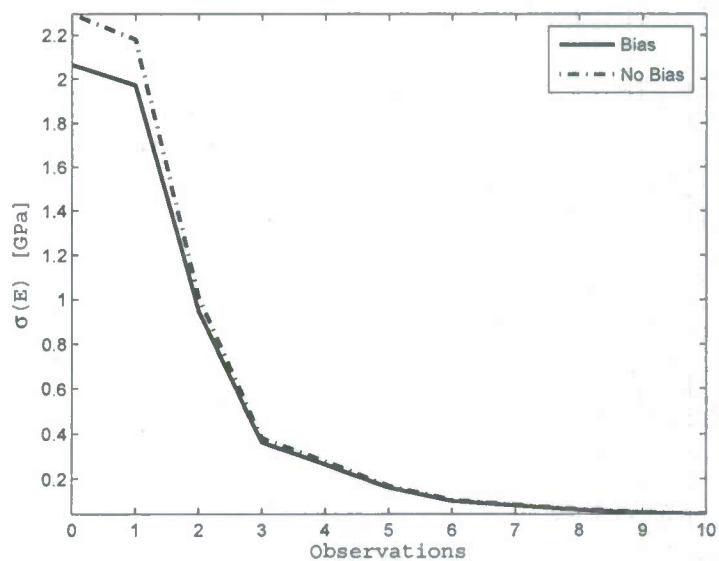
Figure 44: Beam: effect of evidence on the child nodes upon the variability of E.
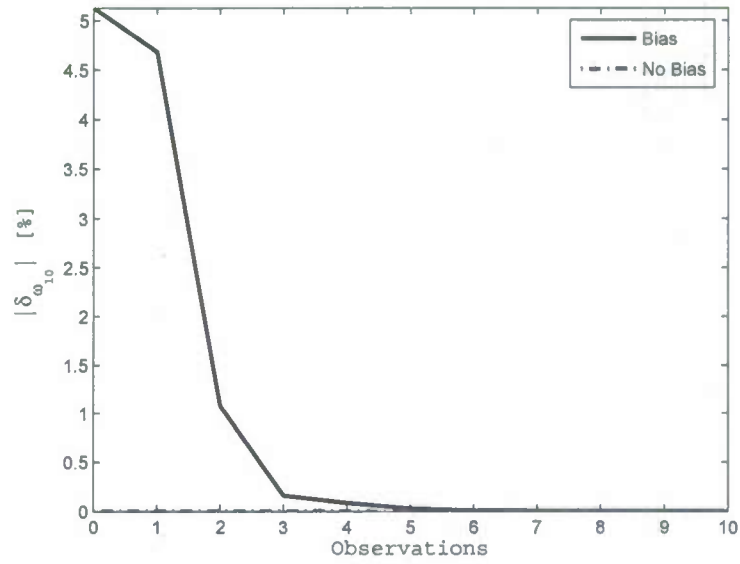
Figure 45: Beam: effect of evidence on the child nodes upon the relative error on ω_{10}.
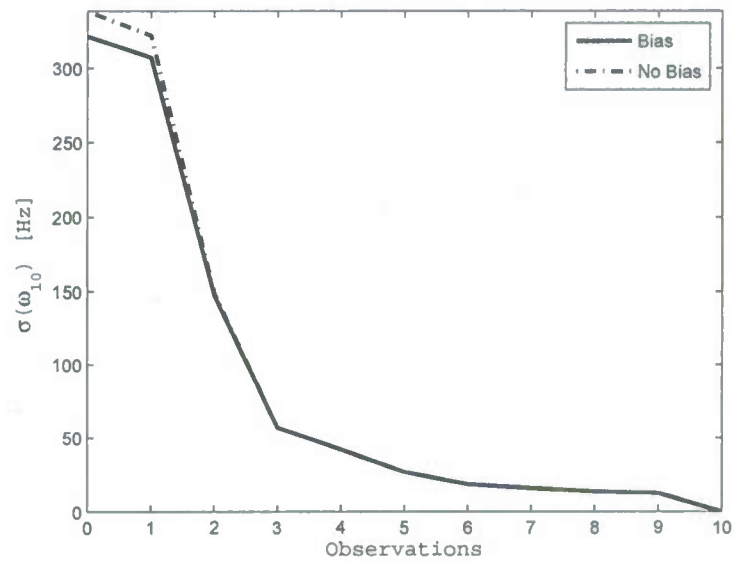
Figure 46: Beam: effect of evidence on the child nodes upon the variability of ω_{10}.

Table 12: Beam: statistical moments of root nodes.

	Monte Carlo Sim.		BN (no evidence)	
Root Node	μ	σ	μ	σ
E [GPa]	114.02	2.29	114.01	2.29
C [cm]	15.32	0.77	15.33	0.77
T [cm]	2	0.1	2	0.14

Table 13: Beam: statistical moments of child nodes.

	BN with E, C, T (no evidence)	
Child Node	$\mu(\omega_i)$ [Hz]	$\sigma(\omega_i)$ [Hz]
ω_1	323.11	24.82
ω_2	2006.57	138.95
ω_3	5476.75	254.56
ω_4	5698.34	159.7
ω_5	10635.82	687
ω_6	16721.96	469.94
ω_7	17335.05	708.5
ω_8	24876.24	1447.27
ω_9	28187.81	283.72
ω_{10}	33631.84	1838.95

$i = 1, \ldots, 10$

Carlo simulation where each variable has been assumed to vary as a Gaussian distribution $N(\mu, \beta\mu)$, where the values $\beta = 2\%$ for E and $\beta = 5\%$ for C and T have been selected. Tables 12 and 13 list the first two statistical moments of the variables' probability density functions resulting from the training procedure.

For a Bayesian network with more than one root node, the distinction between direct and inverse problems is not as well defined as in the one-root-node case. In fact, a unilateral direction of propagation of evidence cannot be clearly identified, as evidence introduced at any of the root nodes will affect both the child nodes and the other root nodes. Therefore, in this context, those cases where evidence is introduced at the root nodes will be denoted as "direct problems", whereas in the case of "inverse problems" evidence is introduced at the child nodes.

4.3.2.1   Direct Problem

The results associated with observations on E, C, and T are listed in Tables 14-17, where a bias has been introduced in the form of a 10% error in their values associated with the "true" physical system. On the one hand, when considered separately, each piece of evidence seems to be incapable of reducing significantly either the bias or the variability of the nodes with respect to the no-evidence scenario. Out of the three, evidence on T has the strongest impact, while the network is rather insensitive to evidence on C. As a matter of fact, according to Bernoulli beam theory, a cantilevered beam's natural frequency is proportional to $T\sqrt{E}$, whereas there exists no dependence upon C. In light of this observation, the linear-link approximation only affects the arcs connected to E, whereas the non-null arcs originating from node C appear to be a mere fabrication of the training procedure. Such a situation highlights the potential negative consequences associated with the modeling within the network of weak causal relationships, which may still cause the network to respond to the inclusion of certain pieces of evidence whose impact should instead be theoretically null. Furthermore, given the symmetric topology of the Bayesian network with respect to each root node, the difference in sensitivity separately associated with E and T seems to be due primarily to the different power transformation relating each of them to the beam's natural frequencies. As an example, the marginal probabilities for the 5th natural frequency are illustrated in Figure 47 for the various types of evidence, where the statistical parameters used therein are those of Tables 14-16. On the other hand, as shown in Table 17, when observations on E, C and T are introduced concomitantly, the marginal probabilities of the child nodes are characterized by an even further reduction in their spread, as well as a stronger decrease in their bias error for the majority of the nodes. This behavior is in agreement with the expected trend between the network's decreasing variability and the increasing number of observed nodes.

4.3.2.2   Inverse Problem

The inclusion of evidence at the child nodes yields a monotonic decrease of the variability associated with the root nodes E, C, and T. The estimates of the mean values though do

Table 14: Beam: effect of evidence on E upon the nodes' marginal probabilities.

Node	Reference Value	μ(Node)	δ [%]	σ(Node)
E [GPa]	102.6	-	-	-
C [cm]	13.77	15.33	11.33	0.77
T [cm]	1.8	2	11.11	0.14
ω_1 [Hz]	276.07	306.92	11.17	24.61
ω_2	1717.5	1906.05	10.98	137.48
ω_3	4753.4	5208.32	9.57	248.79
ω_4	5347.3	5407.07	1.12	148.6
ω_5	9162.1	10103.12	10.27	678.62
ω_6	14836	15885.56	7.07	438.88
ω_7	16043	16465.92	2.64	686.65
ω_8	21630	23630.56	9.25	1425.47
ω_9	26741	26776.25	0.13	10.17
ω_{10}	29393	31947.87	8.69	1807.58

Table 15: Beam: effect of evidence on C upon the nodes' marginal probabilities.

Node	Reference Value	μ(Node)	δ [%]	σ(Node)
E [GPa]	102.6	114.01	11.12	2.29
C [cm]	13.77	-	-	-
T [cm]	1.8	2	11.11	0.14
ω_1 [Hz]	276.07	323.12	17.04	24.82
ω_2	1717.5	2006.6	16.83	138.95
ω_3	4753.4	5466.34	15	254.51
ω_4	5347.3	5708.73	6.76	159.62
ω_5	9162.1	10635.49	16.08	687
ω_6	14836	16691.87	12.51	469.71
ω_7	16043	17364.16	8.24	708.35
ω_8	21630	24874.08	15	1447.27
ω_9	26741	28187.88	5.41	283.72
ω_{10}	29393	33628.09	14.41	1838.95

Table 16: Beam: effect of evidence on T upon the nodes' marginal probabilities.

Node	Reference Value	μ(Node)	δ [%]	σ(Node)
E [GPa]	102.6	114.01	11.12	2.91
C [cm]	13.77	15.33	11.33	0.77
T [cm]	1.8	-	-	-
ω_1 [Hz]	276.07	291.02	5.42	10.52
ω_2	1717.5	1810.84	5.43	22.55
ω_3	4753.4	5137.26	8.08	90.8
ω_4	5347.3	5512.76	3.09	92.76
ω_5	9162.1	9667.24	5.51	107.64
ω_6	14836	16172.73	9.01	269.84
ω_7	16043	16398.56	2.22	267.55
ω_8	21630	22841.62	5.6	251.22
ω_9	26741	28187.84	5.41	283.72
ω_{10}	29393	31051.94	5.64	339.83

Table 17: Beam: effect of evidence on E, C and T upon the nodes' marginal probabilities.

Node	Reference Value	μ(Node)	δ [%]	σ(Node)
E [GPa]	102.6	-	-	-
C [cm]	13.77	-	-	-
T [cm]	1.8	-	-	-
ω_1 [Hz]	276.07	274.84	-0.45	10
ω_2	1717.5	1710.36	-0.42	10.05
ω_3	4753.4	4858.43	2.21	72.87
ω_4	5347.3	5231.89	-2.16	71.8
ω_5	9162.1	9134.21	-0.3	11.75
ω_6	14836	15306.24	3.17	210.63
ω_7	16043	15558.54	-3.02	202.23
ω_8	21630	21593.78	-0.17	22.41
ω_9	26741	26776.34	0.13	10.17
ω_{10}	29393	29364.22	-0.1	32.6
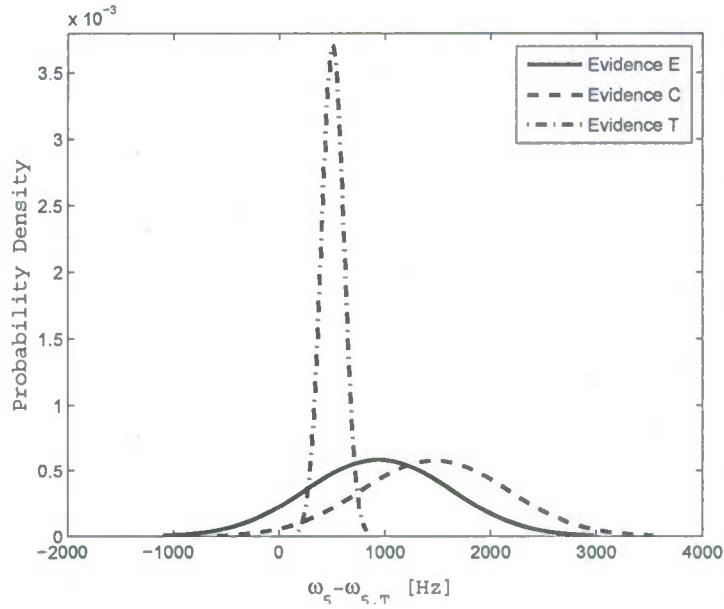
Figure 47: Beam: effect of evidence on the root nodes upon the probability of ω_5.

not necessarily improve monotonically as more observations become available. Examples of these trends are shown in Figures 48 and 49 for the modulus of elasticity E.

As regards the child nodes, both the bias error and the standard deviation associated with each natural frequency reduce monotonically as the number of observations increases. Illustrated in Figures 50 and 51 are the absolute relative percentage error and the standard deviation, as a function of evidence, for the 10th natural frequency, where similar trends were also observed for the other child nodes. In the case of no bias being present in the training data, the non-monotonic behavior of the relative error can be explained as a simple manifestation of the network adjusting to the new evidence in the presence of non-linearities and internal numerical error. Furthermore, for the system at hand, such oscillations are of low magnitude and negligible, with a percentage relative error on any given estimate of the order of 0.1% or lower.

The results obtained for the direct and inverse problems confirm the positive impact associated with the introduction of evidence within a Bayesian network, even though it may be more sensitive to certain nodes than others, as observed, for instance, for the

94
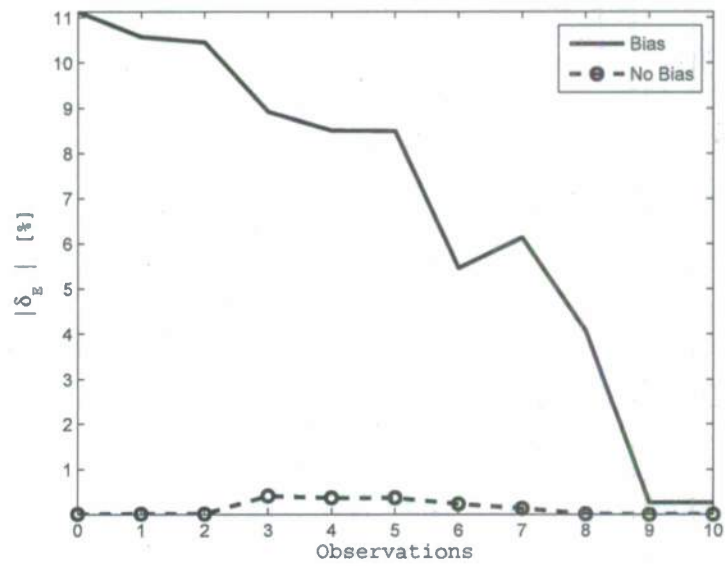
Figure 48: Beam: effect of evidence on the child nodes upon the relative error on E.
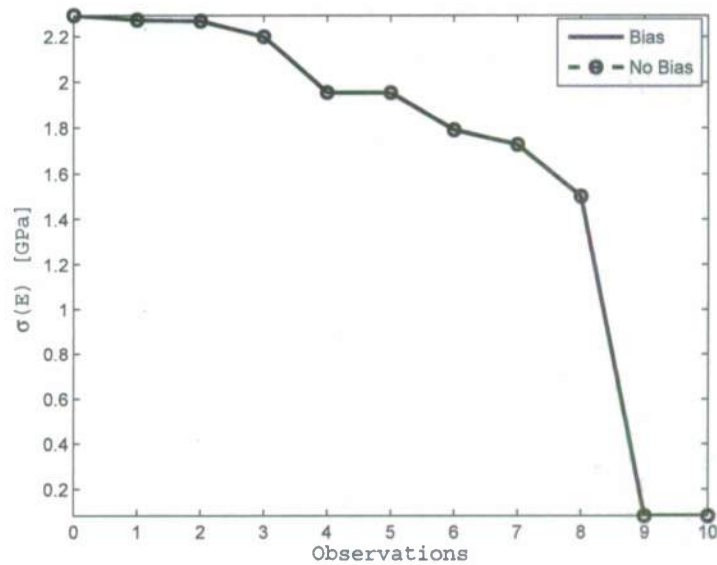
Figure 49: Beam: effect of evidence on the child nodes upon the variability of E.
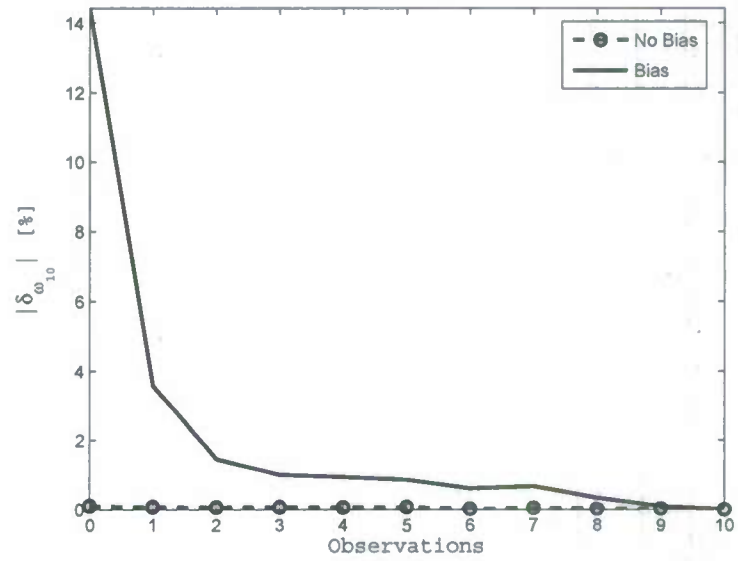
Figure 50: Beam: effect of evidence on the child nodes upon the relative error on ω_{10}.
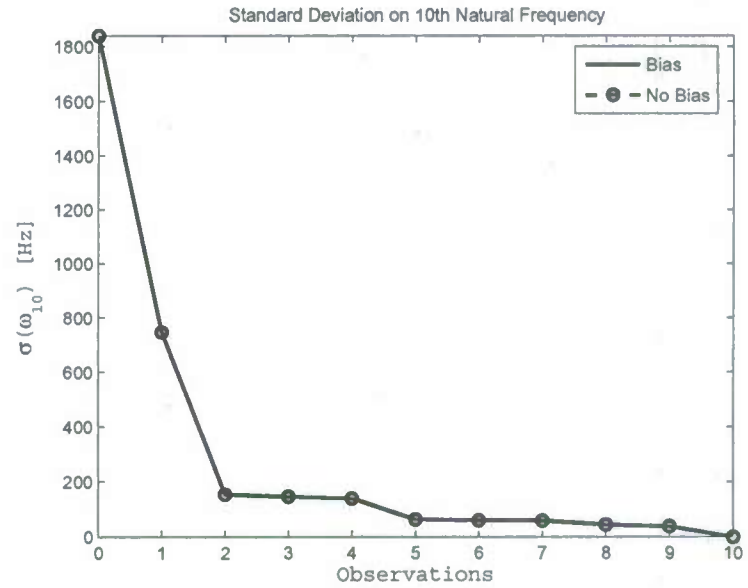
Figure 51: Beam: effect of evidence on the child nodes upon the variability of ω_{10}.

direct problem. The observed trend is in agreement with beam theory according to which frequencies are more sensitive to thickness variations than to changes in Young's modulus. Furthermore, the modeling of causal relationships unwarranted by the data, but artificially created by the learning algorithm, may hinder the quality of the results by altering the effect of evidence infusion. Finally, it is expected that convergence to the reference values and consequent error reduction will become harder to achieve as the physics of the problem and the network's structure evolve in complexity, encompassing a higher number of nodes and/or links.

4.3.3   Bayesian Network with Model Noise

In practical situations certain quantities of a system are not explicitly represented within a network. For instance, that occurs when the variability on a given parameter is not observed or cannot be easily measured, or when network simplicity is being preferred to accuracy. As a consequence, the uncertainty in certain system output quantities due to the variability of non-modeled inputs appears in the form of noise within the modeled nodes of the network. In other words, the training data contain spurious uncertainty because its sources cannot be explicitly identified. This may be an analyst's desire in some cases, but in other circumstances it may simply originate from limitations in the analytical framework or the test setup. In order to address the effect of non-modeled phenomena, the one-root-node/ten-child-node Bayesian network with noise of Figure 52 was investigated, where E was the only input parameter included. Noise was introduced by training the given network with a data set generated via a Monte Carlo simulation in which E, C and T were all varied, with the understanding that C should play no role, at least from a theoretical standpoint. Shown in Figures 53 and 54 is a comparison between the given network and the layouts presented in the previous sections, where no bias error was introduced so as to isolate the effect of noise.

In the absence of noise, the one-root-node network has the fastest response to evidence, whereas the introduction of noise reduces its sensitivity to evidence in one case (Figure 53), and practically eliminates it in the other, as is the case for the variability of the
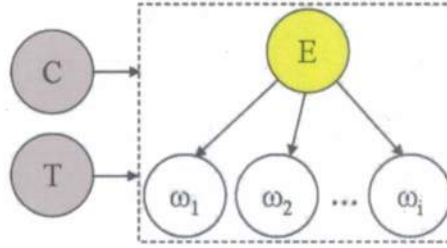
Figure 52: One-root-node Bayesian network with noise.

10th natural frequency (Figure 54). Both in the three-root-node network and in the one with noise, the spread of E shows similar trends, thus indicating that the effect of noise primarily concentrates on the child nodes since E, C, and T are indeed independent of one another. On the one hand, this elementary case study indicates that the presence of non–modeled uncertainty can make the response of the dependent nodes in a Bayesian network stiffer with respect to evidence, as noise in the training data inevitably contaminates the variables' interrelations. On the other hand, when properly verified for the problem at hand, the appearance of such stiffness could be interpreted as a warning sign that certain phenomena are not being fully captured and/or properly modeled.

4.4 BN-based Uncertainty Analysis on a Bladed-disk Sector

The procedure illustrated in the previous sections has also been employed to analyze a structurally more complex system, namely the disk sector described in Table 2 and depicted in Figure 2. The objective, once again, is to assess the feasibility of using a Bayesian network to integrate evidence, available for any part or input/output parameter of the system, and have it propagate throughout the entire statistical model for a consistent update of all the performance and input parameters of the system. Given the intense computational workload required by the Monte Carlo simulation, the number of runs used was set equal to 1000 and no cyclic compatibility constraints were included at this stage, which, however, leads to no significant detriment to the objective and validity of this study in terms of system complexity. The use of an alternative technique (e.g., surrogate model) would be needed to reduce the larger computational effort associated with the full bladed disk. The number of
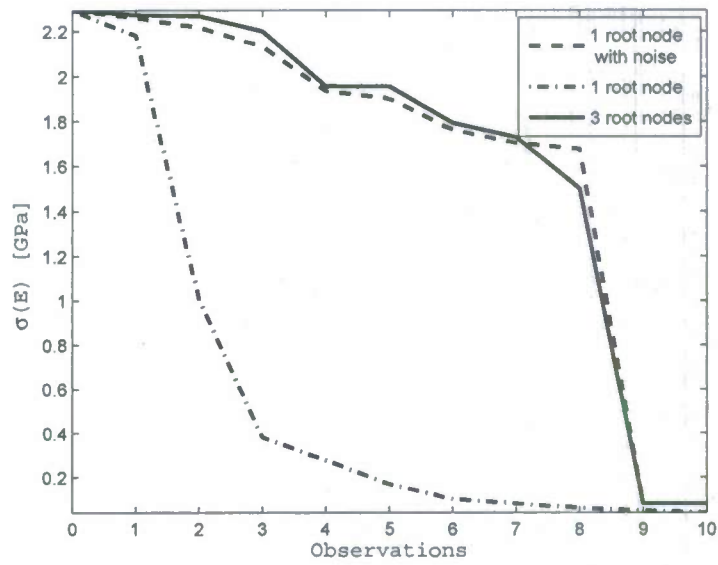
Figure 53: Beam: effect of non-modeled uncertainty upon the variability of E.
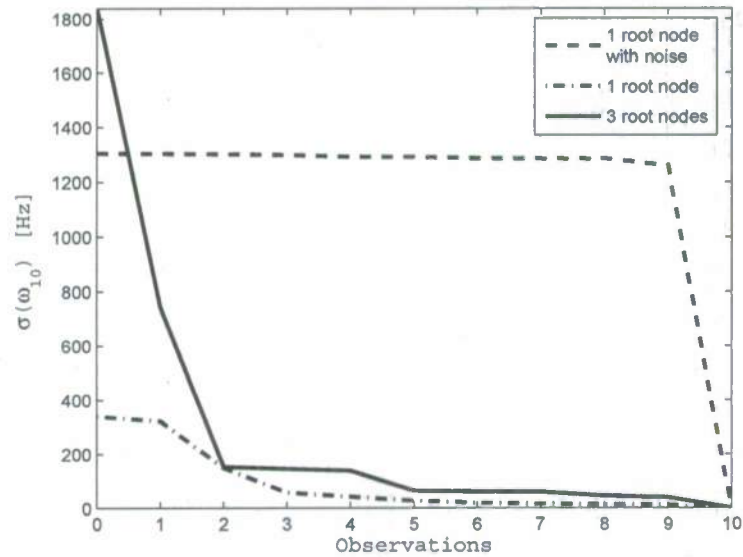
Figure 54: Beam: effect of non-modeled uncertainty upon the variability of ω_{10}.

Table 18: Disk sector: physical systems and nominal model characteristics.

Quantity	Nominal System Q_0	Physical System Q_1	Physical System Q_2	Physical System Q_3
$E = 114$ [GPa]	E	E	$0.9E$	$0.9E$
$\rho = 4430$ [Kg/m^3]	ρ	0.97ρ	0.97ρ	ρ
$k = 1$	k	k	k	k
ω_1 [Hz]	259.45	263.43	249.91	246.14
ω_2	555.94	564.47	535.50	527.41
ω_3	1708.9	1735.1	1646.1	1621.2
ω_4	1934.4	1964.1	1863.3	1835.2
ω_5	3701.8	3758.6	3565.7	3511.8
ω_6	4029.8	4091.6	3881.6	3823.0

performance parameters was limited to the first six natural frequencies, while uncertainty was introduced for material properties (i.e., Young's modulus E and mass density ρ) and geometry, via random radial scaling of the entire sector. The geometry radial scaling factor k is herein used as a simplified characterization of manufacturing tolerances, under the constraints imposed by adjacent sectors in a fully modeled disk. For each of the case studies presented next, the training data sets were generated assuming that the quantities being varied followed a Gaussian distribution of the form $N(\mu, \beta\mu)$ with means equal to the values for a nominal system, and β equal to 2%, 5% and 1.5% for E, ρ and k, respectively. In order to address the impact of possibly biased training data, evidence was also generated for physical systems with material properties different from those of the nominal model. A summary of the numerical values for the nominal system's model as well as the real systems under investigation is given in Table 18.

4.4.1 One-root-node Bayesian Network

In the case of the one-root-node Bayesian network depicted in Figure 40, uncertainty was introduced in the form of a normally distributed Young's modulus $E \sim N(\mu, \sigma) = N(114\,\text{GPa}, 0.02 \times 114\,\text{GPa})$, while mass density and scaling factor were assigned their nominal values. The necessary training data was obtained via a Monte Carlo simulation performed using the probabilistic toolbox within the commercial finite-element package ANSYS©.

4.4.1.1 Direct Problem

As for the case of direct propagation, illustrated in Table 19 and Figures 55-56 is the effect of biased and unbiased training data upon the network's capability to estimate the system's modal performance parameters in the presence of evidence at the root node E. With no loss of generality, in this case as well as the following ones, biases have been embedded in the evidence rather than at the Monte Carlo simulation level so as to limit the computational effort. As shown in the table, the introduction of a piece of evidence at the root node E causes the same variability reduction for any of the child nodes, independently of the bias. The bias, however, affects the capability of the network to accurately estimate the system's natural frequencies. More specifically, in the presence of a shift in the reference frequencies, partly or entirely due to a discrepancy in mass density between the nominal system and the physical one, the evidence cannot lead to a decrease in such biases, as those are associated with a non-modeled source of uncertainty. Frequency biases due only to a wrong estimate of Young's modulus are, instead, reduced when evidence is included.

Table 19: Disk sector: effect of evidence on E upon the child nodes' marginal probabilities.

	Monte Carlo Sim.	BN No evidence	BN Evidence on E
$\sigma(\omega_1)$ [Hz]	2.61	10.36	10.0
$\sigma(\omega_2)$	5.59	11.58	10.0
$\sigma(\omega_3)$	17.18	20.53	10.0
$\sigma(\omega_4)$	19.45	22.63	10.0
$\sigma(\omega_5)$	37.22	40.12	10.0
$\sigma(\omega_6)$	40.52	43.46	10.0

4.4.1.2 Inverse Problem

The inverse problem for the one-root-node Bayesian network consists of the introduction of evidence at any or all of the child nodes. Depicted in Figures 57-59 is the dependence of the random variables E and ω_6 upon three distinct sets of evidence associated with the configurations of Table 18. As expected, the variability associated with each unknown node decreases as the amount of available evidence increases. Observations for the child nodes
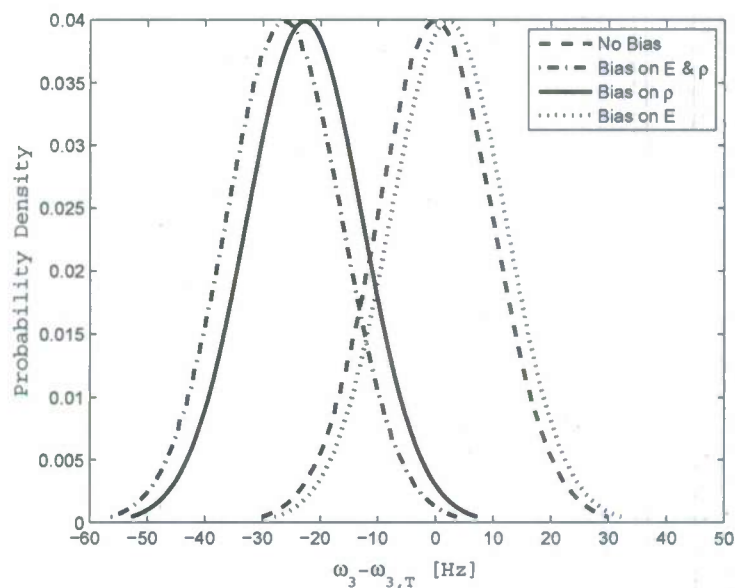
Figure 55: Disk sector: effect of evidence on E upon the marginal probability of ω_3.
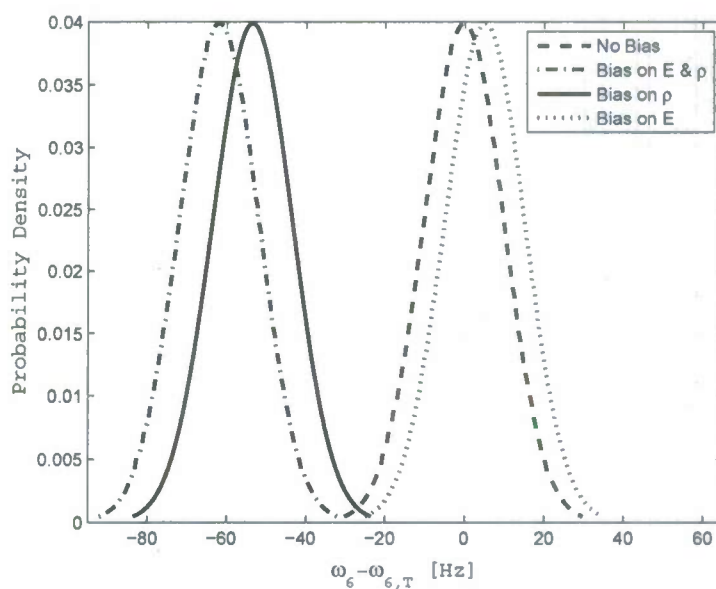
Figure 56: Disk sector: effect of evidence on E upon the marginal probability of ω_6.
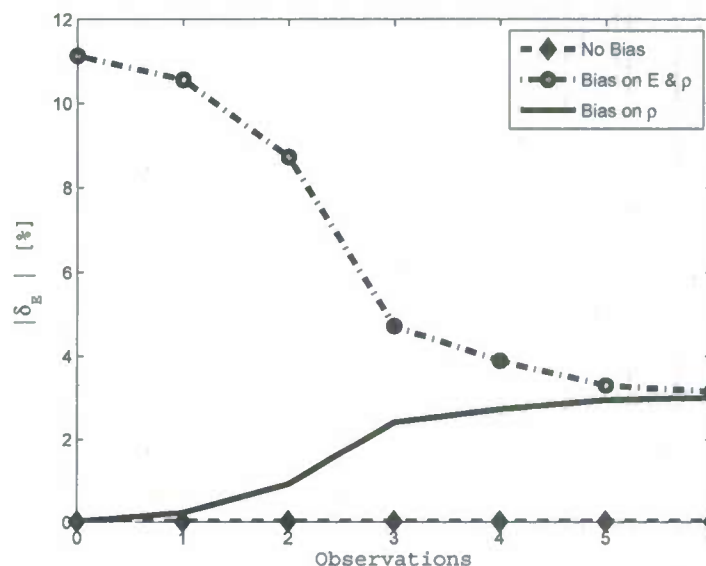
Figure 57: Disk sector: effect of evidence on the child nodes upon the relative error on E.

are input, for convenience, in a sequential order, and are assumed to be deterministic in nature, thus causing the curves in Figures 58 and 59 to eventually go to zero for any biased or unbiased evidence. While the process of evidence infusion is able to reduce the impact of biases for the natural frequencies, that is not the case for Young's modulus. On the contrary, as shown in Figure 57, the presence of bias in the mass density ρ alone causes a divergent effect for E, while it prevents the network from removing entirely a preexisting bias on E itself. In both cases, however, this network seems incapable of counteracting the effect of a non-modeled uncertainty associated with ρ. This may also be partially due to the non-linearities inherent in the structure not being fully captured under the assumption of node-to-node linear Gaussian links.

4.4.2 Three-root-node Bayesian Network

The three-root-node Bayesian network for the disk sector is similar to the one depicted in Figure 40, where the quantities C and T have been replaced, in this case, with the mass density ρ and the geometry scaling factor k. The training data for the Bayesian network
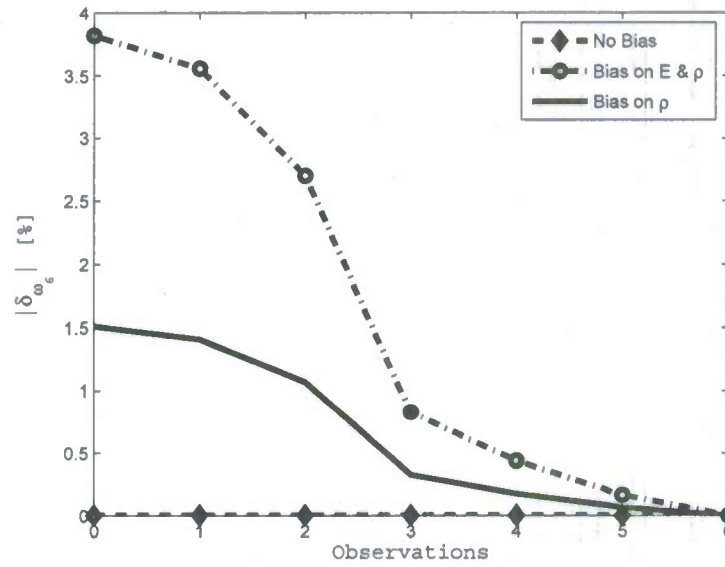
Figure 58: Disk sector: effect of evidence on the child nodes upon the relative error on ω_6.
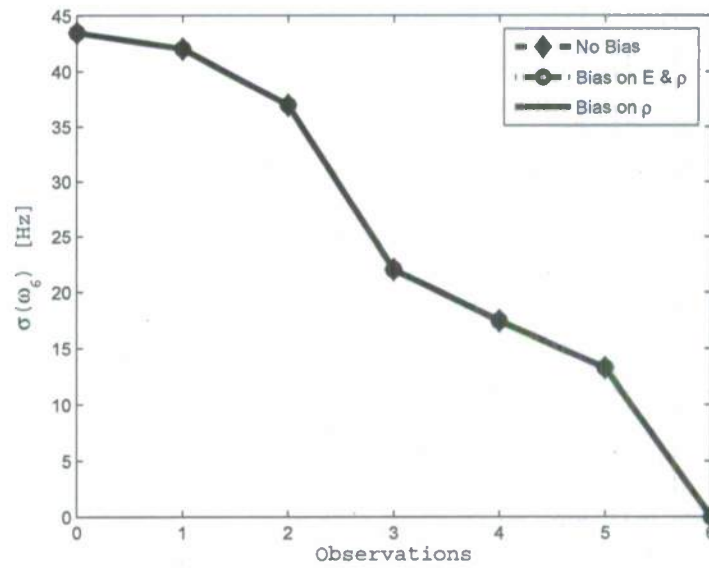
Figure 59: Disk sector: effect of evidence on the child nodes upon the variability of ω_6.

is obtained through Monte Carlo simulations with E, ρ and k assumed to have Gaussian distributions of the form $N(\mu, \beta\mu)$, with nominal values used as means, and β set equal to 2%, 5%, and 1.5%, respectively. Moreover, the effect of bias on this network was investigated by utilizing evidence associated with the system configurations Q_1, Q_2, and Q_3 of Table 18.

4.4.2.1 Direct Problem

Direct propagation has been investigated for the four configurations given in Table 18. In the case of the nominal system Q_0 (i.e., no bias in the data), evidence on ρ is characterized by the highest impact in terms of reduction in the variability associated with the natural frequencies. Evidence on E and k, instead, yield very minor improvement in the confidence of the remaining unknown nodes. Moreover, evidence applied separately on any pair of root nodes yields the same variability in the estimate of the third parent node.

For the physical system Q_1, in the presence of bias generated via a non-nominal mass density, the network appears to be rather insensitive to evidence on E and scaling factor k in terms of a decrease in uncertainty within the nodes. As for the node estimates themselves, they approach their reference values only when evidence on ρ is introduced, whereas the biases do not change significantly with respect to the zero-evidence scenario in the other cases.

As for the physical system Q_2, evidence on E yields very minor fluctuations in the variability of the other unknown nodes. In other words, the network seems to be stiffened to evidence on E when compared to the zero-evidence condition. The variability at the root-node level is also unaffected when information about the mass density ρ is made available, whereas the same evidence on ρ causes a significant reduction in the standard deviation of the child-node frequencies. Furthermore, the nodal standard deviations are also rather insensitive to evidence on k. As for the biases, only the observation on E causes a meaningful reduction in them.

The physical system Q_3 is characterized only by a biased Young's modulus. In this scenario, evidence on E eliminates the bias, but does not yield any improvement in the variability of the other nodes, which is, instead, greatly decreased when evidence on ρ

is introduced. On the contrary, evidence on k causes no relevant decrease both in the estimates' biases and their spreads. As an example, numerical results for the physical system Q_2 are given in Table 20.

In conclusion, since the structure is characterized by different sensitivity levels with respect to given input parameters, so does its representative Bayesian model.

Table 20: Disk sector: effect of evidence on the root nodes upon the Bayesian network of system Q_2.

Percentage relative error δ [%]

	No Evidence	Evidence on E	Evidence on ρ	Evidence on k
E [GPa]	11.12	0	11.12	11.12
ρ [Kg/m^3]	3.09	3.09	0	3.09
k	-0.03	-0.03	-0.03	0
ω_1 [Hz]	4.01	-1.19	5.57	3.98
ω_2	4.01	-1.18	5.57	3.96
ω_3	4.01	-1.2	5.57	3.96
ω_4	3.98	-1.22	5.55	3.95
ω_5	3.97	-1.23	5.53	3.94
ω_6	3.98	-1.22	5.54	3.95

Standard Deviation σ

	No Evidence	Evidence on E	Evidence on ρ	Evidence on k
E [GPa]	2.39	0	2.39	2.39
ρ [Kg/m^3]	2767.99	2767.99	0	2767.99
k	0.10	0.10	0.10	0
ω_1 [Hz]	86.08	86.04	27.58	82.20
ω_2	206.35	206.27	109.90	175.04
ω_3	586.91	586.64	237.75	537.00
ω_4	637.73	637.41	195.36	607.50
ω_5	1237.58	1236.97	426.84	1162.35
ω_6	1364.66	1364.00	512.12	1265.68

4.4.2.2 Inverse Problem

In the case of observations available for the child nodes, the statistical moments associated with all the remaining unobserved child nodes follow the same pattern shown in Figures 60 and 61 (solid lines). More in detail, their standard deviation σ is a monotonically

decreasing function of evidence. As for the root nodes, Figure 62 indicates that the percentage relative error for E is independent of evidence for configuration Q_2, whereas the relative error on the mass density ρ increases from 3.1% for zero observations to 10.86% after six observations. The error associated with the scaling factor exhibits a peak value of 0.32% to drop then below 0.05% as more observations are made available. Trends are, instead, more regular when no bias is considered. As a consequence of these findings, it appears that the root-node estimates exhibit no clear dependence on evidence for different sources of bias. In fact, despite the expected reduction in variability as a function of evidence, the network may converge to values different from those corresponding to the given observations. Furthermore, the fact that in real scenarios no evidence is deterministic in nature should be taken into consideration for that introduces more uncertainty into the Bayesian network. This aspect may be addressed by modeling a given quantity and its measurement as two distinct nodes, as will be explained further in Chapter 5.

4.4.3   Bayesian Network with Model Noise

Similarly to what was previously done for the beam structure, the effect of noise has also been investigated for the disk sector, where it consists in additional uncertainty within a network due to non-modeled phenomena and/or causal relationships. This scenario has been herein simulated via a one-cause network trained with a data sample associated with three sources of uncertainty. Mass density and scaling factors were treated as hidden nodes, while E was explicitly modeled. Results are shown in Figure 60-63, where the three different network topologies of Figures 40 and 52 were compared against one another. Overall, the three-root-node network performs better than the one with noise in terms of filtering out the uncertainty associated with the child nodes, whereas its performance is worse at the root node E due to its low sensitivity to evidence, as already observed in the previous section. The one-root-node without noise, instead, performs satisfactorily for all the nodes and is able to steadily reduce the uncertainty introduced by the bias of physical system Q_2. Of course, its higher convergence rate is primarily due to the simpler topology and lower level of inherent uncertainty within its nodes.
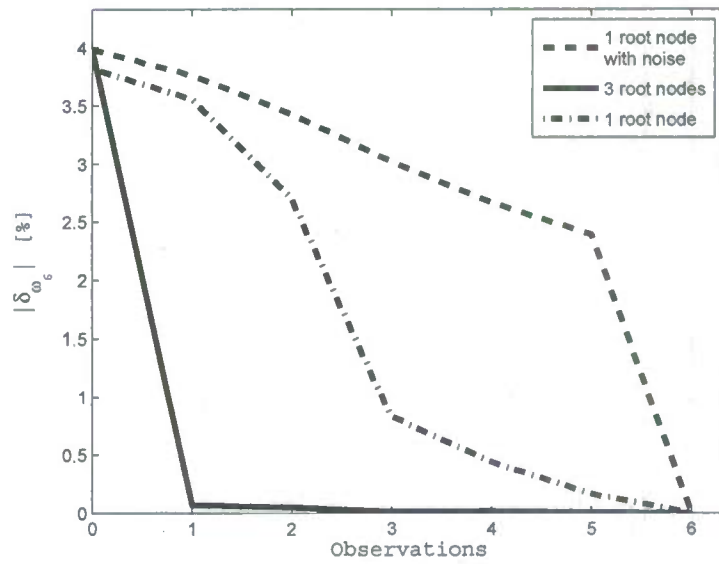
Figure 60: Disk sector: effect of non-modeled uncertainty upon the relative error on ω_6.
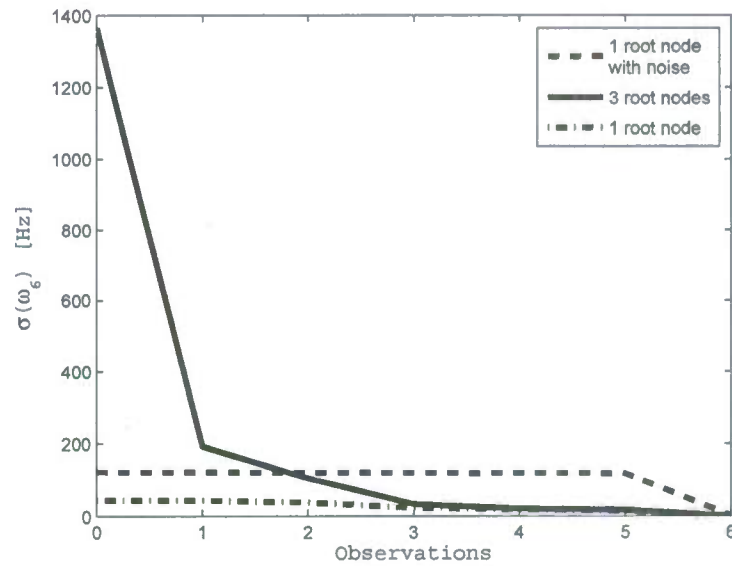
Figure 61: Disk sector: effect of non-modeled uncertainty upon the variability of ω_6.
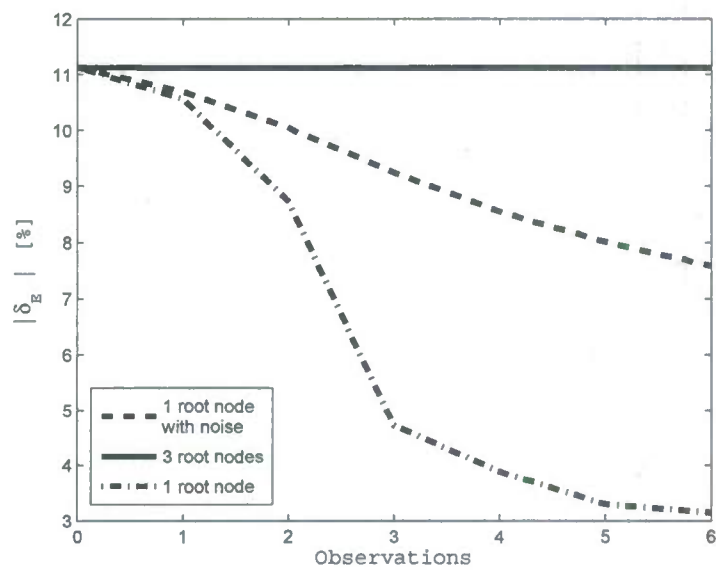
Figure 62: Disk sector: effect of non-modeled uncertainty upon the relative error on E.
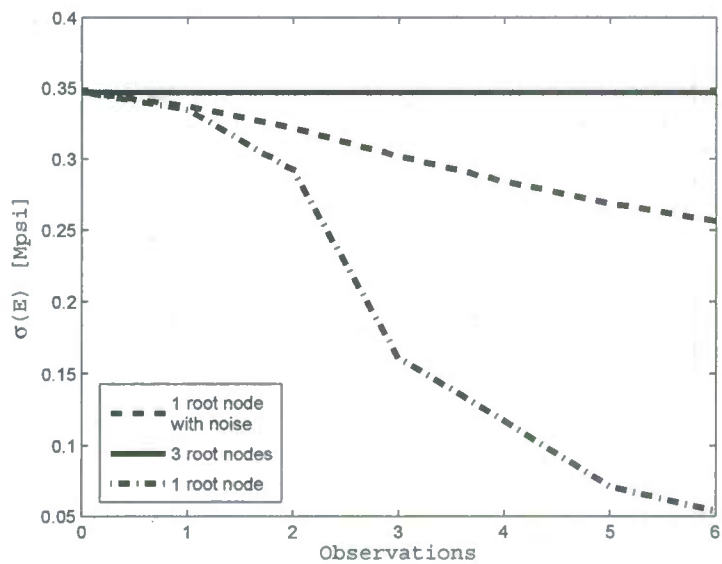
Figure 63: Disk sector: effect of non-modeled uncertainty upon the variability of E.

109

4.5 Summary

The use of Bayesian networks allows for a statistically rigorous synthesis of the results from system models and experimental data that provides indirect information on the parameters of the analytical models themselves. The feasibility of using Bayesian networks to model multi-directional uncertainty propagation has been assessed for a beam structure as well as a bladed disk sector where modal frequencies are evaluated as a function of material and geometric properties. Results show that the Bayesian network associated with a system retains well the system's inherent dependence and sensitivity trends among the given parameters, according to which it responds differently to various sources of evidence. As a consequence of such behavior, a particular piece of evidence may be more or less effective in estimating a system's input/output parameter as well as improving its confidence level, where, inevitably, such effectiveness is also influenced by network topology and quality of the training data. In fact, bias in the data could not always be removed, whereas the use of non-Gaussian data samples yielded even larger errors and uncertainty within the network's nodes and links. Overall, the use of a Bayesian network shows good potential in addressing, in a consistent manner, the problems of uncertainty propagation and quantification, as long as a good trade-off is reached among network topological complexity (i.e., the accuracy with which the physics of the problem is described), quality of the training data, and uncertainty in the evidence. Therefore, as discussed next, this statistical tool has been evaluated as a potential means to establish a unified framework for response prediction in structural dynamic applications.

CHAPTER V

BAYESIAN VIBRATORY RESPONSE ESTIMATION

5.1 *Response Inference via Bayesian Networks*

In order to combine information from the experiments with the knowledge from the analytical model, and account for variability from both, a Bayesian representation of the inference technique is constructed which permits the quantification and reduction of uncertainty as a function of the available experimental data. This process of integration is illustrated in Figure 64 for which three fundamental steps can be identified:

- Creation of an analytical/numerical experimentation framework representing the given real/experimental conditions;

- Establishment of a Bayesian network topology for response inference and population of its elements by means of the simulated experimental data; and

- Infusion of the real test data for the updating of the prior statistical information within the network.

Next, the simulation environment and the Bayesian network topology adopted for the assessment of a system's vibratory response are presented. It is to be reminded that the modal-based inference scheme is applied separately to each resonance condition. Hence, the Bayesian network is also resonance-specific and computation of its prior information is needed at each of those conditions.

5.1.1 Equivalent Numerical Experimentation

The first step in the uncertainty-quantification process is the construction of a simulated-experiment environment (e.g., a finite-element forced-response analysis) equivalent to the actual test setup, where equivalency is defined in terms of comparable levels of uncertainty within the results generated via the numerical/analytical framework and the corresponding

111
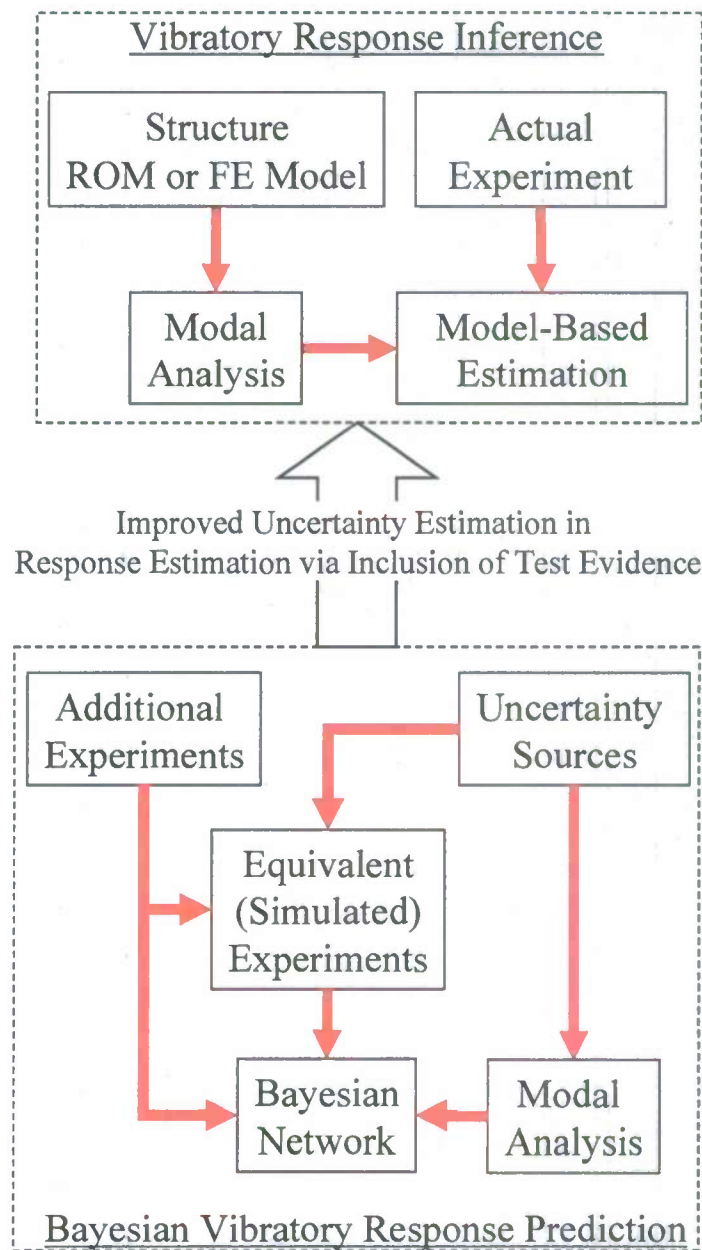
Figure 64: Bayesian model-based vibratory response inference procedure.

test data. In practical applications, not all the sources of uncertainty are detectable or observable, nor their impact can always be isolated in a comprehensive way. In this sense, simulated experimentation is not meant to duplicate reality, but to identify a set Θ^E of explanatory factors through which physical observations and corresponding uncertainties can be "equivalently" accounted for, even though such a set might not be at all exhaustive due to analytical limitations as well as a lack of complete knowledge about the structure and its true state. In fact,

$$\Theta^E = \{\theta_i^E, i = 1, \ldots, N_E\} \subseteq \Theta^T = \left\{\theta_j^T, j = 1, \ldots, N_T\right\} \tag{35}$$

where Θ^T represents, instead, the set of quantities, often unknown, which fully describe the physical system and its inherent random nature. Given an analytical experiment environment, the method of direct propagation of input-parameter uncertainties can be used to identify suitable sets Θ^E for any specific structure and loading condition, as well as to establish the statistical cause-effect relationships necessary to construct a Bayesian network. Furthermore, this approach also serves the purpose of a screening test, as it pinpoints which parameters, among the ones being investigated, are mostly responsible for the variability in the system's response, and which ones could be neglected with minimal loss of information. Besides reducing the number of nodes to be modeled within a Bayesian network, a screening test also permits to exclude cause-effect arcs which would otherwise be rather weak, and hence unresponsive to the propagation of evidence through them. This unresponsiveness leads to two main effects. On the one hand, a node whose connections to other nodes are weak can be updated effectively only through evidence infusion at that same node, as any information included at any other nodes will be damped out or will not propagate to it. For the same reason, evidence introduced at that node will also transfer weakly or not at all to its parent and child nodes and its effect will be therefore isolated. On the other hand, there is always the risk that the training procedure may establish a link between a pair of nodes which is stronger than what observed through the sensitivity analysis, thus explaining the variability in the data differently and leading to posterior probabilities for the network nodes that are unwarranted by the data.

According to the proposed response-estimation technique, in order to train a Bayesian network, data associated with both forced-response and modal analyses are to be generated. The commonly used approach of direct uncertainty propagation through Monte Carlo simulations may, however, incur a high computational cost, even for simple structures. Therefore, surrogate models based on standard polynomial interpolation [97] have been adopted to limit the number of finite-element analyses to be executed. More specifically, spline interpolation was used in the case of harmonic analyses to alleviate the dependance upon the spectrum's frequency resolution $\Delta\omega$. In fact, for a fixed value of $\Delta\omega$, the accuracy with which the response at resonance is computed varies as a function of the values of the independent-parameter vector $\boldsymbol{\theta}^E = \left[\theta_1^E, \ldots, \theta_{N_E}^E \right]$. As a consequence of that, the peak response, computed at any given point on the structure, exhibits a non-continuous behavior with respect to $\boldsymbol{\theta}^E$ which hinders the use of a continuous analytical model to represent better their relationship and smoothen the observed discontinuities. As an alternative to the use of spline interpolation, $\Delta\omega$ could be optimized, through some iterative process, for each value of $\boldsymbol{\theta}^E$, or a very high frequency resolution could be employed to interrogate the entire domain of $\boldsymbol{\theta}^E$, with consequent increase in the computational cost in both cases.

Once the surrogate models relating peak responses and modal quantities to the independent parameters are established, uncertainty can be propagated by assigning appropriate probability density functions to the elements of $\boldsymbol{\theta}^E$, and the corresponding Bayesian network can be populated and trained. More precisely, given a particular structure subject to an external harmonic load, let $\Delta\omega$ be the range of the excitation frequency ω, sampled at values $\bar{\omega}_s$ ($s = 1, \ldots, N_\omega$) and containing only one resonance condition at ω_p; also, let $(\boldsymbol{\theta}_1^E, \ldots, \boldsymbol{\theta}_{N_d}^E)$ be a N_d-case Design Of Experiments (DOE) on the N_E independent parameters comprising $\boldsymbol{\theta}^E$ (e.g., material properties, geometric quantities and others). For the i-th ($i = 1, \ldots, N_d$) simulated experiment (i.e., a harmonic analysis), the computed sampled measurements $\varepsilon_g(\bar{\omega}_s, \boldsymbol{\theta}_i^E)$ at the sensor location $\mathbf{x}_g$ ($g = 1, \ldots, N_g$) are used as an input to a standard interpolating-spline scheme, herein indicated with the operator $\Upsilon_\omega[.]$. As a result, the entire forced response can be constructed over the entire frequency domain $\Delta\omega$ and the p-th peak frequency $\omega_p(\boldsymbol{\theta}_i^E)$ for the i-th DOE run can be estimated together with

its corresponding response peak amplitude $\varepsilon_g^p(\boldsymbol{\theta}_i^E)$:

$$\varepsilon_g^p(\boldsymbol{\theta}_i^E) = \max_{\omega \in \Delta\omega} \{\Upsilon_\omega \left[\varepsilon_g(\bar{\omega}_s, \boldsymbol{\theta}_i^E)\right]\} \tag{36}$$

Once the resonance conditions are computed for all the N_d cases, such information is utilized to construct other surrogate models, via the interpolation operator $\Upsilon_E[.]$, whose validity is limited to the domain of $\boldsymbol{\theta}^E$ spanned by the design of experiments itself:

$$\varepsilon_g^p(\boldsymbol{\theta}^E) = \Upsilon_E \left[\varepsilon_g^p(\boldsymbol{\theta}_i^E)\right] \tag{37}$$

$$\omega_p(\boldsymbol{\theta}^E) = \Upsilon_E \left[\omega_p(\boldsymbol{\theta}_i^E)\right] \tag{38}$$

where $\omega_p(\boldsymbol{\theta}^E)$ and $\varepsilon_g^p(\boldsymbol{\theta}^E)$ represent, respectively, the functional dependences of the p-th resonance frequency, recorded at the g-th sensor location, and the corresponding peak amplitude of the response being considered (e.g., strain) upon the vector $\boldsymbol{\theta}^E$.

Obviously, in the case of the natural frequencies and the modal quantities $e(\mathbf{x})$ (e.g., modal strains, modal displacements, etc.), no surrogate model is defined in the frequency domain, but only surrogate models in terms of $\boldsymbol{\theta}^E$ are to be established. An example of the aforementioned process is illustrated in Figures 65 and 66, for the cases, respectively, of harmonic and modal strain amplitudes of a plate subject to a base excitation, where results were obtained via a grid-like 25-run design of experiments performed in a domain of $\boldsymbol{\theta}^E = [L, W]$, where L and W are the plate's length and width, respectively. While neural networks were initially considered, surrogate models based on polynomial interpolation have been observed to perform well for the various ranges of excitation frequency being considered. Also, the use of more flexible surrogate models (e.g., neural networks or kriging) was not deemed necessary because if a polynomial meta-model were to strongly underfit the data at a sensor location, this behavior could be interpreted as a warning sign that the use of that sensor data for training a linear Gaussian network could generate a similar underfitting problem, thus hampering the statistical analysis. The size of the design of experiments needs to be adjusted depending on the excitation frequencies being considered and may need to be increased for higher frequency ranges to better capture stronger non-linearities in the vibratory response, even though the obtained accuracy may still not be good enough

115
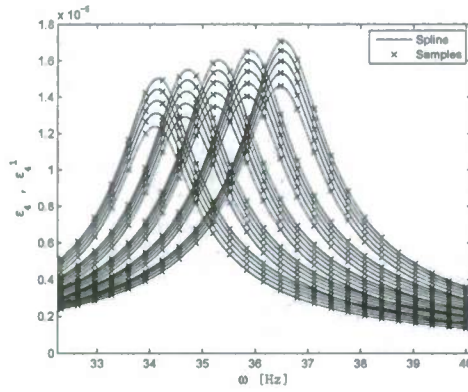
(a) Surrogate models in the frequency domain   (b) Surrogate model in the domain of $\Theta^E = \{L, W\}$
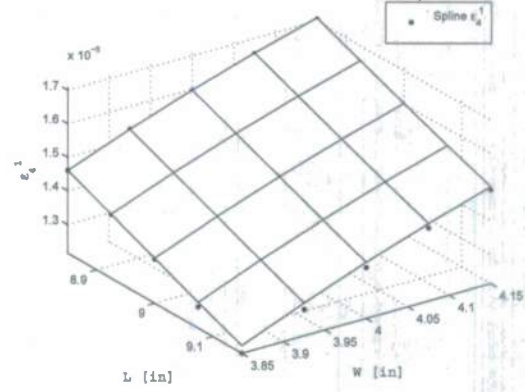
Figure 65: Plate's strain amplitude ε_g at the g-th sensor location ($g = 4$) and near the p-th resonance condition ($p = 1$), computed for $N_d = 25$.

in the presence of strong gradients, as depicted in Figure 66 in the case of the modal strain amplitudes for modes 6 and 8. Besides illustrating the issue of strong gradients, Figure 66 also highlights the appearance of nodal regions within the domain of θ^E for the given sensors. A sensor located in a nodal region usually yields both a low signal-to-noise ratio in the test measurements and numerical noise in the corresponding modal quantities. Therefore, such a sensor should not be modeled within the Bayesian network so as to avoid a loss in accuracy as well as singularities in the response prediction. Also to be excluded from the network are those sensors at whose locations the forced responses and/or the modal quantities of interest exhibit a very low sensitivity with respect to the independent variable θ^E. In fact, under these circumstances, the network training algorithm may not converge entirely because of the presence of nodes with a very small variance, behaving, in essence, as constant quantities rather than as random variables.

Overall, the use of a surrogate model in lieu of direct Monte Carlo simulations provides advantages both at the computational level as well as in terms of gained information, where the amount of error introduced by the interpolating schemes can be reduced by increasing the frequency resolution and/or the size of the design of experiments. In some circumstances, however, the direct-sampling approach may be unavoidable should the vibratory

116

(a) 7-th gauge and 6-th mode   (b) 4-th gauge and 8-th mode
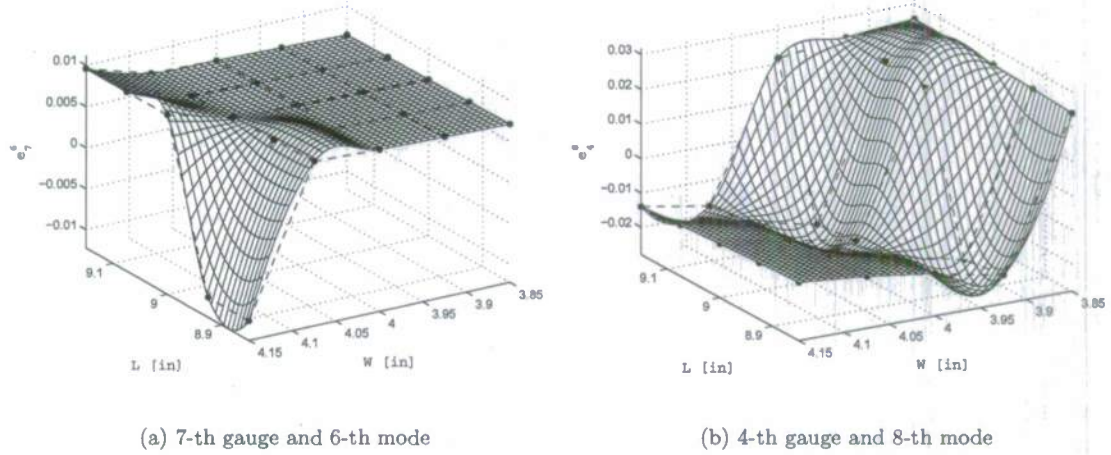
Figure 66: Plate's modal strain amplitudes e_g^n, computed at the g-th sensor location for the n-th mode.

response exhibit a zigzag behavior with respect to the input parameters. That could be the case in the presence of geometric uncertainties whose modeling requires the use of a finite-element mesh that needs to be regenerated at every computational run instead of being scaled up or down. In fact, the consequent variations in the domain discretization become responsible for the introduction of numerical noise which translates into a jittery behavior of the solution, difficult to describe accurately with smooth surrogate models.

5.1.2 Bayesian Network: Topology Selection and Training

According to the inference scheme presented in Section 2.2, four groups of nodes can be herein identified for the n-th resonance and mode: the first group consists of independent quantities included in the set Θ^E and/or Θ^T, and describing the system's properties (e.g., material characteristics or geometric parameters) with respect to which certain uncertainties are parameterized; the second set comprises the "modal nodes" (i.e., the modal ratios $e_{i \neq k}/e_k$ and e_M/e_k, and the natural frequency ω_n) identifying the modal quantities of interest, computed at the sensor locations ($1 \leq i, k \leq N_g$); the third group includes the "harmonic nodes" representing the computed and estimated forced-response quantities (i.e., the true peak amplitude ε_k at the reference sensor k, the estimates $\varepsilon_{i \neq k}^*$ at the other

117
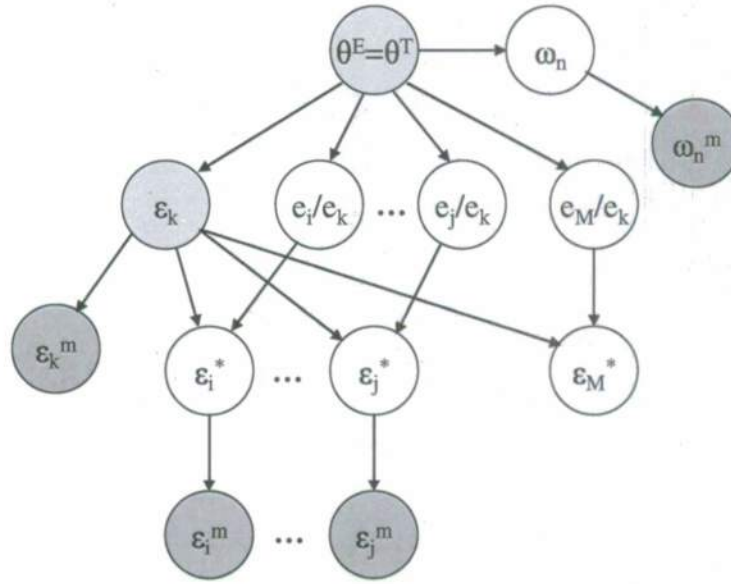
Figure 67: Bayesian network topology T_1.

locations, and the maximum-response estimate ε_M^*); and finally, the fourth set encompasses the "measurement nodes" (i.e., the sensor measurements ε_k^m, $\varepsilon_{i \neq k}^m$ at the recorded peak frequency ω_n^m), which consists of the actual outputs from the measuring devices. In order to find the most suitable way to model the uncertainty in the response prediction scheme, various network structures were taken into consideration, with a focus mainly on the three topologies, T_1, T_2 and T_3, illustrated in Figures 67-69. Despite looking somewhat similar to one another, these three network structures do differ significantly from a conceptual standpoint.

Network topology T_1 is based on the assumption that $\Theta^E = \Theta^T$, which implies that all the factors responsible for the observed uncertainties are fully observable and could be modeled. This hypothesis is not entirely realistic, especially for complex systems and experimental setups, where a myriad of unobservable sources of uncertainties is present. Furthermore, such a net cannot account for the poor correlation Ξ between the physical system (or forced-/-response test data) and the analytical model (or mode shapes). Besides measurement errors, any unsatisfactory correlation (and consequent response variability)
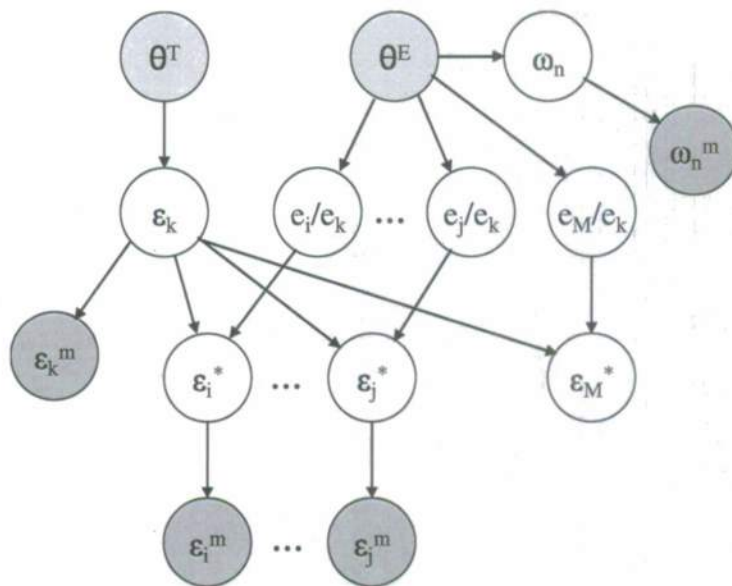
Figure 68: Bayesian network topology T_2.

between the physical system's true state and its system model's nominal state may represent an important contributor to uncertainty. Such a scenario, however, cannot be modeled explicitly with topology T_1 because harmonic and modal nodes share the same set of root nodes. An artificial stratagem would be to calculate each element of Ξ using a modal ratio associated with a realization of the quantities comprising the set Θ^E different from the one used to obtain the simulated forced response. Such an expedient, however, destroys the cause-effect relationships linking ε_j and e_i/e_j to ε_i^* $(i \neq j)$, thus causing the Bayesian network to perform extremely poorly in terms of evidence propagation.

Network topology T_2 no longer contains the hypothesis $\Theta^E = \Theta^T$. This gives the freedom to choose Θ^E to be equal to Θ^T, or just be a subset of it based, for instance, on given design criteria (e.g., network complexity). The explicit modeling of the elements of Θ^T within the network implies, however, that a complete knowledge is available about the factors responsible for the variability and uncertainty present in the data. In practical applications, however, this knowledge may not be accessible. The distinction between Θ^E and Θ^T allows to account easily for those cases of poor correlation between a physical system

and its model, even in the event that the two sets contain the same input parameters, thanks to the fact that two different sample populations for each parameter can be used to populate the harmonic and the modal nodes. Nevertheless, a clear drawback to this approach is represented by the inability of the network to have the two sets of input-parameter root nodes, Θ^E and Θ^T, converge to the same mean values upon the introduction of evidence. This behavior is due primarily to the error introduced by the modeling, through linear arcs, of the various non-linear cause-effect relationships between the nodes. In fact, if evidence is introduced, for instance, at node ε_i^* and propagated backwards to Θ^E and Θ^T, the different levels of error introduced by the linear approximation along the two distinct paths of links become responsible for the observed discrepancy between Θ^E and Θ^T. In order to resolve this difference, due to model underfitting, an off-line update procedure would be necessary to have both sets of root nodes converge to one set of values. An alternative could be to employ the root nodes characterized by a lower posterior variance as reference for their counterparts and infuse their posterior information as additional evidence. A possible issue would, then, be that the Bayesian network might become over-constrained with consequent forced steering of its statistical parameters.

Finally, illustrated in Figure 69 is the network structure T_3 which has been developed and adopted to model the response prediction scheme under uncertainty. The proposed topology is able to address the aforementioned issues in the following manner:

- Regardless of the parameters actually employed to generate the scatter in the simulated measurements, such variability can be ascribed to other factors as well, since none of the former ones is explicitly modeled in the network. This is in agreement with the idea of simulated experiments not being a duplicate of reality, but an equivalent representation of it;

- Measurement uncertainty and errors associated with the matching of the actual structure with a nominal model are consistently accounted for; and

- No hypothesis is necessary when constructing the network in terms of the completeness of the knowledge at hand. Of course, the more information is available, the more
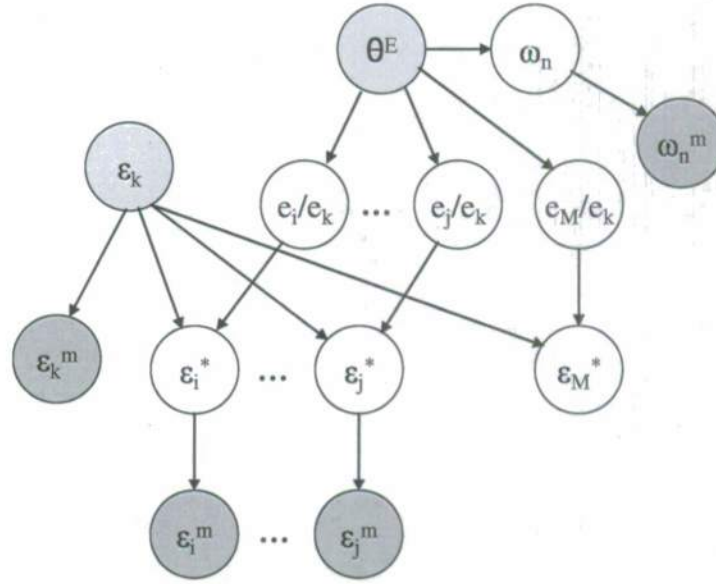
Figure 69: Bayesian network topology T_3.

educated the selection of the root nodes included in the set Θ^E can be, and the better
the uncertainty can be quantified and reduced through evidence infusion.

Once the structure of the network is fixed, the next step is to populate its elements.
Training data can be divided into two types: the first type includes the sample data obtained
from the simulated modal and forced-response analyses, and used to establish the links
among the root, the modal and the harmonic nodes; the second type contains the data
that directly relates to the uncertainty embedded within the experimental measurements,
which is responsible for how given computed nodes are connected to their measurement--
node counterparts. On the one hand, the uncertainty propagated through the simulated
experiments can be assigned based on the available expertise, or arbitrarily in the presence
of limited knowledge (e.g., unknown tolerances associated with a particular manufacturing
process), as long as the simulated response is comparable with the measured response in a
statistical sense. On the other hand, the training data necessary to connect the measurement
nodes to the rest of the network is a function of the error η associated with the particular
instrumentation in use. According to the network's underlying assumption of Gaussian

nodes, the measurement error η is also assumed to be normally distributed; hence, the following relationships are established for each physical quantity:

$$
\begin{aligned}
\varepsilon_k^m \quad &= \varepsilon_k + A_\varepsilon\, \eta_\varepsilon \\
\varepsilon_i^m \quad &= \varepsilon_i^* + A_\varepsilon\, \eta_\varepsilon \quad (i \neq k) \\
\omega_n^m \quad &= \omega_n + A_\omega\, \eta_\omega \\
\text{where} \quad \eta_\varepsilon &\sim N(0, \sigma_\varepsilon) \\
\eta_\omega &\sim N(0, \sigma_\omega)
\end{aligned}
\tag{39}
$$

The non-dimensional standard deviations σ_ε and σ_ω characterize, respectively, the variability in peak amplitude and peak frequency, while measurement accuracy is expressed in terms of the factors A_ε and A_ω whose values are chosen based on the scatter in the physical quantities due to uncertainty at the root-node level. In the ideal case of infinite accuracy (zero σ's), the measurement nodes are a mere image of their counterparts and their links carry no additional statistical information; on the other hand, the higher the measurement errors present in the training data are (non-zero σ's), the more experimental uncertainty can be modeled in the network until a limit is reached at which the physical quantities and their measurements are no longer correlated, and their links actually destabilize the network.

In order to assess the network's ability to properly update itself upon evidence infusion, each node's supposedly known true value is compared against the mean value of its posterior probability function. For a given true state $\left[\bar{\Theta}^E, \bar{e}_{i \neq k}/\bar{e}_k, \bar{e}_M/\bar{e}_k, \bar{\varepsilon}_k, \bar{\varepsilon}_{i \neq k}^*, \bar{\varepsilon}_M^*, \bar{\varepsilon}_k^m, \bar{\varepsilon}_{i \neq k}^m, \bar{\omega}_n, \bar{\omega}_n^m\right]$ of the network and a specific evidence scenario (i.e., a subset of observed nodes), a metric δ has been adopted to evaluate how well the posterior mean μ of a queried node agrees with its assumed true state. For instance, for node ε_k and its true-state realization $\bar{\varepsilon}_k$, δ is defined as follows:

$$
\delta = 100 \times \frac{\mu\left(\varepsilon_k\right) - \bar{\varepsilon}_k}{\Delta \varepsilon_k}
\tag{40}
$$

where $\Delta \varepsilon_k$ is the node's range of variability observed in the set of data used for validation. As done for ε_k, the percentage relative error δ can also be defined for all the other queried nodes in the network, while it defaults to a value of zero for the observed nodes. Moreover,

given a sample population of states, mean, standard deviation, and confidence intervals for each nodal δ can be obtained for any evidence scenario and can be used to assess the goodness of network updating in a statistical sense. Since only the measurement nodes are observable in an experiment, complete states for the network can only be computed by means of simulation, but their use in the computation of δ still provides valuable information in terms of the accuracy to be expected from the network when tracking the nodes' states associated with actual experimental observations.

In the following sections, the proposed methodology and its performance in quantifying uncertainty are investigated for two vibration problems regarding a one-dimensional beam and a three-dimensional plate structure. It is to be noted that the response ε considered for the beam structure consists of the axial stress, with results to be interpreted in SI units; on the other hand, strains were computed for the plate whose geometric parameters were expressed in British units, namely inches. Moreover, the notation introduced in equation (28) has been further simplified by removing the indices referring to the peak number and the sensor used as reference for the estimation process.

5.2 One-dimensional Problem: Beam Structure

Analyses on the response inference technique and its Bayesian-network implementation have been conducted at first on a one-dimensional fixed-free beam structure subject to a base excitation with frequency sweeping across the second natural frequency. In these simulated experiments, the vibratory response of the structure, in the form of axial stresses, was recorded at nine locations along the span, with sensor g placed at a distance of $0.1\,g\,L_o$ ($g = 1, \ldots, 9$) from the fixed end of the beam, the nominal length of which is $L_o = 1\,\mathrm{m}$.

Contrary to the topology shown in Figure 69, modal ratios could not be modeled explicitly within the network because of their invariance with respect to certain input parameters, as that would lead to the modeling of deterministic nodes. Hence, the modal stress at each sensor location was treated as a separate node. As a result, any modeled difference between the actual system and its nominal analytical representation was also, *de facto*, absent within the network and had no impact on the statistical results.

Presented next are two cases constructed assuming input-parameter uncertainties on geometry, material properties, and measurements. In these and all the other case studies, the Bayesian network has been trained using at least 3000 samples per node, and it has been validated utilizing 1000 simulated true states of the structure being considered.

5.2.1 Uncertainty in Geometry

The case of uncertainty in the beam's length L and thickness T is illustrated in Figures 70 and 71 for a two-gauge network with no measurement nodes. Shown in the figures is the network's performance in predicting a single true state and reducing the corresponding variability in the case of observations introduced, in sequence, at nodes ε_3, ε_9^*, and ω_2. Any single one of the first two pieces of evidence is sufficient to update the maximum-response $\mu(\varepsilon_M^*)$ to its correct value, even though both of them have no effect on the root and modal nodes, which are, instead, updated only after the information on the natural frequency ω_2 is added. Unless the zero-evidence state of the network is close to the true state of the system, the update is consistently inaccurate for the root nodes because there are infinitely many combinations of length $\mu(L)$ and width $\mu(T)$ which can yield the given measured frequency. As a result, the modal stresses also do not converge to their true values, even though their update does not destroy the intrinsic relationship between a forced-response ratio, at a point on the structure, and its corresponding modal ratio. Such a behavior does not constitute a limitation of the Bayesian network *per se*, but simply a consequence of the information about the true state being insufficient and/or redundant. In fact, in conjunction with the mode shape being known short of a scaling factor, additional degrees of freedom emerge due to the modal ratios being constant with respect to L and T, a phenomenon which will unlikely be as important in realistic situations. As illustrated in Figure 72, the inclusion of two additional sensor nodes within the network does not yield any improvement in terms of convergence for the root and modal quantities (i.e., natural frequency and modal stresses). In fact, their percentage relative error δ does not vary significantly as evidence is sequentially added at the measurement nodes, whereas the uncertainty associated with the maximum-response estimate decreases steadily.

124
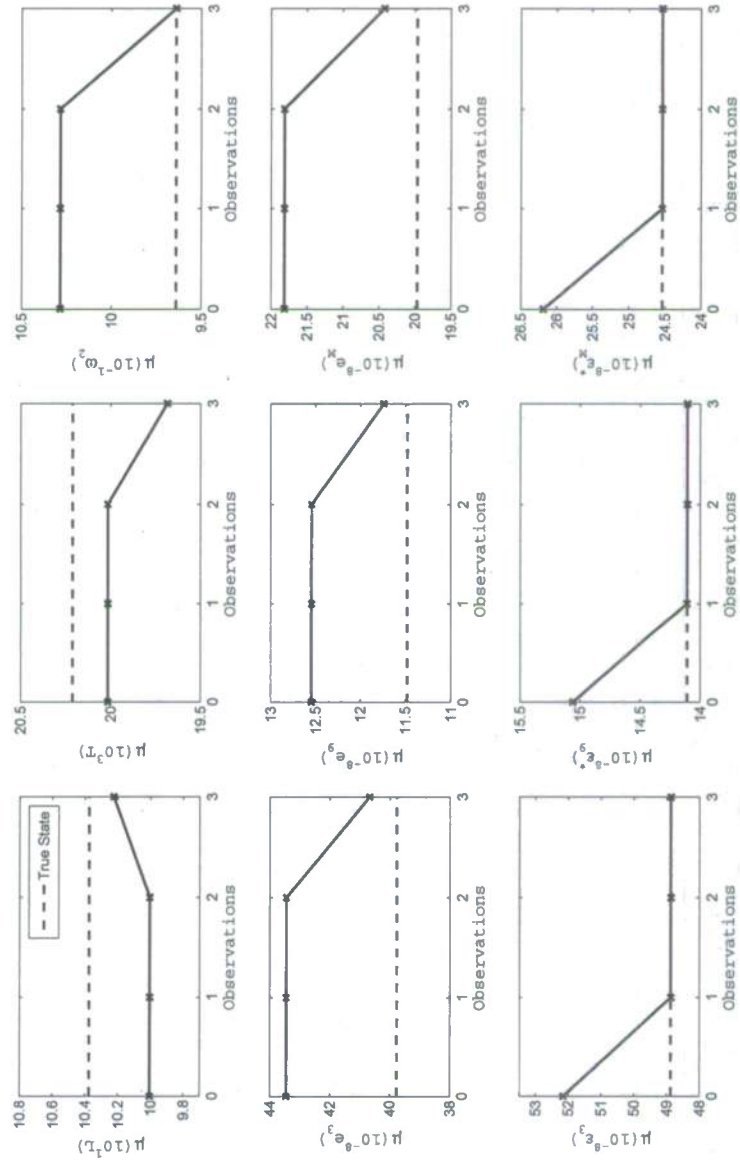
Figure 70: Beam structure: comparison between true and expected state of a two-gauge Bayesian network in the presence of geometric uncertainty in L and T.
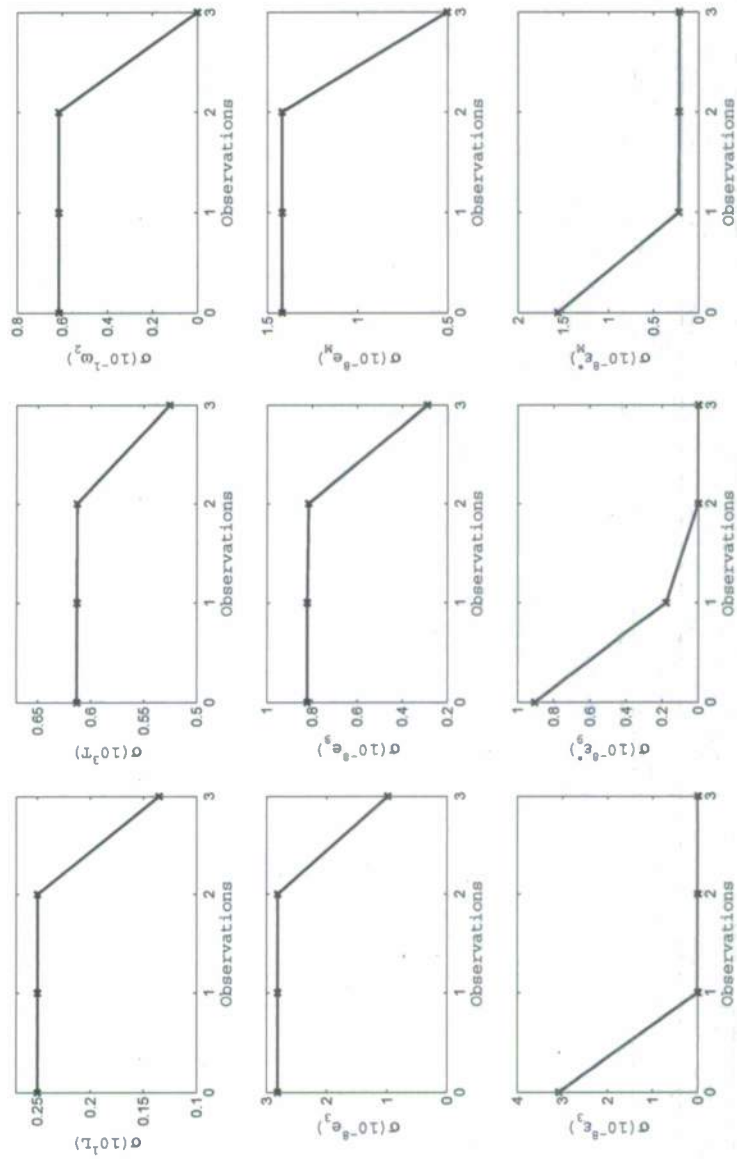
Figure 71: Beam structure: standard deviations at the nodes of a two-gauge Bayesian network in the presence of geometric uncertainty in L and T.

126
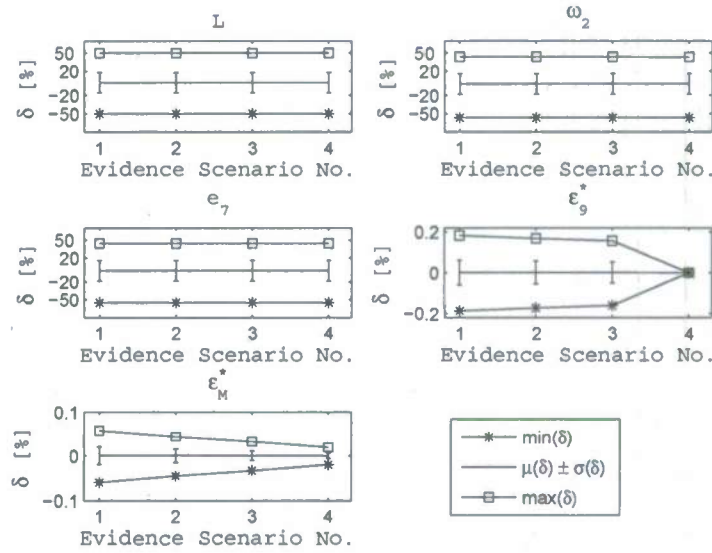
Figure 72: Beam structure: prediction error δ in the presence of geometric uncertainty in L and T, for a four-gauge Bayesian network.

5.2.2 Material Properties Uncertainties

Uncertainties in Young's modulus E and damping ratio ξ have also been considered with standard deviations equal to 3% and 10% of their nominal values 114 GPa and 0.02, respectively. As in the previous analysis, this scenario has first been modeled via the same two-sensor network topology, whose dichotomy between harmonic and root/modal nodes still exists. Since the prediction of the system's response is performed via undamped mode shapes, the damping ratio's variability only affects the accuracy with which the forced–response is known, while the $\xi - \omega_2$ arc is unable to transfer any information. This results in the incapacity of the Bayesian network to update the prior distribution of ξ and reduce its inherent uncertainty. As in the case of geometric uncertainty, evidence on any of the sensor nodes is sufficient to properly predict the maximum axial stress, while the rest of the network is insensitive to the inclusion of this information. Knowledge on the frequency node is, therefore, necessary to update the remaining nodes, except for ξ. Once again, the update does not lead to an absolute convergence, even though the updated modal stresses yield

127

modal ratios that are consistent with the corresponding ratios from the forced response. The $\pm 1\sigma$ interval for the relative error on Young's modulus and modal stresses shrinks from $\pm 15\%$ to $\pm 5\%$ when ω_2 is updated with the additional evidence. Because of the small prior variance $\sigma(E)$, the worst conditions occur when the evidence on ω_2 corresponds to a value of E which disagrees strongly with its prior probability distribution so that the evidence is given less importance due to a high belief in the prior information itself. Besides this phenomenon, the linear approximation describing the non-linear relationship between Young's modulus and natural frequencies also contributes to the mismatch between true state and posterior mean values of the root nodes. This error consequently propagates down to the modal stresses as well.

Prediction accuracy does not improve when more sensors are included in the network, as shown in Figure 73. In fact, the addition of two other sensors only adds in topological complexity as the maximum stress is already estimated as precisely as possible with one gauge. The error δ of the modal and root nodes also remains unaffected until ω_2 is updated in the fifth evidence scenario.

The introduction of measurement errors causes the network to fail in successfully pinpointing the true maximum stress with just one measurement. In contrast to the above cases, an increase in the number of sensor measurements being infused into the network becomes advantageous in this circumstance, as it steadily decreases the discrepancy between predicted and true response. As depicted in Figure 74, the increasing number of sensors only affects the harmonic nodes, whereas the uncertainty associated with the posterior probabilities at the modal and root nodes is exclusively dependent upon a measurement of the peak frequency being as accurate as possible.

Overall, the particular nature of the beam structure reveals an interesting behavior of the Bayesian prediction scheme, where harmonic and modal nodes do not exchange knowledge with one another, thus forming two practically decoupled sub-nets, with the former being predicted with satisfactory accuracy and the latter unable to converge. Despite that, modal ratios are preserved and in consistent agreement with their forced-response counterparts when frequency and amplitude evidence are accounted for. Furthermore, the network

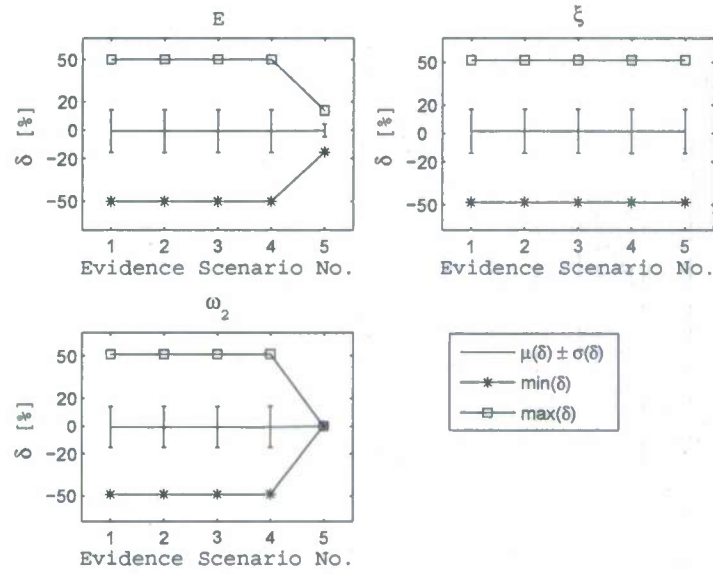**Figure 73:** Beam structure: response prediction in the presence of uncertainty in E and ξ, for a four-gauge Bayesian network.
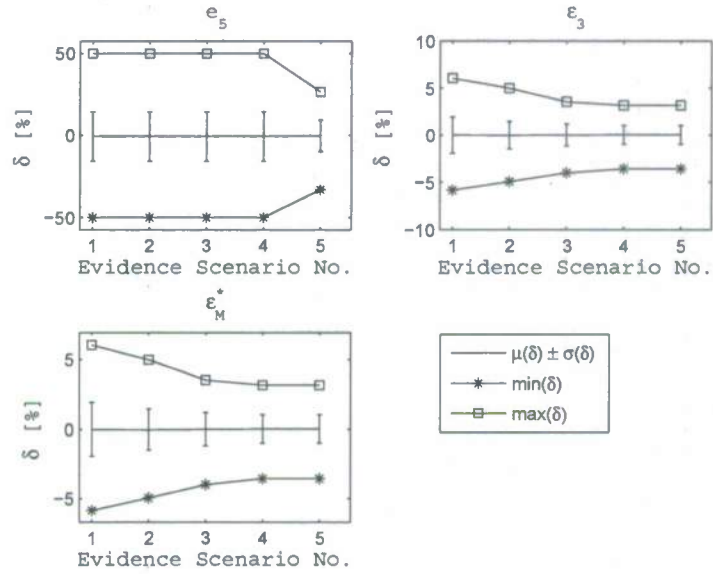
Figure 74: Beam structure: response prediction in the presence of measurement errors and uncertainty in E and ξ, for a four-gauge Bayesian network.

structure has demonstrated the ability to capture and model satisfactorily non-contributing nodes (i.e., ξ) without exhibiting additional insensitivity to evidence infusion.

5.3 Three-dimensional Problem: Plate Structure

To extend the analysis to the three-dimensional case, the same plate structure of Chapter 3 has been considered, instrumented with eleven strain gauges and subject to a base excitation. In this case, the system's response being tracked is in the form of surface strains, evaluated along the sensor measurement direction, while the Von Mises equivalent maximum strain represents the target quantity to be predicted. Errors associated with test measurements, uncertainty in model parameters, as well as the discrepancy in the correlation between the physical system and its model are all modeled within the network.

As a representative example, geometric uncertainty has been considered in the form of harmonic thickness variations along the plate's length L and width W. These particular parameters were utilized because they provide higher sensitivity for the vibratory response of the plate structure as compared to other sources of uncertainty. In a reference frame with z-axis perpendicular to the plate's main surfaces and origin coincident with one of its vertices, the following thickness tolerances, Δz_u and Δz_l, were assigned, respectively, on the top and bottom surface:

$$\Delta z_u(x,y) = +\frac{t_L}{2} \sin\left(2\pi\frac{y}{L}\right) + \frac{t_W}{2} \sin\left(2\pi\frac{x}{W}\right) \tag{41}$$
$$\Delta z_l(x,y) = -\frac{t_L}{2} \sin\left(2\pi\frac{y}{L}\right) - \frac{t_W}{2} \sin\left(2\pi\frac{x}{W}\right)$$

where t_L and t_W represent two Gaussian random variables with zero mean and standard deviations equal to 5% of the thickness nominal value 0.125 inches.

In the first set of results, a four-gauge network was considered in which t_L was assumed to be the only source of uncertainty together with non-matching correlation between model and physical component. Hence, in the absence of measurement errors, the true-strain and predicted-strain nodes are effectively connected to their corresponding measured-strain nodes by means of equality links. This setup allows to investigate the effect that the linear-link approximation has upon the network's ability to close in onto the system's true state as a function of evidence. Shown in Figures 75-77 is the dependence of the modal ratios upon

130

t_L for the chosen sensors, where essentially only one arc is non-linear. Despite the attempt at reducing non-linearities by selecting, when possible, sensors at which the response exhibits shallow non-linear trends, the major source of non-linearity is embedded in the estimation process itself via the product of modal ratios and measurements.

The performance of the network with respect to evidence at the measurement nodes is illustrated in Figures 78 and 79. In contrast to the desired behavior of the model, the error δ does not steadily decrease for all nodes with more evidence being infused into the network. Such a behavior is the result of fitting non-linear data into a linearized model, basically an evidence-induced stiffening effect. As a consequence of this model underfitting, as more observations are added, the network loses some of its degrees of freedom, and it becomes incapable of explaining the new evidence, hence the rising of non-monotonic trends due to apparent conflicting information. Illustrated in Figures 80 and 81 is the case in which evidence at the frequency node is included as the last observation. As for the beam structure, the frequency-measurement node influences primarily the modal nodes, while the forced–response ones are affected mostly by the amplitude-measurement nodes. No significant inconsistency arises from its addition, unless the $\pm 1\sigma$ interval for a specific node is already quite tight within a few percentage points. In the presence of measurement errors in the training data (Figure 82) and the observations, the network becomes more flexible with respect to evidence inclusion and, once again, an increasing number of sensors/observations becomes beneficial in reducing the extra variability and consistently lowering the relative error δ, especially for the harmonic nodes (Figures 83 and 84).

Another set of results is presented for the 20-node Bayesian network comprising t_L and t_W as root nodes together with five strain gauges. As indicated by Figures 85 and 86, in spite of the non-linearities affecting its links, the network performs satisfactorily as the discrepancy δ decreases with the infusion of more and more measurements. It is important to note that for the network to capture and properly quantify uncertainty, the error introduced by the linear approximation has to be lower than the one associated with other sources of variability. If a very low correlation between training data and linear models occurs, this results in meaningless cause-effect relationships being established among the

nodes, and consequent poor performance of the network. In order to obviate this issue, a transformation can be used where harmonic and modal nodes are replaced with their logarithms. On the one hand, the transformation eliminates the non-linearities associated with the computation of ε_j^* $(j = 1, 2, \ldots)$ as well as the dependence of the corresponding links upon the training data. On the other hand, however, such a transformation invalidates even more the assumption of Gaussian nodes and is itself non-linear. Depicted in Figure 87, the errors on the maximum strain are compared for two Bayesian networks, with and without logarithmic transformation, for the same training data and evidence scenarios. Clearly, in this case, no approach is strongly outperforming the other, but the use of the logarithm transformation (or other suitable ones) could be strongly beneficial in the presence of large non-linearities in the training data to be treated with linear models. Moreover, the comparison of δ's can be employed to assess the error introduced by the linearized prediction scheme against the transformation-induced non-linearities.
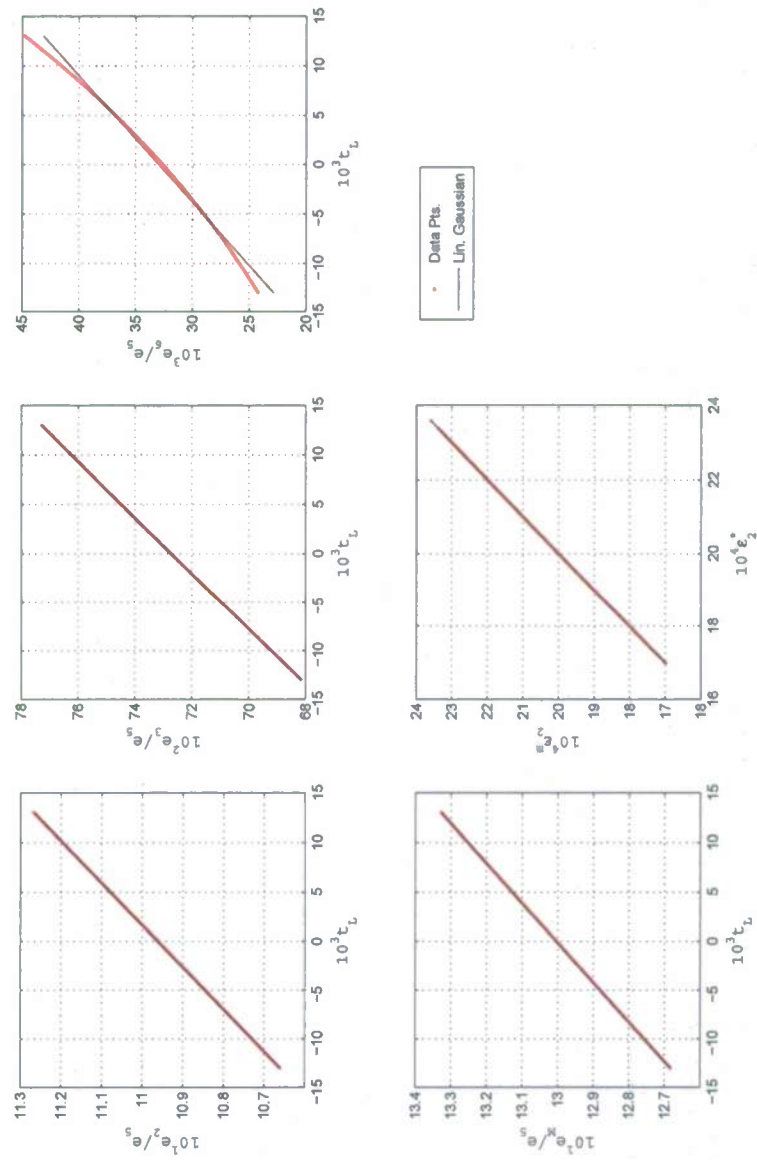
Figure 75: Plate structure: data for network training and linear approximation.

133
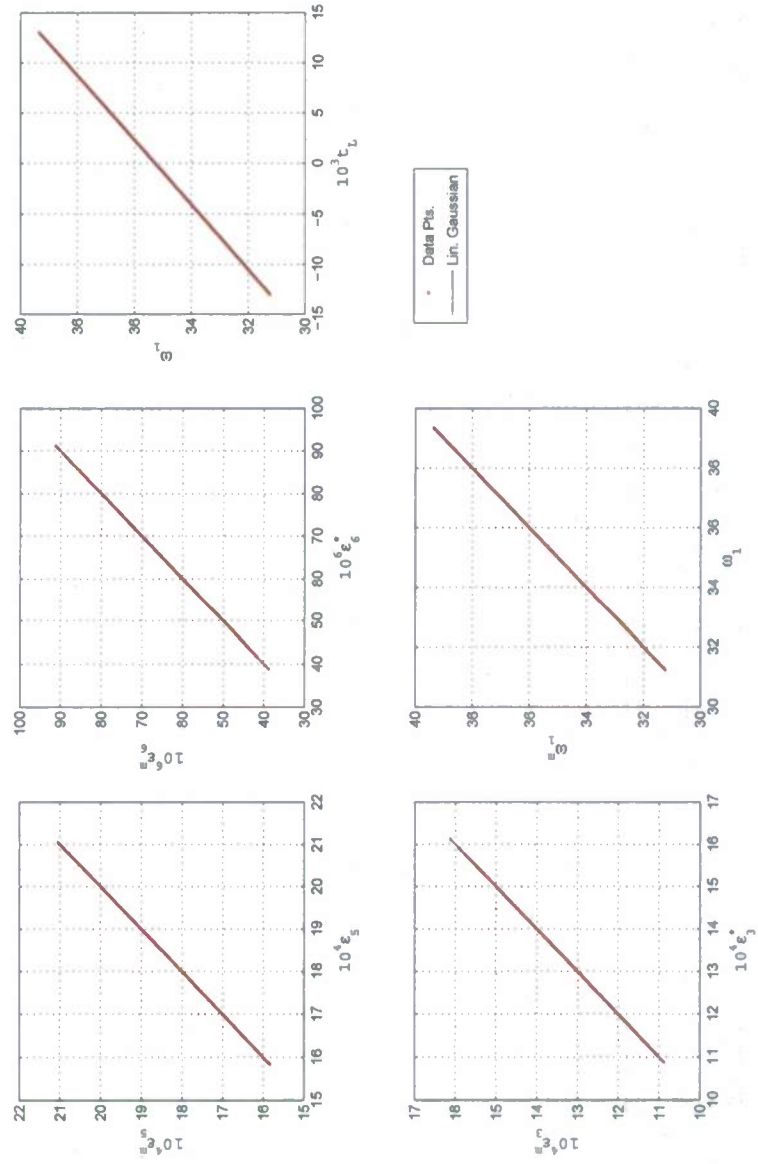
Figure 76: Plate structure: data for network training and linear approximation.

Figure 77: Plate structure: data for network training and linear approximation.

Figure 78: Plate structure: prediction error in the presence of uncertainty in t_L and no measurement errors, with evidence only at the amplitude measurement nodes of a four-gauge Bayesian network.
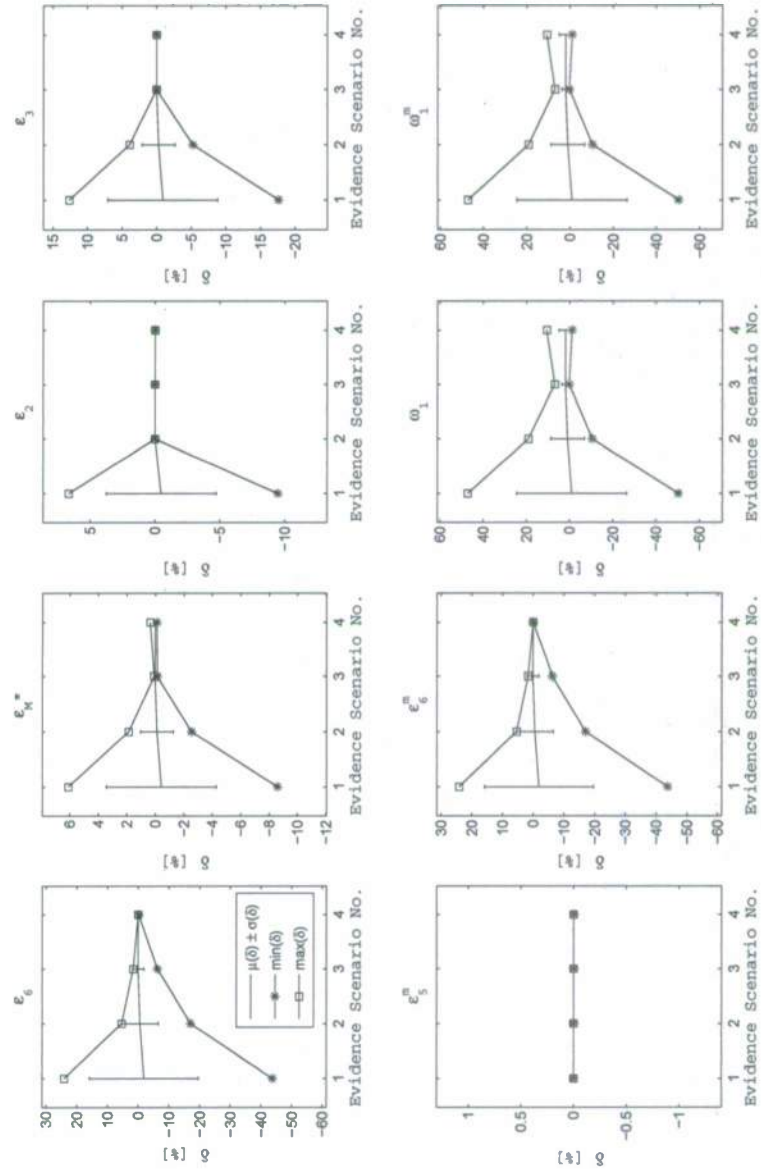
Figure 79: Plate structure: prediction error in the presence of uncertainty in t_L and no measurement errors, with evidence only at the amplitude measurement nodes of a four--gauge Bayesian network.
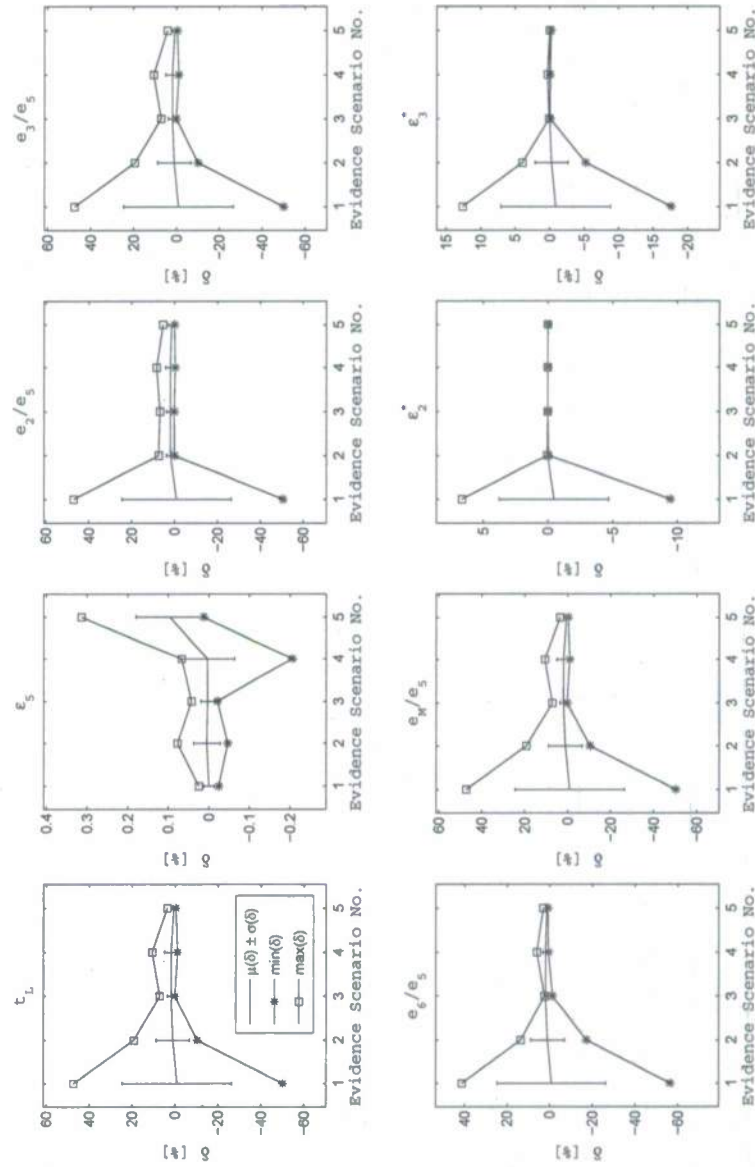
Figure 80: Plate structure: prediction error in the presence of uncertainty in t_L and no measurement errors, with evidence at the amplitude and frequency measurement nodes of a four-gauge Bayesian network.
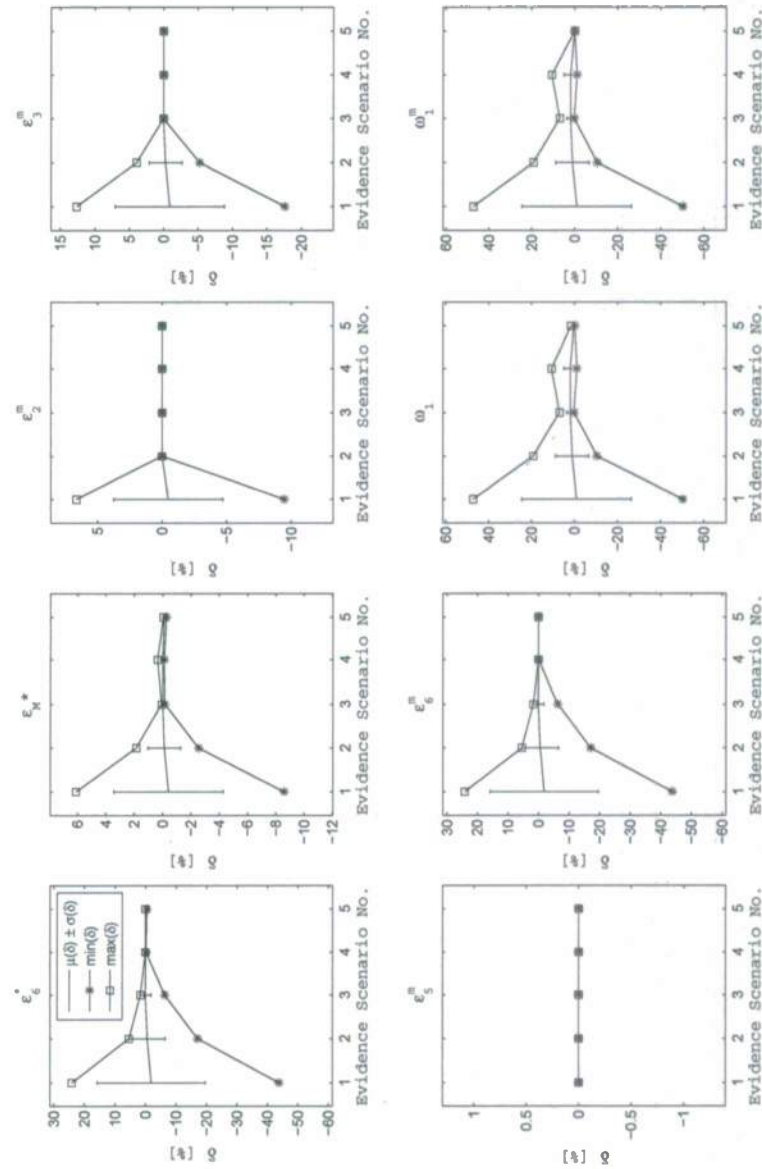
Figure 81: Plate structure: prediction error in the presence of uncertainty in t_L and no measurement errors, with evidence at the amplitude and frequency measurement nodes of a four-gauge Bayesian network.
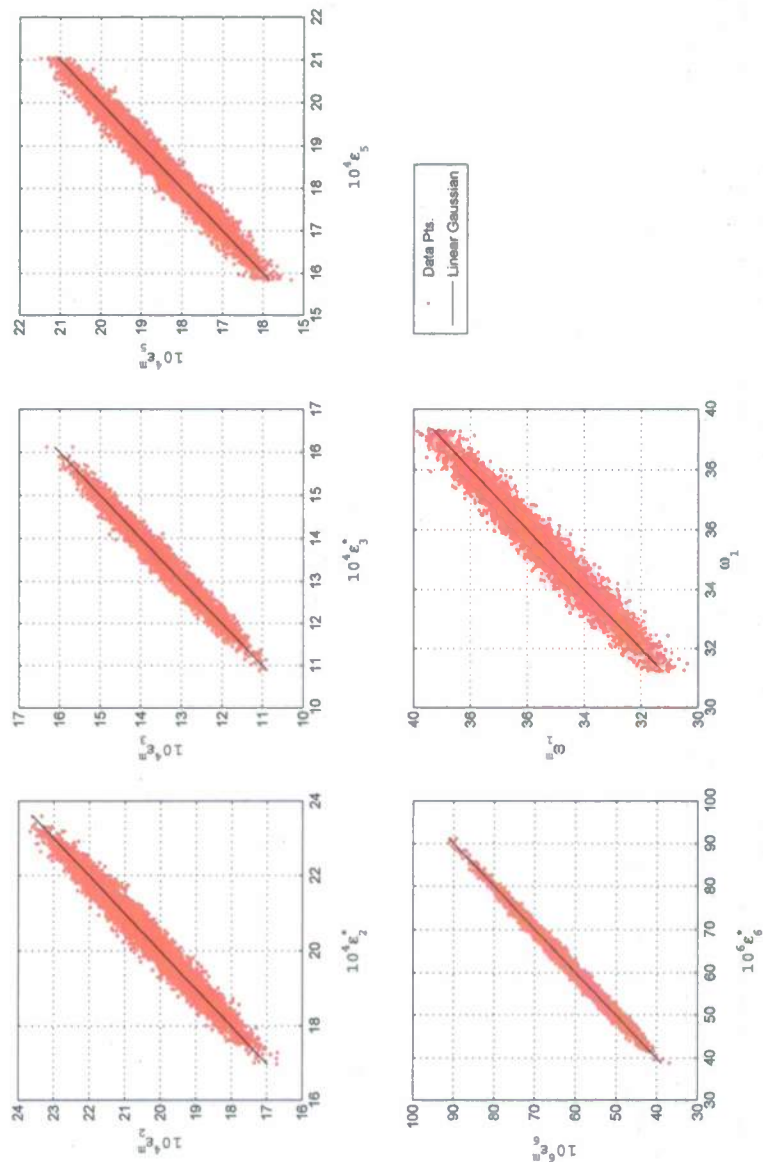
Figure 82: Plate structure: measurement errors included in the training data.
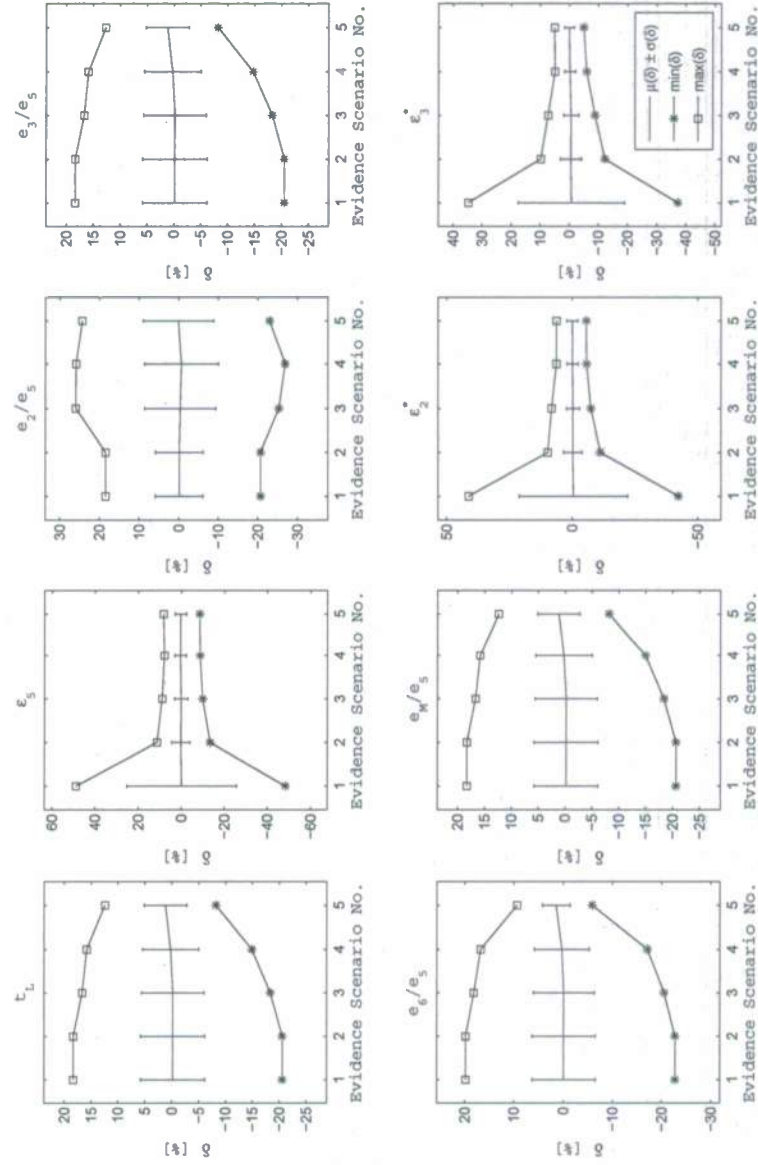
Figure 83: Plate structure: prediction error in the presence of uncertainty in t_L and measurement errors, with evidence at the amplitude and frequency measurement nodes of a four-gauge Bayesian network.

141
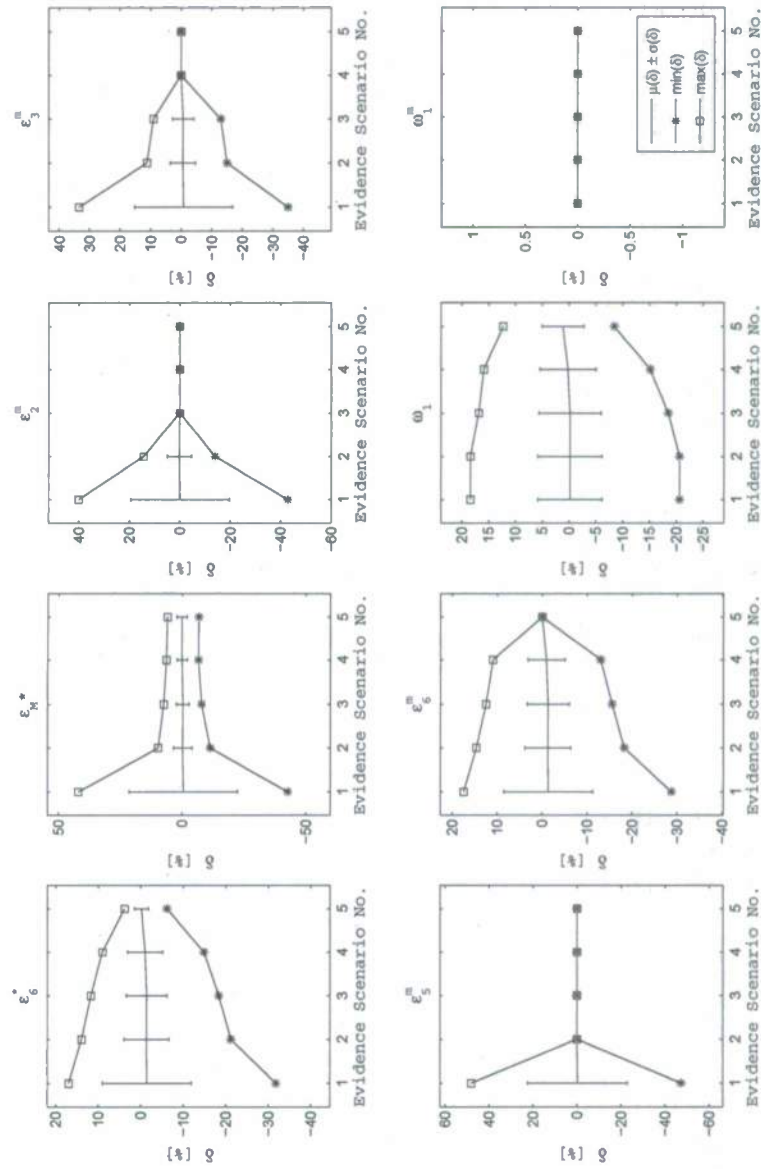
Figure 84: Plate structure: prediction error in the presence of uncertainty in t_L and measurement errors, with evidence at the amplitude and frequency measurement nodes of a four-gauge Bayesian network.
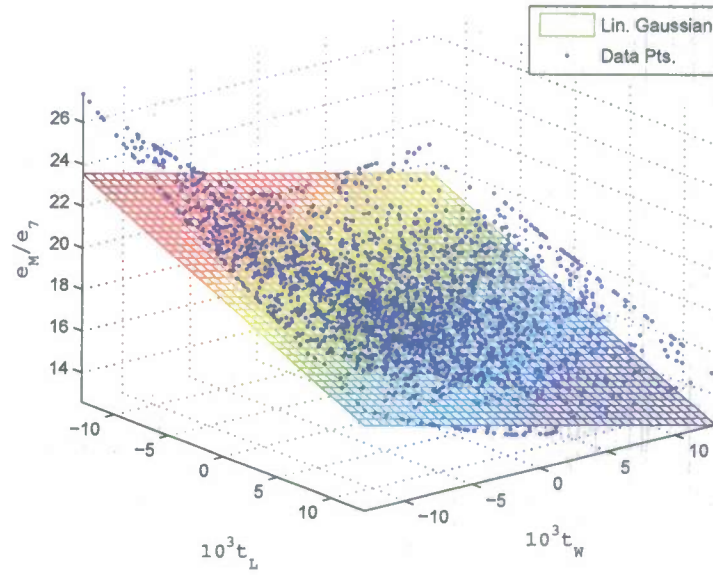
(a) Linearized causal relationship for e_M/e_7
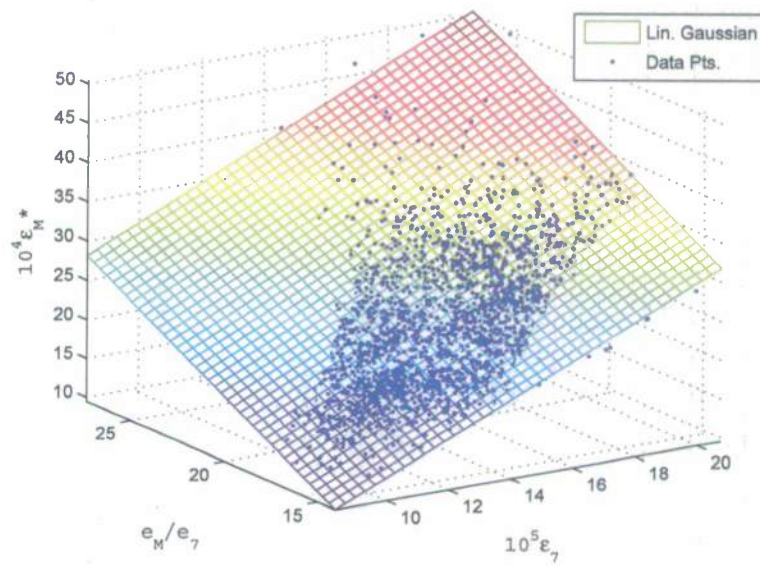
(b) Linearized causal relationship for ε_M^*
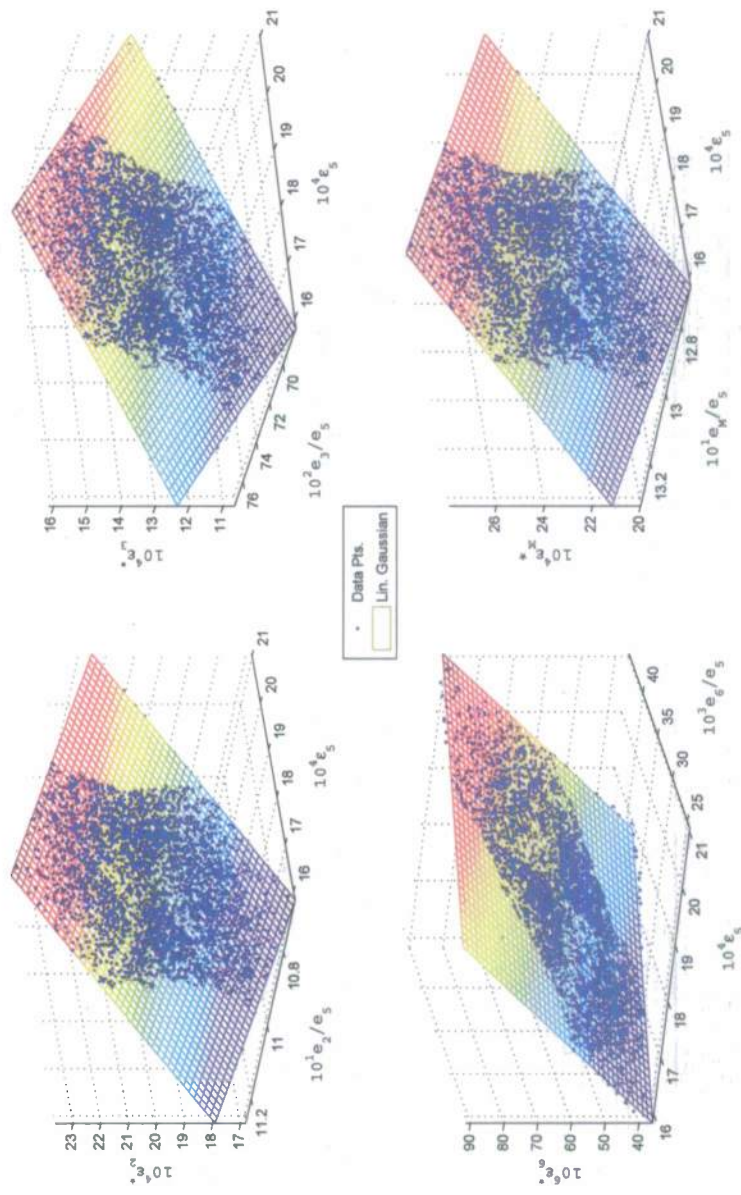
Figure 85: Plate structure: data for network training and linear approximations.
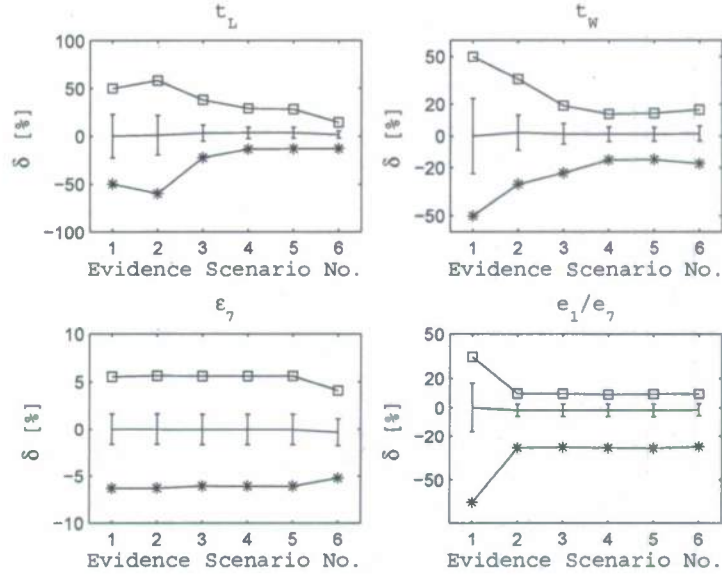
(a)
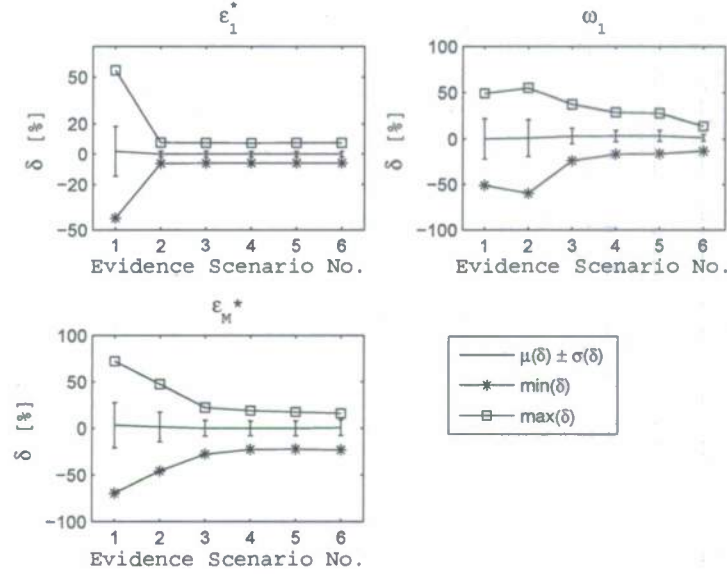
(b)

Figure 86: Plate structure: prediction error in the presence of uncertainty in t_L, t_W and the measurements, with evidence at the amplitude and frequency measurement nodes of a five-gauge Bayesian network.
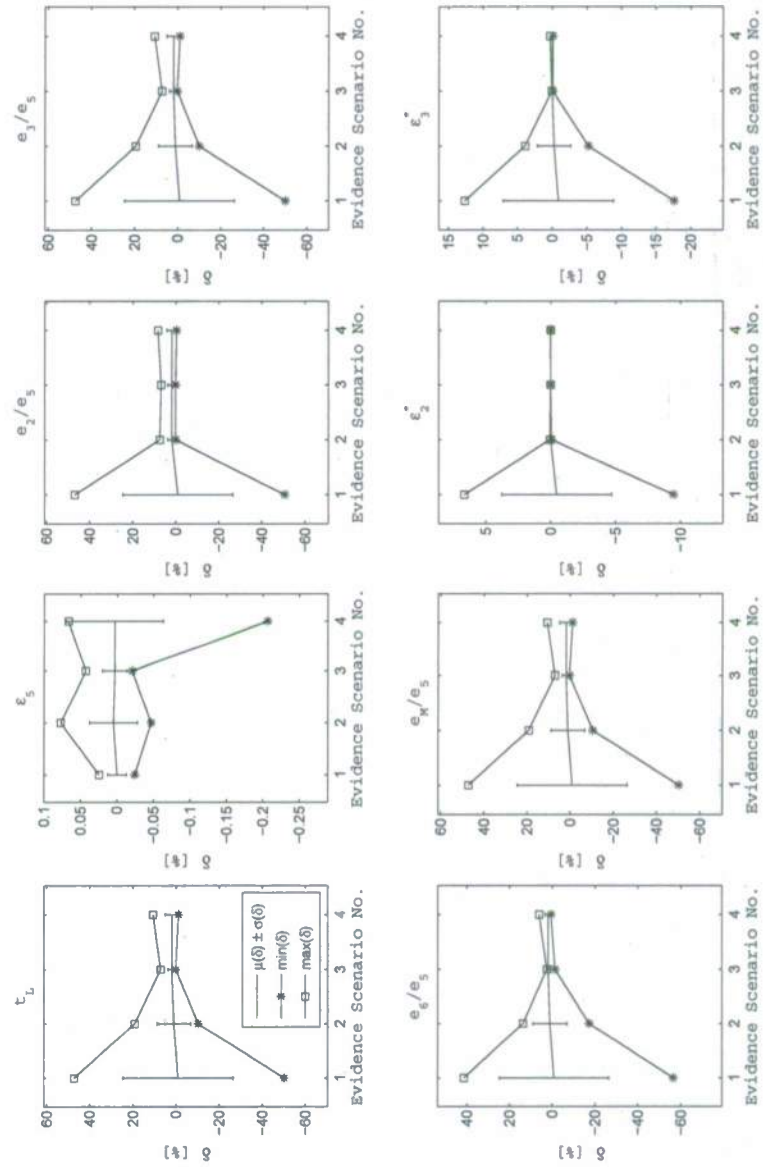
144
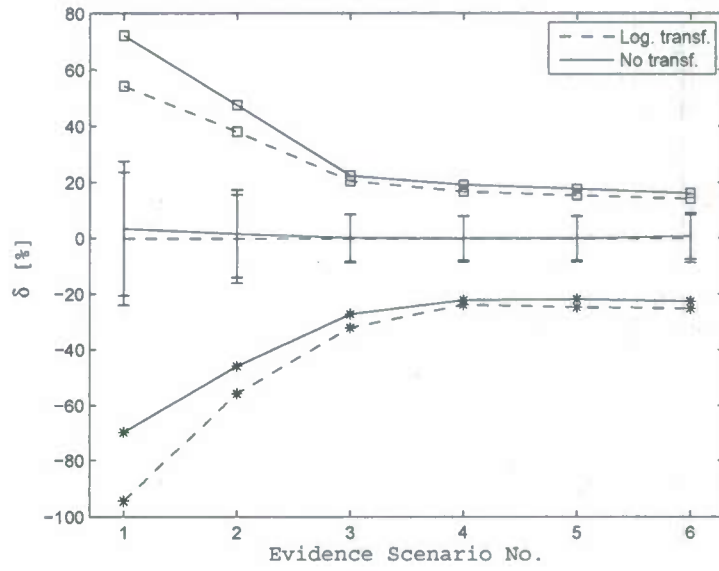
Figure 87: Plate structure: prediction error in the presence of uncertainty in t_L, t_w and the measurements, with evidence at the amplitude and frequency measurement nodes of a five-gauge Bayesian network.

5.4 Discrete-node Bayesian Networks

The results presented thus far were obtained using a Bayesian network comprised of continuous nodes and based upon the following assumptions:

- All the nodes are Gaussian variables;

- A node's Conditional Probability Distribution (CPD), describing the statistical dependency from its parent nodes, is a normal distribution whose mean is a linear function of the mean values of the parent nodes, and whose variance is fixed.

Gaussian nodes were chosen because their use leads to a closed-form solution of the marginal probability integrals and requires a lower computational cost as compared to utilizing other probability functions to describe the network nodes. Furthermore, other methods in the literature have also been successfully developed under the same assumption [29, 30, 107], thanks to the possibility of transforming, when desired, a set of non-normal random variables into an equivalent set of Gaussian ones via the Rosenblatt or the Nataf transformation

[67].

Despite the fact that these assumptions are never met (e.g., for the prediction nodes alone, each $\varepsilon^*_{j \neq k}$ is not a linear combination of its parents and its distribution fails to be Gaussian even if its parents were normally distributed), the previous results showed a satisfactory performance of the Bayesian inference scheme as long as the node-to-node links were not weakened by large approximation error due to excessive non-linearities. Any significant non-Gaussian nature of the training data, instead, has not been taken into consideration in the previous analyses as it was neglected within the training procedure. In fact, the expectation-maximization learning algorithm in use within the BNT Gaussian toolbox trains the network by matching the first two moments (mean and standard deviation) of each node with the corresponding moments of the sample populations, regardless of their higher moments, which may still be statistically significant. Therefore, in order to assess further the impact of the aforementioned assumptions upon the validity of the results, the use of a discrete-node Bayesian network was also investigated for comparison purposes.

Discrete-node Bayesian networks have both advantages and limitations. On the one hand, the discrete-node approach can be applied to any variable, independently of its underlying probability distribution, and the network's marginal probabilities can be inferred exactly (e.g., via the variable elimination algorithm, or by enumeration [77]) if the number of nodes is manageable. On the other hand, discretization of a continuous random variable inherently affects the level of detail in the results as the statistical analysis can only provide information in terms of ranges of possible values. Furthermore, results may be ambiguous at times, especially in those situations in which the true value of a continuous variable lies close to the border between two adjacent bins. These issues of detail level and result ambiguity could be circumvented by means of a finer domain discretization, under the penalty of a growing size of the nodal Conditional Probability Tables (CPT's).

In the structural problems under investigation, the physical variables (e.g., geometric parameters, material properties, or stress field) are continuous in nature. In order to convert a continuous random variable X into a discrete node, a discretization into N_b states (also called bins) ought to be performed. For each sampled node/variable X comprising

146

the Bayesian network, the statistical results herein presented correspond to a six-bin discretization ($N_b = 6$), with the bins x_b ($b = 1, \ldots, 6$) defined as follows:

$$
\begin{aligned}
x_1 &= (-\infty \ , \ \mu(X) - 2\sigma(X)] \\
x_2 &= [\,\mu(X) - 2\sigma(X) \ , \ \mu(X) - \sigma(X)] \\
x_3 &= [\,\mu(X) - \sigma(X) \ , \ \mu(X)] \\
x_4 &= [\,\mu(X) \ , \ \mu(X) + \sigma(X)] \\
x_5 &= [\,\mu(X) + \sigma(X) \ , \ \mu(X) + 2\sigma(X)] \\
x_6 &= [\,\mu(X) + 2\sigma(X) \ , \ \infty)
\end{aligned}
\tag{42}
$$

where $\mu(.)$ and $\sigma(.)$ are, respectively, the mean and the standard-deviation operators applied to the sample population of X. It is to be observed that the result of network training is independent of the nodes' level of discretization into bins, except, of course, for the size of the CPT's. In fact, the conditional probability $P(X = x | Y = y, Z = z)$ of a generic discrete node X and its discrete parents, Y and Z, is simply computed as follows:

$$
\begin{aligned}
P(X = x | Y = y, Z = z) \ &= \ \frac{P(X=x, Y=y, Z=z)}{P(Y=y, Z=z)} \\
&\approx \ \frac{\text{Number of times } X = x, \, Y = y \text{ and } Z = z \text{ in the sample population}}{\text{Number of times } Y = y \text{ and } Z = z \text{ in the sample population}}
\end{aligned}
\tag{43}
$$

where x, y and z represent, respectively, a generic possible bin in which, X, Y and Z can be, respectively. Therefore, results for a coarser discretization could be obtained by proper combination of corresponding CPT entries and nodal marginal probabilities without having to necessarily resort again to network training.

An important issue to take into consideration in the discrete approach is the case in which certain combinations of states for the parents of a child node are never observed in the sample population. As a consequence of that, referring to equation (43), the joint probability of the parent nodes $P(Y = y, Z = z)$ cannot be defined using the information at hand. Such a scenario has a twofold explanation: on the one hand, the given combination of states has not been observed yet, but it could still be assumed as possible; on the other hand, such a combination cannot ever be observed because it represents an infeasible dynamic/vibratory state for the system. Possible solutions to such a situation could be the use of a coarser binning, specifying the conditional probability $P(X = x | Y = y, Z = z)$

according to some known probability function (e.g., the uniform distribution) for those CPT entries otherwise undefined, or introducing a fictitious state x^f for the given child X, whose conditional probability equals zero or one, respectively, for observed and unobserved/infeasible combinations of the parents' states:

$$P(X = x^f | Y = y, Z = z) = \begin{cases} 1 & \text{if } P(Y = y, Z = z) \text{ undefined} \\ 0 & \text{if } P(Y = y, Z = z) \text{ defined} \end{cases} \tag{44}$$

The above definition relies on the fact that the employed statistical algorithm assigns a default value of zero to any conditional probability which cannot be computed from the training data according to equation (43). Therefore, equation (44) is intended as a possible alternative to resolve inconsistencies within a node's CPT. Of course, equation (44) could be generalized to a higher number of fictitious states, as long as their conditional probabilities consistently sum to one where requested by the definition of probability tables. Since the number of such states has no influence whatsoever on the nodes' marginal probabilities associated with the real states, but it only results in a larger-scale problem with no gain of information, only one fictitious state was added, per node, when needed.

Either approach could be adopted, each with some repercussions. On the one hand, the use of a different binning strategy, of course, causes a change in accuracy and might not necessarily resolve the underlying problem, especially when nodes at deeper network levels are involved, as more complex dynamic/structural interdependencies may be present. On the other hand, the usage of a known, yet arbitrary, probability function to handle undefined scenarios introduces an error in the marginal probabilities which spreads throughout all the states of the nodes, thus making it difficult to quantify its impact. Furthermore, the selection of another probability function will result in different amount and propagation of the error, thus calling for its selection in an appropriate fashion. The error associated with the introduction of a fictitious state, instead, can be quantified more easily because localized on that single state rather than distributed across all the bins, while its marginal Probability Mass Function (PMF) value can be discarded because it contains no meaningful information. In light of these considerations, the fictitious-bin approach seems to offer a simpler interpretation of the results as well as a lower error-wise contamination, and was,

therefore, adopted in this study. To account for the fact that the marginal probability associated with an artificial bin carries no meaning, the following normalization of the node X's marginal probability mass function has also been incorporated in the analysis:

$$\tilde{P}(X = x_i) = P(X = x_i) + \frac{P(X = x^f) \cdot P(X = x_i)}{\sum_{i=1}^{N_b} P(X = x_i)} \tag{45}$$
$$\text{where } P(X = x^f) + \sum_{i=1}^{N_b} P(X = x_i) = 1$$

where x_i $(i = 1, \ldots, N_b)$ and x^f are, respectively, the real and the fictitious state, while $\tilde{P}$ denotes the normalized marginal probability mass function. If, for a given evidence scenario, its marginal probability is not null, the presence of an artificial bin, *de facto*, induces a more conservative interpretation of the results, whereas the proportional normalization in equation (45) redistributes its probability, and allows for a more consistent comparison with other analyses (e.g., a continuous-node Bayesian network) in which no fictitious state may be present.

5.4.1 Uncertainty Quantification via Discrete Nodes

As an illustrative example, normalized-PMF results for the response inference modeled using the discrete-network approach are depicted in Figure 88 in the case of the beam structure subject to uncertainty in the test measurements, the modulus of elasticity E and the damping ratio ξ. The network response to evidence at nodes ε_3^m and ω_2^m is in agreement with what already observed for the the continuous-node network (Figure 74): evidence on node ε_3^m affects exclusively the harmonic nodes, and an observation on ω_2^m influences primarily the modal and root nodes, whereas neither one has an impact on ξ, as expected.

As observed throughout several case studies, the network may not always be capable of pinpointing the true states, either because of the chosen binning strategy or actual network limitations. On the one hand, the shifting of the bins may be able to better clarify certain inconclusive probability distributions according to which no particular state may be identified as the most probable. On the other hand, the network may be incapable of matching the true states with the highest-probability bins, even though the introduction of
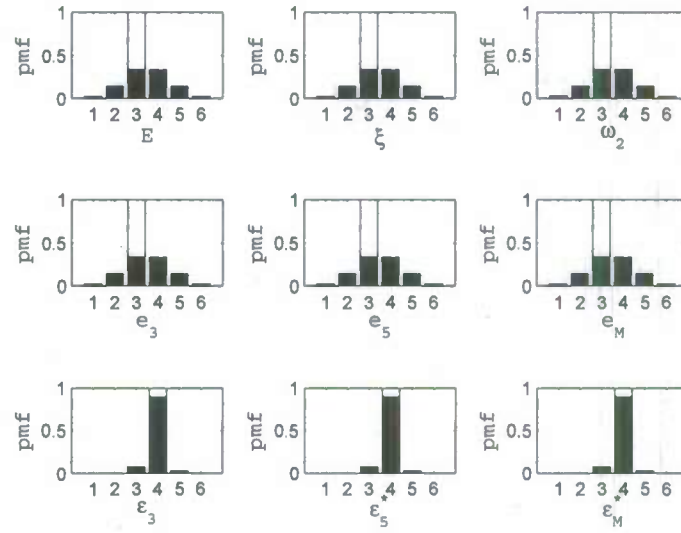
(a) Evidence at node ε_3^m
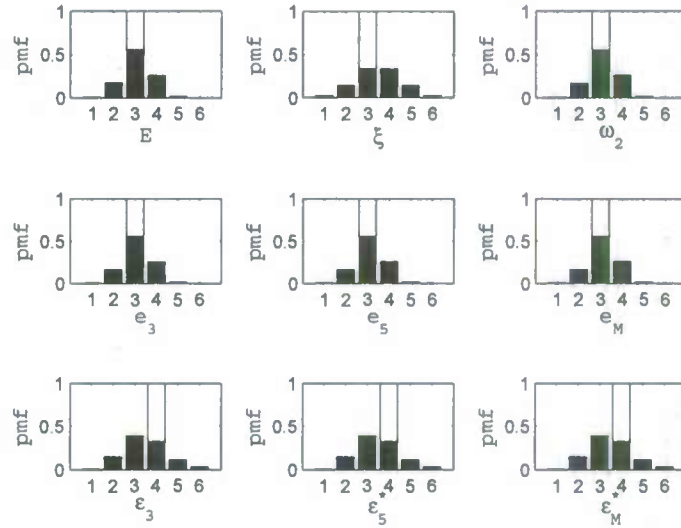
(b) Evidence at node ω_2^m

Figure 88: Beam structure: response prediction in the presence of measurement errors and uncertainty in E and ξ, for a four-gauge discrete Bayesian network.

evidence skews the probability mass functions towards the true states, thus permitting to exclude certain bins which are farther away.

In order to quantify the level of confidence to be associated with a given response estimate, a metric Π similar to δ was chosen for the discrete network as well. For each discrete node, Π_0 and Π_1 represent the rates of occurrence, respectively, that the bin with the highest posterior probability coincides with or is next to the true state. In other words, Π_0 and Π_1 are defined, respectively, in terms of zero-bin and one-bin distances between the highest-probability state and the true one. Illustrated in Figures 89 and 90 are the results for the beam and plate structures, where 1000 and 3000 true network states were respectively considered, and where observations were introduced, one at a time, first at the amplitude-measurement nodes and then at the frequency-measurement node. It can be observed that, if not coincident, the nodes' most probable bins are, at least, next to their true states in the largest majority of the cases. Therefore, in practical scenarios in which the true values of the structure's parameters and response are indeed unknown, a conservative prediction of the true states can be done by considering the highest-probability bin together with its immediate neighbors, where changes in the domain discretization can be carried out in an attempt to improve the confidence level associated with the estimated system's response. Finally, the trends shown for Π_0 in Figures 89 and 90 for the root and modal nodes are in agreement with what observed for their continuous counterparts in Figures 72 and 86. Both networks indeed exhibit similar distributions of sensitivity to evidence and perform alike when predicting the states of the nodes in question. This similarity in behavior seems to indicate that the effect of evidence depends primarily on the structure of the training data (as observed specifically for the beam system) and the topology of the network, regardless of how the random nodes are modeled. The quality of the prediction at those nodes, however, will depend on bin discretization and linear-approximation error for the discrete and the continuous network, respectively. Limitations in the identification of the correct true states, respectively as most probable bins or mean values, are also to be ascribed to the non-uniqueness of the solution at the root-node level.
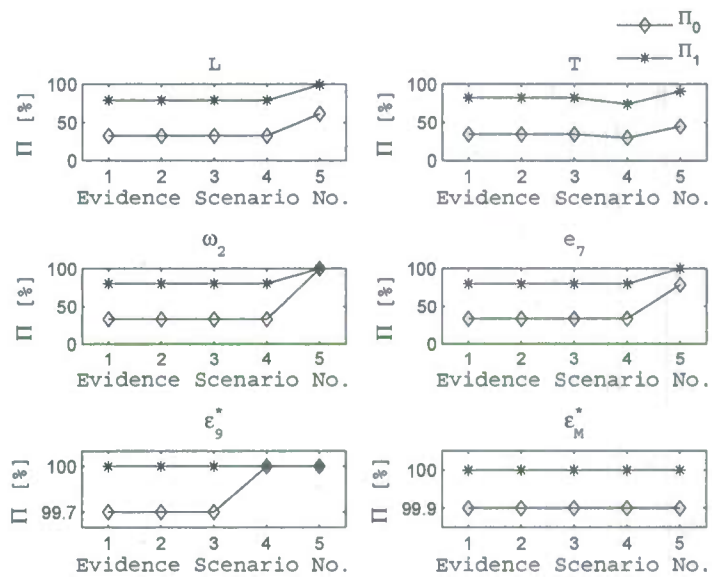
Figure 89: Beam structure: prediction rate of success Π in the presence of only geometric uncertainty in L and T, for a four-gauge discrete Bayesian network.
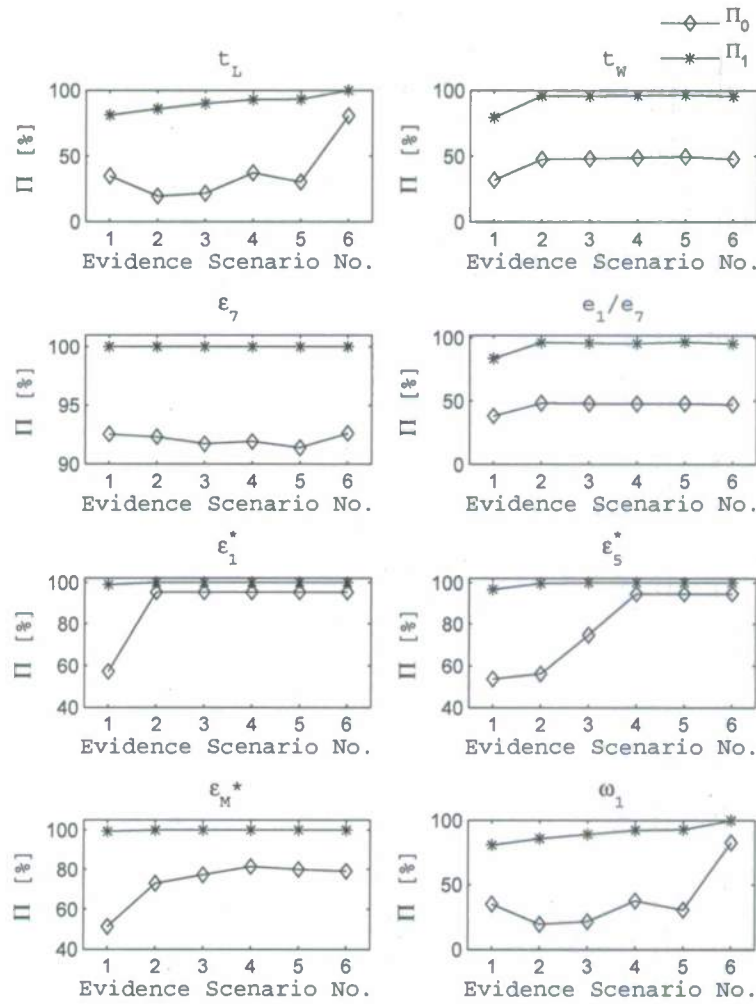
Figure 90: Plate structure: prediction rate of success Π in the presence of geometric uncertainty in L and T and measurement errors, with evidence at the amplitude and frequency measurement nodes of a five-gauge discrete Bayesian network.

5.5 *Closing the Loop: Bayesian Analysis of Experimental Data*

Thus far, the performance of the network has been tested with respect to simulated data. The statistical metric δ has been used to quantify how well a randomly-generated assigned state of a structure agrees with its Bayesian expected state, as well as to assess whether or not convergence to that true state improves and uncertainty reduces as more sensor information is made available and infused into the network.

The next and final step consists of using real experimental data as observations for the measurement nodes. For this purpose, the same experimental data analyzed in Chapter 3 were utilized, where only five out of the eleven sensors (i.e., gauges 1, 3, 5, 7, and 9) were employed to construct the 20-node Bayesian network of Figure 69. More specifically, gauges located near the plate's root and mid-length region were selected so as to include within the analysis different levels of signal-to-noise ratio, while also taking into consideration the non-linear behavior of the strain field with respect to the uncertainties modeled at the root nodes. Furthermore, given the fact that variations in the plate's geometry (specifically, length, width and thickness), as well as in its modulus of elasticity, density and damping ratio were observed to generate little or no spread in the modal strain ratios and/or the forced strains, only t_L and t_W were adopted as independent parameters so that all the modal and harmonic nodes in the Bayesian network would be characterized by a meaningful level of variability.

For a specific experiment conducted on the brass plate, results corresponding to the first resonance condition are presented in Table 21 and Figures 91-93, where the Gaussian measurement errors η of equation (40) were considered with $\sigma_\epsilon = 0.01$ and $\sigma_\omega = \alpha$ ($\alpha = 0\%,\ 1\%,\ 2\%$); also, A_ϵ and A_ω were chosen to be equal to the maximum values observed in the training data for the strain peak amplitudes and frequency, respectively. Listed in the table are the results of the correlation analysis for the modeled sensors, where gauge 7 has been chosen as reference, and where a frequency-matching-based 20% reduction in the nominal value of Young's modulus (Table 4) has been included in an effort to improve the model/test correlation. In light of the large range of possible values in the material properties of brass [65], this correction appears to be reasonable and can prove

to be beneficial when constructing equivalent numerical experiments, since the impact of evidence is inversely related to its distance from the prior information within the network. The definition of ξ_{ij} ($i = 1, 3, 5, 9$; $j = 7$) is given in equation (29), whereas ξ_{ij}^* ($i = 1, 3, 5, 9$; $j = 7$) is defined as follows:

$$\xi_{ij}^* = \frac{\bar{\varepsilon}_j^m / \bar{\varepsilon}_i^m}{\mu \left(\frac{e_j}{e_i} \right)} \tag{46}$$

As already illustrated in Figure 28, the non-unitary values of ξ_{ij} indicate that the measured response of the physical system is not always well correlated with the response computed analytically. Furthermore, correlation is not the same across the various gauge pairs, thus leading to different estimates of the system response, at other non-instrumented locations, depending on which sensors are used. As for ξ_{ij}^*, their values will depend on the amount of error present in the network, as indicated by the tabulated results obtained considering a constant error level in the amplitude measurements and varying error $N(0, \sigma_\omega)$ associated with the frequency measurement. For low error levels, the Bayesian network has less freedom to adjust itself and compensate for inconsistent evidence, whereas it is able to achieve better correlation between experimental data and analytical information as more uncertainty is present in the frequency measurement. This behavior is in agreement with what observed previously for the trend of the nodal δ's, with and without measurement errors which, *de facto*, provide the linear network with useful freedom to fit non-linear information. Furthermore, in those cases in which the final correlation is deteriorated with respect to the nominal case, the network attempts to redistribute it across all sensors, thus reducing the response variability across the various pairs of gauges. For the same reasons, the correlation for certain sensors does not vary monotonically as more observations are introduced because of the inconsistencies for which the network tries to compensate. The entire set of measurement evidence, therefore, is not only beneficial, but also necessary to guide the network towards a final expected state that agrees better with all the pieces of information.

The specific effect of observations upon the network's nodes is illustrated in Figures

91-93, where the posterior expected values are also compared against the structure's nominal geometry and response obtained either analytically or estimated through a combination with the experimental data. As previously observed, for the independent geometric parameters and the modal nodes, evidence is not always capable of univocally matching the physical system's true state with their expected values. In the case of actual experimental evidence, this problem may be further exacerbated because of modeling limitations and more uncertainty being present in the physical system than the one actually captured by the equivalent numerical experimentation. On the one hand, in fact, the simple sinusoidal variations in thickness, introduced via equation (41), are only one possible way to account for the presence of manufacturing-induced geometric uncertainty, which may be distributed or concentrated in real components. On the other hand, the same geometric uncertainties become a surrogate for other non-modeled sources of uncertainty. In light of these issues, as shown in the figures, large deviations between the nominal model and the Bayesian expected model may appear, where the final expected states of all the nodes are, however, consistent with the experimental observations provided, and lead to a reduction in the variability of the maximum-response estimate, as indicated by the results of Table 22. The confidence level associated with those expected states is, of course, a function of the amount of error embedded in the experimental information itself, whose statistical significance and accuracy is weighed against the prior information in the network according to conditional probability theory. As a final note, the network infused with evidence successfully helps explain and filter out the variability in the maximum-response estimate which inevitably originates from a host of sources of uncertainty such as low signal-to-noise ratios, inaccurate solution averaging in high-gradient regions for the strain field, or interpolation errors introduced by spectrum analyses.
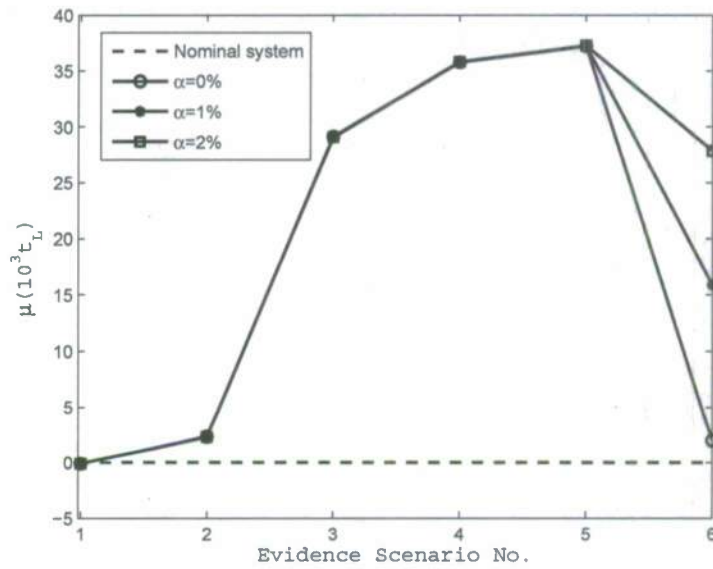
(a) Effect of evidence upon $\mu(t_L)$
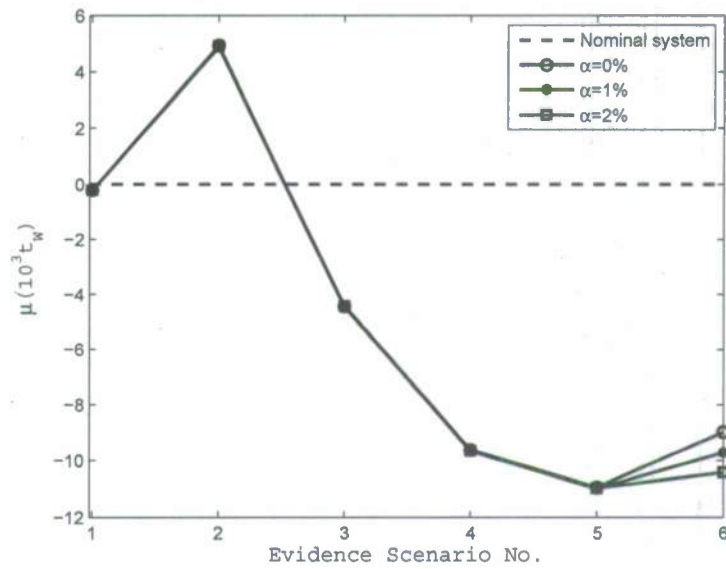
(b) Effect of evidence upon $\mu(t_W)$

Figure 91: Brass plate structure: expected values of t_L and t_W in the presence of measurement errors, for a a five-gauge Bayesian network.
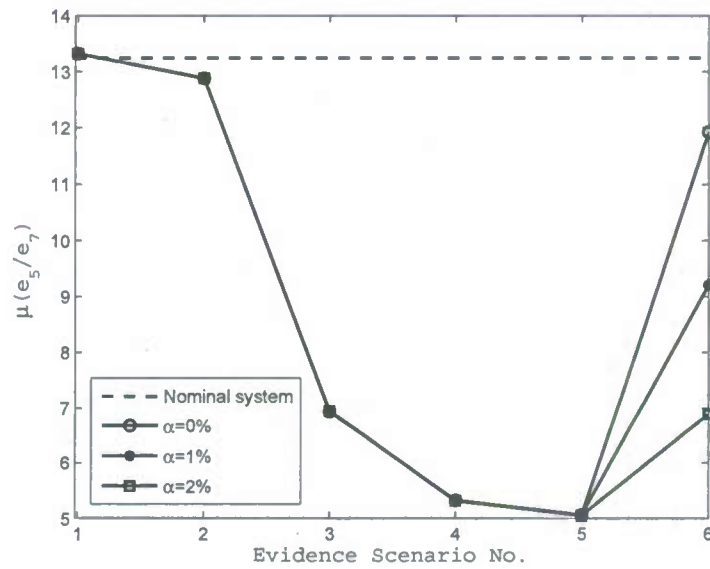
(a) Effect of evidence upon $\mu(e_5/e_7)$
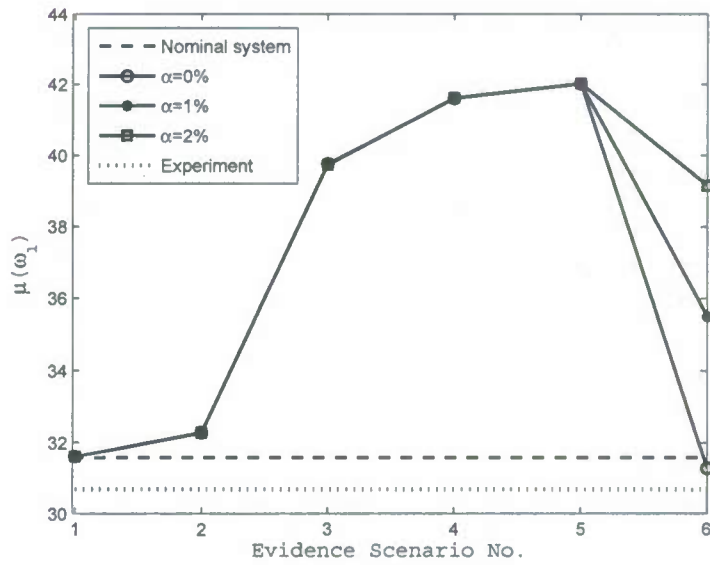
(b) Effect of evidence upon $\mu(\omega_1)$

Figure 92: Brass plate structure: expected values of e_5/e_7 and ω_1 in the presence of measurement errors, for a five-gauge Bayesian network.
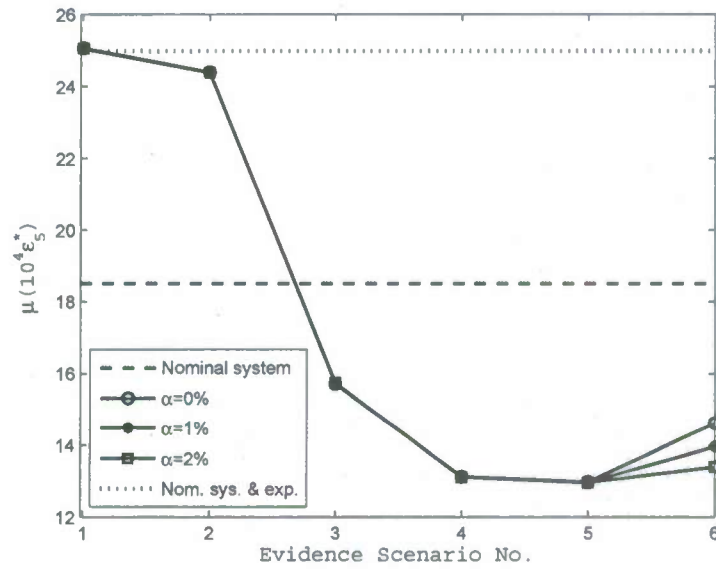
(a) Effect of evidence upon $\mu(\varepsilon_5^*)$
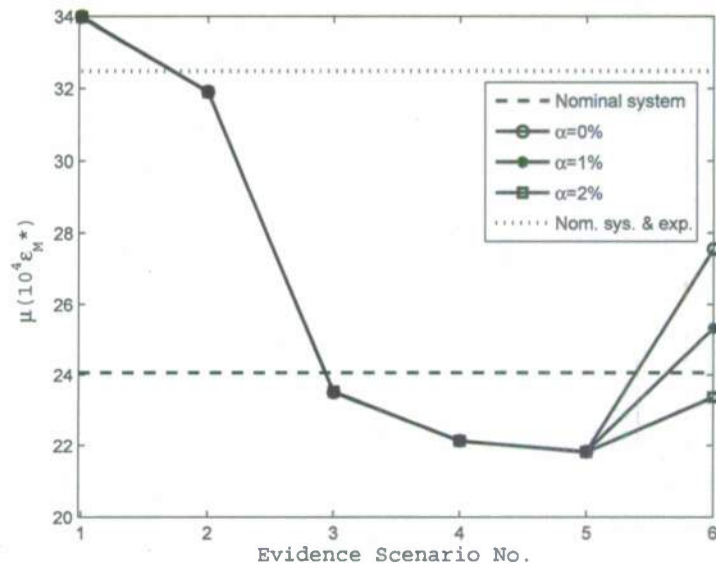
(b) Effect of evidence upon $\mu(\varepsilon_M^*)$

Figure 93: Brass plate structure: expected values of ε_5^* and ε_M^* in the presence of measurement errors, for a five-gauge Bayesian network.

Table 21: Correlation Ξ for brass plate based on gauge 7.

Experiment vs. nominal system

ξ_{17}	ξ_{37}	ξ_{57}	ξ_{97}
0.9111	0.7112	0.5180	0.5509

Experiment vs. Bayesian network

Evidence Scenario No.	Observed Nodes	ξ_{17}^*	ξ_{37}^*	ξ_{57}^*	ξ_{97}^*
1	ε_7^m	0.9949	0.9964	0.9970	0.9970
2	$\varepsilon_7^m, \varepsilon_1^m$	1.0185	1.0105	1.0038	1.0025
3	$\varepsilon_7^m, \varepsilon_1^m, \varepsilon_3^m$	1.0693	1.0516	1.2017	1.1566
4	$\varepsilon_7^m, \varepsilon_1^m, \varepsilon_3^m, \varepsilon_5^m$	1.0393	1.1067	1.2899	1.2431
5	$\varepsilon_7^m, \varepsilon_1^m, \varepsilon_3^m, \varepsilon_5^m, \varepsilon_9^m$	1.0291	1.1169	1.3573	1.2244
6 ($\alpha = 0\%$)	$\varepsilon_7^m, \varepsilon_1^m, \varepsilon_3^m, \varepsilon_5^m, \varepsilon_9^m, \omega_1^m$	0.7860	0.7088	0.5753	0.6041
6 ($\alpha = 1\%$)	$\varepsilon_7^m, \varepsilon_1^m, \varepsilon_3^m, \varepsilon_5^m, \varepsilon_9^m, \omega_1^m$	0.8675	0.8285	0.7449	0.7556
6 ($\alpha = 2\%$)	$\varepsilon_7^m, \varepsilon_1^m, \varepsilon_3^m, \varepsilon_5^m, \varepsilon_9^m, \omega_1^m$	0.9510	0.9683	0.9970	0.9617

Table 22: Maximum-response estimation results.

Estimation via nominal model and experimental data

	$i = 1$	$i = 3$	$i = 5$	$i = 7$	$i = 9$
$\frac{e_M}{e_i}\bar{\varepsilon}_i^m$	0.0030	0.0023	0.0017	0.0032	0.0018

Estimation via Bayesian expected states

		$\alpha = 0\%$	$\alpha = 1\%$	$\alpha = 2\%$
$\mu(\varepsilon_i^*)\,\mu\left(\frac{e_M}{e_7}\right)/\mu\left(\frac{e_i}{e_7}\right)$	$i = 1$	0.0028	0.0025	0.0022
	$i = 3$	0.0026	0.0025	0.0023
	$i = 5$	0.0023	0.0023	0.0024
	$i = 9$	0.0024	0.0024	0.0023
$\mu\left(\varepsilon_M^*\right)$		0.0027	0.0025	0.0023

Results corresponding to the 6th evidence scenario.

5.6 Summary

The use of a Bayesian network for the inference of the vibratory response of a structure has been investigated as a possible means to evaluate the level of confidence that can be assigned to a given estimate in the presence of various sources of uncertainty. The approach has been tested on two structures, for various sources of uncertainty, and for two different types of networks with discrete and Gaussian nodes. In terms of performance, both networks behaved similarly, as they both responded comparably to evidence infusion and pinpointed the same limitations in predicting certain nodes correctly. There are, however, distinct advantages and limitations for each of them. On the one hand, the main strength of the discrete-node approach is that it can be applied to any variable, independently of its underlying probability distribution, and marginal probabilities can be inferred exactly. The main drawback is that the discretization of a continuous random variable inherently affects the level of detail associated with the statistical analysis, since it can only provide information in terms of ranges of possible values. Higher precision can be achieved, however, by means of a finer domain discretization, under the penalty of a growth in the size of the network. On the other hand, a continuous-node Bayesian network is not affected by the problem of dimensionality of its conditional probabilities, or the corresponding loss of accuracy due to binning. Furthermore, if the nodes are assumed to have linear Gaussian distributions, an analytical solution exists for probability marginalization and propagation of evidence, and the inference process itself requires a lower computational cost compared to other distributions. Unfortunately, the more the training data is non-Gaussian, the more difficult it may become to extrapolate the information obtained through a Gaussian-node network to the actual statistical nature of the physical quantities being predicted (especially in terms of variance and higher statistical moments). Moreover, a linear Gaussian network relies on the assumption of linearity among its nodes. Of course, the higher the non-linearities, the lower the accuracy in the estimated quantities. Throughout the study, an accurate selection of the gauge locations was done so as to limit the intrinsic non-linearity in the prediction scheme. Other possible measures are to model as nodes suitable transformations of the physical quantities, or to divide the domain space of the independent parameters in smaller

regions where the linear approximation may perform better.

Overall, the use of linear Gaussian networks was found to be satisfactory for this particular type of inference in spite of the "bending" of its underlying hypotheses. Moreover, its use as a statistical surrogate model of the inference scheme permits to account for unobservable sources of uncertainty through the parameterization of alternative sources of error. Also, through the network, the accuracy of prediction can be statistically assessed via numerical experimentation, and a δ-based confidence level can be assigned to each node's estimation for any set of available node observations. The effect of evidence infusion has been proven to increase the quality of prediction in or without the presence of experiment-based errors, where the same error was noticed to become beneficial in helping estimate non-linear quantities by means of a linear model. The importance of using more test data has also been shown together with the diverse impacts that amplitude and frequency measurements have on network updating. The former may be sufficient to predict successfully the maximum response, but the latter appears to be necessary to update the system's model to a configuration consistent with the true physical component, thus improving upon their correlation.

In conclusion, for the purpose of statistically assessing the estimation of a system's vibratory response, experimental knowledge and model information have been integrated within a scheme which has demonstrated to work satisfactorily for the tested sources of uncertainty under the given set of network assumptions.

CHAPTER VI

CONCLUDING REMARKS

6.1 Summary of Research

The objective of this research has been to quantify the level of accuracy within a standard model-based estimation scheme for the calculation of the maximum vibratory response in dynamic structures. For any given physical system being investigated, this inference technique relies on two essential contributors: an analytical model of the system and actual experimentation, both of which are inevitably affected by uncertainties and errors in their results. In order to characterize the statistical interaction between these two contributors and assess the predictive accuracy of the estimation procedure, a structured statistical framework has been developed by means of a Bayesian-network representation of the inference scheme itself. This approach allows for multi-directional propagation and updating of uncertainty, as well as knowledge infusion from available sources of information at various levels of the analysis. In order to construct the Bayesian network, a simulated-experiment environment equivalent to the procedures used for actual systems was created, where equivalency in this setting implies comparable levels of results' variability and correlation between the physical system and its model. Sensitivity analyses conducted through direct propagation of uncertainty were utilized to identify key uncertainty sources to be included in the network, whether they were the true causes of the variability observed in the actual experiments or a suitable set of surrogate explanatory ones. Finally, uncertainty sources associated with system/model correlation, model parameters, and measurement sensors were modeled probabilistically and integrated in a unified fashion within the network.

The methodology was tested on two structures, a one-dimensional beam and a three-dimensional plate, with results that proved to be promising in light of the assumptions embedded in the process. In fact, in the presence of a limited set of actual test data upon which it may be difficult to draw strong statistical conclusions, the developed Bayesian

163

approach was shown to provide a means to quantify comprehensively the uncertainty in the response estimates based simply upon additional simulated experiments. The level of confidence in the estimated quantities can be assessed and quantified more satisfactorily upon the inclusion of real information from the sensors, a task that the Bayesian-network approach allows to be performed coherently.

6.2 Conclusions

The scope of this work lies within the realm of methodologies employed in building analytical models for the purpose of system performance prediction. Among the host of potential models, two main distinct categories can be identified: physics-based models and data-driven ones. On the one hand, the former are built upon first principles, and their verification and validation are usually executed as a separate task of reconciliation with appropriate test data. On the other hand, the latter consist of data-based meta-models which may not be derived from physics-based considerations. This second type of system representation lends itself easily to statistical validation, assuming that a large set of relevant data is available, which might or might not be the case.

In the presence of these distinct engineering approaches, a need has been identified for a way to integrate experimental and model information capable of addressing the intermediate scenarios and quantifying any residual uncertainty, thus combining the best features of both approaches by relying on the physics-based models and yet allowing for a statistically rigorous incorporation of the evidence into the model. As indicated by the literature review, work has already been made in the field of system identification, in which the problem of model-to-data correlation has been addressed both in a deterministic and a statistical fashion. In this work, the use of Bayesian networks has been investigated as a possible means to bridge the gap between physics-based and data-driven approaches and applied to a particular structural-dynamics application where model and experimental data are used concomitantly for the purpose of response prediction. In this context, the Bayesian network itself can be viewed as a statistical surrogate model of the prediction scheme, relating the uncertainty embedded in the estimates to the changing level of available knowledge.

The high complexity of certain structural systems makes the identification and characterization of the sources of uncertainty embedded in them an involved task which may result in a rather large state space to be modeled within a statistical framework such as a Bayesian network. Therefore, sensitivity studies and network Gaussian-linear statistics were adopted to address the dimensionality issue as well as manage the computational burden.

Sensitivity analysis was used to downsize the Bayesian network to its essential elements by means of pinpointing key explanatory factors of uncertainty and discarding quantities responsible for weak causal relationships. Case studies on these scenarios demonstrated that the presence of such quantities causes unnecessary additional topological complexity and may hamper the effect of evidence infusion because of localized insensitivity of the given network.

The assumption of linear Gaussian cause-effect relationships permits, instead, to solve for uncertainty quantification in closed form, with consequent computational savings. As with any modeling technique, however, the analytical simplifications do bound the range of applicability and validity for the proposed framework. More specifically, it may become impossible to model non-linearities using a linear network if the noise level introduced by the linearization process and due to underfitting issues outweighs the impact of any other uncertainty source; or the quantities being modeled may be highly non-Gaussian so that the first two statistical moments become insufficient to fully characterize their probabilistic nature. This loss of accuracy and information could be significantly reduced by appropriately transforming the original variables, derived from physics-based considerations, and consequently using the results of these transformations to construct the Bayesian network. As an example, the logarithmic transformation was suggested because it eliminates the source of non-linearity from the estimation product formula, and may prove beneficial if the gain in accuracy exceeds the consequent loss of probabilistic information due to treating the newly log-transformed quantities as Gaussian random variables. The use of other transformations (e.g., the Rosenblatt transformation or variations of it) could be envisioned to address this last issue.

The effect of evidence infusion led to the discovery of interesting behaviors of the network. Evidence in the form of peak frequency and peak amplitudes was chosen for this type of model-based response prediction in accordance with the existing industrial practice. The effectiveness of the propagation of evidence at a node was observed to be dependent on two important factors: the causal strength of connecting links, and the level of separation between the observed node and a given queried one. As a result of this evidence attenuation, both pieces of measured information on peak frequency and peak response amplitudes were found to be essential for a satisfactory update of the entire network. Furthermore, even with multiple inclusions of evidence, the network was not always able to pinpoint the assumed true state of all the nodes, even though its updated state was indeed consistent with the infused information. This behavior is deemed to originate primarily from the issue of solution non-uniqueness typically encountered when addressing inverse problems.

6.3 Future Work

In its present form, the proposed methodology has shown potential for a consistent and coherent statistical integration of various sources of uncertainty and information. Future endeavors should be directed towards addressing its limitations and relaxing the embedded assumptions so as to extend the range of applicability and improve the quantification of uncertainty. More specifically, important directions for future research are:

- To inspect further the use of variable transformations and assess them in terms of residual non-linearities in the model and nature of the transformed quantities, whose probabilistic interpretation may become more difficult;

- To address the problem of solution non-uniqueness, for which task additional sources of information ought to be identified and suitably integrated within the current network topology. The search for additional evidence may call for a concomitant use of numerical results and observations associated with different resonance conditions;

- To investigate the potential use of the developed statistical framework for model updating, with the understanding that some of the uncertainties modeled within the

166

network may be in substitution of unobservable ones;

- To extend the current approach to those scenarios in which more than one mode shape contributes to the forced response in the frequency range of interest. This is the case for cyclic structures characterized by the existence of double modes. A question is raised as to whether the coefficients of modal participation should be computed separately or included within the Bayesian network as additional random variables, with consequent need for other evidence;

- To automate the sensitivity analysis and the selection of the gauges to be included in the network for a possible online implementation within current industry practices. For this purpose, a database of *ad hoc* simulated experiments may be needed to reduce the long computational time associated with designs of experiments on complex systems. Alternatively, as already suggested in the literature, generic databases could be generated together with appropriate scaling functions to link them to the specific test/in-field conditions of interest;

- To explore the inclusion of more exhaustive models of the instrumentation-related uncertainties (e.g., acquisition and data-processing errors) so as to account for them as individual interacting entities rather than condensing them into a single measurement node per sensor. This could lead to potential usages of the information acquired through this process for subsequent test setup optimization; and

- To assess the proposed Bayesian response prediction scheme in the case of turbine engine blades as well as other structures with more complex geometry.

In tackling these and other interesting research ideas, however, attention is to be given to the potential issues of network increasing complexity and higher demand for more pieces of evidence, which ought to be statistically uncorrelated so as not to bias the Bayesian inference process.

REFERENCES

[1] ALLEMANG, R. J. and BROWN, D. L., "A correlation coefficient for modal vector analysis," in *Proceedings of the 1st International Modal Analysis Conference and Exhibit*, (Orlando, FL, USA), pp. 110–116, 1982.

[2] ANSYS® INC., *Theory reference. ANSYS Release 10.0.* SAS IP, Inc., © 2005.

[3] ARAUJO, M. I. and DE BRAGANA PEREIRA, B., "A comparison of Bayes factors for separated models: some simulation results," *Communications in Statistics - Simulation and Computation*, vol. 36, no. 2, pp. 297–309, 2007.

[4] ARNOLD, S., "New techniques to quantify HCF margins demonstrated during accelerated mission testing," in *Proceedings of the 39th AIAA Joint Propulsion Conference and Exhibit*, (Huntsville, AL, USA), July 20-23 2003.

[5] ASTROM, K. J. and EYKHOFF, P., "System identification - a survey," *Automatica*, vol. 7, no. 2, pp. 123–62, 1971.

[6] BECK, J. L. and KATAFYGIOTIS, L. S., "Updating models and their uncertainties. I: Bayesian statistical framework," *Journal of Engineering Mechanics*, vol. 124, pp. 455–461, April 1998.

[7] BEN-HAIM, Y., "Uncertainty, probability, and information-gaps," *Reliability Engineering and System Safety*, no. 85, pp. 249–266, 2004.

[8] BENFIELD, W. A. and HRUDA, R. F., "Vibration analysis of structures by component mode substitution," *AIAA Journal*, vol. 9, no. 7, pp. 1255–1261, 1971.

[9] BLADH, R., CASTANIER, M., and PIERRE, C., "Reduced order modeling and vibration analysis of mistuned bladed disk assemblies with shrouds," *Journal of Engineering for Gas Turbines and Power*, vol. 121, pp. 515–522, July 1999.

[10] BLADH, R., CASTANIER, M., and PIERRE, C., "Component-based reduced modeling techniques for mistuned bladed disks, part I: Theoretical models," *Journal of Engineering for Gas Turbines and Power*, vol. 123, pp. 89–99, January 2001.

[11] BLADH, R., CASTANIER, M., and PIERRE, C., "Component-based reduced modeling techniques for mistuned bladed disks, part II: Application," *Journal of Engineering for Gas Turbines and Power*, vol. 123, pp. 100–108, January 2001.

[12] BOUDALI, H. and BECHTA-DUGAN, J., "A continuous-time Bayesian network reliability modeling, and analysis framework," *IEEE Transactions on Reliability*, vol. 55, pp. 86–97, March 2006.

[13] BREESE, J. S., HORVITZ, E. J., PEOT, M. A., GAY, R., and QUENTIN, G. H., "Automated decision-analytic diagnosis of thermal performance in gas turbines," in *Proceedings of the ASME Turbo Expo 1992 Conference*, (Cologne, Germany), June 1-4 1992. ASME Paper No. 92-GT-399.

[14] Brown, J., Slater, J., and Grandhi, R., "Probabilistic analysis of geometric uncertainty effects on blade modal response," in *Proceedings of the ASME Turbo Expo 2003 Conference*, (Atlanta, GA, USA), pp. 247–255, June 16-19 2003.

[15] Campbell, M. and Crawley, E., "Development of structural uncertainty models," *Journal of Guidance, Control and Dynamics*, vol. 20, pp. 841–849, September-October 1997.

[16] Capiez-Lernout, E. and Soize, C., "Nonparametric modeling of random uncertainties for dynamic response of mistuned bladed disks," *Journal of Engineering for Gas Turbines and Power*, vol. 126, pp. 610–618, July 2004.

[17] Capiez-Lernout, E., Soize, C., and Lombard, J., "Blade manufacturing tolerances definition for a mistuned industrial bladed disk," in *Proceedings of the ASME Turbo Expo 2004 Conference*, (Vienna, Austria), pp. 307–316, June 14-17 2004.

[18] Castanier, M. and Pierre, C., "Using intentional mistuning in the design of turbomachinery rotors," *AIAA Journal*, vol. 40, pp. 2077–2086, October 2002.

[19] Chang, C., Chang, T., and Xu, Y., "Adaptive neural networks for model updating of structures," *Smart Materials and Structures*, vol. 9, no. 1, pp. 59–68, 2000.

[20] Chassiakos, A. G. and Masri, S. F., "Identification of structural systems by neural networks," *Mathematics and Computers in Simulation*, vol. 40, no. 5-6, pp. 637–56, 1996.

[21] Ching, J. and Beck, J. L., "Bayesian analysis of the phase II IASC-ASCE structural health monitoring experimental benchmark data," *Journal of Engineering Mechanics*, vol. 130, pp. 1233–1244, 2004.

[22] Ching, J., Muto, M., and Beck, J. L., "Structural model updating and health monitoring with incomplete modal data using gibbs sampler," *Computer-Aided Civil Infrastructure Engineering*, vol. 21, no. 4, pp. 242–257, 2006.

[23] De Figueiredo, L. H. and Stolfi, J., "Affine arithmetic: concepts and applications," *Numerical Algorithms*, vol. 37, no. 1-4, pp. 147–58, 2004.

[24] Der Kiureghian, A., "Bayesian analysis of model uncertainty in structural reliability," in *Lecture Notes in Engineering*, no. 61, (Berkeley, CA, USA), pp. 211–221, 1991.

[25] Elseifi, M. A., "Bayesian models for the reliability analysis of composite plates," in *Proceedings of the 45th AIAA/ASME/ASCE/AHS/ASC Structures, Structural Dynamics and Material Conference*, (Palm Springs, CA, USA), pp. 3458–3467, April 19-22 2004.

[26] Ewins, D. J., *Modal Testing: Theory, Practice, and Application, 2nd Edition*. Baldock, Hertfordshire, England: Research Studies Press, 2000.

[27] Experimental Design & Analysis Solution (EDAS®) Inc., "Gagemap II and EDAS-DV." Software Packages.

[28] EYKHOFF, P., *System Identification: Parameter and State Estimation.* New York, NY, USA: John Wiley & Sons, Inc., 1974.

[29] FONSECA, J. R., FRISWELL, M. I., MOTTERSHEAD, J. E., and LEES, A. W., "Uncertainty identification by the maximum likelihood method," *Journal of Sound and Vibration*, vol. 288, no. 3, pp. 587–599, 2005.

[30] FRISWELL, M. I., FONSECA, J. R., MOTTERSHEAD, J. E., and LEES, A. W., "Quantification of uncertainty using inverse methods," in *Proceedings of the 45th AIAA/ASME/ASCE/AHS/ASC Structures, Structural Dynamics and Materials Conference*, vol. 3, (Palm Springs, CA, USA), pp. 1756–1763, April 19-22 2004.

[31] FRISWELL, M. I., PRELLS, U., and PENNY, J. E. T., "Determining uncertainty bounds for eigenvalues," in *Proceedings of the 2004 International Conference on Noise and Vibration Engineering*, (Leuven, Belgium), pp. 3055–3064, September 20-22 2004.

[32] GEYSKENS, P., DER KIUREGHIAN, A., and MONTEIRO, P., "Bayesian prediction of elastic modulus of concrete," *Journal of Structural Engineering*, vol. 124, no. 1, pp. 89–95, 1998.

[33] GHANEM, R., "Ingredients for a general purpose stochastic finite elements implementation," *Computer Methods in Applied Mechanics and Engineering*, vol. 168, no. 1, pp. 19–34, 1999.

[34] GHANEM, R. and RED-HORSE, J., "Propagation of probabilistic uncertainty in complex physical systems using a stochastic finite element approach," *Physica D: Nonlinear Phenomena*, vol. 133, no. 1-4, pp. 137–144, 1999.

[35] GRIFFIN, J. H., "On predicting the resonant response of bladed disk assemblies," *Journal of Engineering for Gas Turbines and Power*, vol. 110, pp. 45–50, January 1988.

[36] GRIFFIN, J. H. and HOOSAC, T. M., "Model development and statistical investigation of turbine blade mistuning," *ASME Journal of Vibration, Acoustics, Stress and Reliability in Design*, vol. 106, pp. 204–211, April 1984.

[37] HABER, R. and UNBEHAUEN, H., "Structure identification of nonlinear dynamic systems. A survey on input/output approaches," *Automatica*, vol. 26, no. 4, pp. 651–677, 1990.

[38] HARRIS, F., "On the use of windows for harmonic analysis with the discrete fourier transform," *Proceedings of the IEEE*, vol. 66, pp. 51–83, January 1978.

[39] HASSELMAN, T. K., "Structural uncertainty in dynamic analysis," in *SAE Transactions*, 1981. Paper No. 811049.

[40] HASSELMAN, T. K., "Quantification of uncertainty in structural dynamic models," *Journal of Aerospace Engineering*, vol. 14, pp. 158–165, October 2001.

[41] HASSELMAN, T. K., ANDERSON, M. C., and GAN, W., "Principal components analysis for nonlinear model correlation, updating and uncertainty evaluation," in *Proceedings of the 16th International Modal Analysis Conference*, vol. 1, (Santa Barbara, CA, USA), pp. 644–651, February 2-5 1998.

[42] HASSELMAN, T. K., ANDERSON, M. C., and LI, X., "Effect of modal test statistics on modeling uncertainty and model updating," in *Proceedings of the 41st AIAA/ASME/ASCE/AHS/ASC Structures, Structural Dynamics and Materials Conference*, vol. 3, pp. 19–25, April 3-8 2000.

[43] HASSELMAN, T. K. and CHROSTOWSKI, J., "Statistical analysis of modeling error in structural dynamic systems," in *Collection of Technical Papers of the AIAA/ASME/ASCE/AHS Structures, Structural Dynamics and Materials Conference*, (Long Beach, CA, USA), pp. 1945–1951, 1990.

[44] HASSELMAN, T. K., YAP, K. C., WATHUGALA, G. W., and ANDERSON, M. C., "A top-down method for uncertainty quantification and predictive accuracy assessment," in *Proceedings of the 46th AIAA/ASME/ASCE/AHS/ASC Structures, Structural Dynamics and Materials Conference*, vol. 2, April 18-21 2005.

[45] HASSELMAN, T. K., ZIMMERMAN, D. C., and HERENDEEN, D. L., "An integrated FEA software capability for dynamic model validation and verification," in *Proceedings of the 40th AIAA/ASME/ASCE/AHS/ASC Structures, Structural Dynamics and Materials Conference*, vol. 4, (St. Louis, MO, USA), pp. 2970–2979, April 12-15 1999.

[46] HEMEZ, F. and DOEBLING, S., "A validation of Bayesian finite element model updating for linear dynamics," in *Proceedings of the 17th International Modal Analysis Conference*, (Kissimmee, FL, USA), pp. 1545–1555, February 8-11 1999.

[47] HEMEZ, F. and DOEBLING, S., "Model validation and uncertainty quantification," in *Proceedings of the 19th International Modal Analysis Conference*, (Kissimmee, FL, USA), pp. 1153–1158, February 5-8 2001.

[48] HURTY, W. C., "Dynamic analysis of structural systems using component modes," *AIAA Journal*, vol. 3, no. 4, pp. 678–685, 1965.

[49] KATAFYGIOTIS, L. S. and BECK, J. L., "Updating models and their uncertainties. II: Model identifiability," *Journal of Engineering Mechanics*, vol. 124, pp. 463–467, April 1998.

[50] KERSCHEN, G., WORDEN, K., VAKAKIS, A. F., and GOLINVAL, J. C., "Past, present and future of nonlinear system identification in structural dynamics," *Mechanical Systems and Signal Processing*, vol. 20, no. 3, pp. 505–592, 2006.

[51] KOZIN, F. and NATKE, H. G., "System identification techniques," *Structural Safety*, vol. 3, no. 3-4, pp. 269–316, 1986.

[52] KRUSE, M. and PIERRE, C., "Forced response of mistuned bladed disks using reduced-order modeling," *Collection of Technical Papers of the AIAA/ASME/ASCE/AHS/ASC Structures, Structural Dynamics and Materials Conference*, vol. 4, pp. 1938–1950, 1996.

[53] LALLEMAND, B., CHERKI, A., TISON, T., and LEVEL, P., "Fuzzy modal finite element analysis of structures with imprecise material properties," *Journal of Sound and Vibration*, vol. 220, pp. 353–364, February 1999.

[54] LALLEMAND, B., PLESSIS, G., TISON, T., and LEVEL, P., "Modal behaviour of structures defined by imprecise geometric parameters," in *Proceedings of the 18th International Modal Analysis Conference*, (San Antonio, TX, USA), pp. 1422–1428, February 7-10 2000.

[55] LAM, H. F., KATAFYGIOTIS, L. S., and MICKLEBOROUGH, N. C., "Application of a statistical model updating approach on phase I of the IASC-ASCE structural health monitoring benchmark study," *Journal of Engineering Mechanics*, vol. 130, pp. 34–48, January 2004.

[56] LEVIN, R. I. and LIEVEN, A. J., "Dynamic finite element model updating using simulated annealing and genetic algorithm," *Journal of Mechanical System and Signal Processing*, vol. 12, no. 1, pp. 91–120, 1998.

[57] LIN, Y. K., KOZIN, F., WEN, Y. K., CASCIATI, F., SCHUEELLER, G. I., DER KIUREGHIAN, A., DITLEVSEN, O., and VANMARCKE, E. H., "Methods of stochastic structural dynamics," *Structural Safety*, vol. 3, no. 3-4, pp. 167–194, 1986.

[58] LINK, M. and MIODRAG, C., "Combining adaptive FE mesh refinement and model parameter updating," in *Proceedings of the 18th International Modal Analysis Conference*, (San Antonio, TX, USA), pp. 584–588, February 7-10 2000.

[59] MACNEAL, R. H., HARDER, R. L., and MASON, J. B., *NASTRAN Cyclic Symmetry Capability, NASTRAN: Users' Exper.* MSC Software Corporation, September 1973. NASA TM X-2893.

[60] MAHADEVAN, S. and REBBA, R., "Model predictive capability assessment under uncertainty," in *Proceedings of the 46th AIAA/ASME/AHS/ASC Structures, Structural Dynamics and Materials Conference*, (Austin, TX, USA), April 18-21 2005.

[61] MAHADEVAN, S. and REBBA, R., "Validation of reliability computational models using Bayes networks," *Reliability Engineering and System Safety*, vol. 87, pp. 223–232, February 2005.

[62] MANSON, G., "Calculating frequency response functions for uncertain systems using complex affine analysis," *Journal of Sound and Vibration*, vol. 288, no. 3, pp. 487–521, 2005.

[63] MARES, C., MOTTERSHEAD, J. E., and FRISWELL, M. I., "Stochastic model updating: part 1 - theory and simulated example," *Mechanical Systems and Signal Processing*, vol. 20, no. 7, pp. 1674–1695, 2006.

[64] MARUGABANDHU, P. and H., G. J., "A reduced-order model for evaluating the effect of rotational speed on the natural frequencies and mode shapes of blades," *Journal of Engineering for Gas Turbines and Power*, vol. 125, pp. 772–776, July 2003.

[65] MATWEB, *Overview of materials for Brass.* Automation Creations, Inc. © 1996-2008, Blacksburg, VA, USA. Last retrieved on April 20, 2008 from http://www.matweb.com.

[66] MEIROVITCH, L., *Analytical Methods in Vibrations.* New York, NY, USA: Macmillan, 1967.

[67] MELCHERS, R. E., *Structural Reliability Analysis and Prediction, 2nd Edition*. New York, NY, USA: Wiley, 1999.

[68] MOORE, R. E., *Methods and Applications of Interval Analysis*. Philadelphia, PA, USA: SIAM, 1979.

[69] MORGAN, B. J. T., *Elements of Simulation*. New York, NY, USA: Chapman & Hall, 1984.

[70] MOTTERSHEAD, J. E. and FRISWELL, M. I., "Model updating in structural dynamics: a survey," *Journal of Sound and Vibration*, vol. 167, pp. 347–375, October 1993.

[71] MOTTERSHEAD, J. E., MARES, C., JAMES, S., and FRISWELL, M. I., "Stochastic model updating: part 2 - application to a set of physical structures," *Mechanical Systems and Signal Processing*, vol. 20, no. 8, pp. 2171–2185, 2006.

[72] MOYROUD, F., JACQUET-RICHARDET, G., and FRANSSON, T., "A comparison of two finite element reduction techniques for mistuned bladed disks," in *Proceedings of the ASME Turbo Expo 2000 Conference*, (Munich, Germany), May 8-11 2000.

[73] MURPHY, K., "The Bayes net toolbox for matlab," *Computing Science and Statistics*, vol. 33, 2001.

[74] NELLES, O., *Nonlinear System Identification: from Classical Approaches to Neural Networks and Fuzzy Models*. New York, NY, USA: Springer, 2001.

[75] NICHOL, K., "Numerical strain gage representation," in *Proceedings of the 39th AIAA/ASME/ASCE/AHS/ASC Structures, Structural Dynamics and Materials Conference and Exhibit*, (Long Beach, CA, USA), pp. 198–203, April 20-23 1998.

[76] NICHOL, K. L., SENSMEIER, M. D., and TIBBALS, T. F., "Assessment of turbine engine structural integrity using the structural dynamic response analysis code (SDRAC)," in *Proceedings of the ASME International Gas Turbine and Aeroengine Congress and Exhibition*, (Indianapolis, IN, USA), June 7-10 1999.

[77] NORVIG, P. and STUART, R., *Artificial Intelligence: A modern Approach, 2nd Edition*. Prentice Hall Series in Artificial Intelligence, Upper Saddle River, NJ, USA: Pearson Education, Inc., 2003.

[78] OTTARSSON, G. S., CASTANIER, M., and PIERRE, C., "A reduced-order modeling technique for mistuned bladed disks," *Journal of Vibration and Acoustics*, vol. 119, pp. 439–447, July 1997.

[79] PEARL, J., *Probabilistic Reasoning in Intelligent Systems*. San Mateo, CA, USA: Morgan Kauffman, 1998.

[80] PENG, Y. and REGGIA, J. A., *Abductive Inference Models for Diagnostic Problem Solving*. New York, NY, USA: Springer-Verlag, 1990.

[81] PETYT, M., *Introduction to Finite Element Vibration Analysis*. Cambridge, UK: Cambridge University Press, 1990.

[82] QINGGUO, F., AIQUN, L., and CHANGQING, M., "Dynamic finite element model updating using meta-model and genetic algorithm," *Journal of Southeast University*, vol. 22, pp. 213–217, June 2006.

[83] QIU, Z., WANG, X., and FRISWELL, M. I., "Eigenvalue bounds of structures with uncertain-but-bounded parameters," *Journal of Sound and Vibration*, vol. 282, no. 1-2, pp. 297–312, 2005.

[84] REBBA, R., MAHADEVAN, S., and HUANG, S., "Inclusion of uncertainty quantification in model verification and validation," in *Proceedings of Foundations '04: A Workshop for V&V in the 21st Century*, (Arizona State University, Tempe, AZ, USA), October 13-15 2004.

[85] REBBA, R., MAHADEVAN, S., and ZHANG, R., "Validation of uncertainty propagation models," in *Proceedings of the 44th AIAA/ASME/ASCE/AHS Structures, Structural Dynamics and Materials Conference*, vol. 6, (Norfolk, VA, USA), pp. 4671–4678, April 7-10 2003.

[86] SANDERS, A. J. and FLEETER, S., "Experimental investigation of rotor-inlet guide vane interactions in transonic axial-flow compressor," *Journal of Propulsion and Power*, vol. 16, no. 3, pp. 421–430, 2000.

[87] SEINTURIER, E. and ET AL., "Turbine mistuned forced response prediction comparison with experimental results," in *Proceedings of the ASME Turbo Expo 2002 Conference*, (Amsterdam, The Netherlands), pp. 943–952, June 3-6 2002.

[88] SEINTURIER, E. and ET AL., "Forced response prediction methodology for the design of HP compressors bladed disks," in *Proceedings of the ASME Turbo Expo 2004 Conference*, vol. 6, (Vienna, Austria), pp. 317–326, June 14-17 2004.

[89] SENSMEIER, M. D. and NICHOL, K. L., "Optimum placement of sensors for vibration measurements on turbine engine blades," in *Proceedings of the 39th AIAA/ASME/ASCE/AHS/ASC Structures, Structural Dynamics and Materials Conference and Exhibit*, (Long Beach, CA, USA), pp. 1315–1320, April 20-23 1998.

[90] SINHA, A., "Computation of the statistics of forced response of a mistuned bladed disk assembly via polynomial chaos," in *Proceedings of the ASME Turbo Expo 2003 Conference*, (Atlanta, GA, USA), pp. 287–297, June 16-19 2003.

[91] SINHA, A., "Statistics of the peak maximum amplitude of the forced response of a mistuned bladed disk," in *Proceedings of the ASME Turbo Expo 2005 Conference*, (Reno-Tahoe, NV, USA), June 6-9 2005.

[92] SIU, N. O. and KELLY, D. L., "Bayesian parameter estimation in probabilistic risk assessment," *Reliability Engineering and System Safety*, vol. 62, no. 1-2, pp. 89–116, 1998.

[93] SOIZE, C., "A non-parametric model of random uncertainties for reduced matrix models in structural dynamics," *Probabilistic Engineering Mechanics*, vol. 15, no. 3, pp. 277–294, 2000.

[94] SOIZE, C., "A comprehensive overview of a non-parametric approach of model uncertainties for predictive models in structural dynamics," *Journal of Sound and Vibration*, vol. 288, pp. 623–652, December 2005.

[95] STANDER, N., CRAIG, K. J., MULLERSCHON, H., and REICHERT, R., "Material identification in structural optimization using response surfaces," *Structural and Multidisciplinary Optimization*, vol. 29, no. 2, pp. 93–102, 2005.

[96] TAKEWAKI, I. and BEN-HAIM, Y. Y., "Info-gap robust design with load and model uncertainties," *Journal of Sound and Vibration*, vol. 288, no. 3, pp. 551–70, 2005.

[97] THE MATHWORKS™ INC. © 1994-2008, "Matlab." Software Package.

[98] THOMAS, D. L., "Dynamics of rotationally periodic structures," *International Journal for Numerical Methods in Engineering*, vol. 14, no. 1, pp. 81–102, 1979.

[99] TIBBALS, T. F., BAPTY, T. A., and ABBOTT, B. A., "CADDMAS: A real time parallel system for dynamic data analysis," in *Proceedings of the ASME International Gas Turbine and Aeroengine Congress and Exposition*, (The Hague, Netherlands), pp. 1–11, June 13-16 1994.

[100] TIBBALS, T. F., SENSMEIER, M. D., NICHOL, K. L., STONER, A., and BIEGL, C., "Model integrated testing for durability assessment of turbine engines," in *Proceedings of the ITEA Testing and Evaluation and Science and Technology: Forging Partnerships for the Future of Aerospace Workshop*, (University of Tennessee Space Institute, Tullahoma, TN, USA), October 12-15 1999.

[101] UNBEHAUEN, H., "System identification methods using parameter estimation: A survey," in *Annual Review in Automatic Programming*, vol. 12, (Berlin, East Germany), pp. 69–81, 1985.

[102] UNBEHAUEN, H. and RAO, G. P., "Continuous-time approaches to system identification. a survey," *Automatica*, vol. 26, no. 1, pp. 23–35, 1990.

[103] VAN NOORTWIJK, J. M., KALK, H. J., DUITS, M. T., and H., C. E., "The use of Bayes factors for model selection in structural reliability," in *Proceedings of the 8th International Conference on Structural Safety and Reliability*, (Newport Beach, CA, USA), June 17-21 2001.

[104] VANIK, M. W., BECK, J. L., and AU, S. K., "A Bayesian probabilistic approach to structural health monitoring," *Journal of Engineering Mechanics*, vol. 126, pp. 738–745, 2000.

[105] WEI, S. T. and PIERRE, C., "Localization phenomena in mistuned assemblies with cyclic symmetry, part I: Free vibrations," *Journal of Vibration, Acoustics, Stress, and Reliability in Design*, vol. 110, pp. 429–438, October 1988.

[106] WEI, S. T. and PIERRE, C., "Localization phenomena in mistuned assemblies with cyclic symmetry, part II: Forced vibrations," *Journal of Vibration, Acoustics, Stress, and Reliability in Design*, vol. 110, pp. 439–449, October 1988.

[107] WORDEN, K., MANSON, T. M., LORD, T. M., and FRISWELL, M. I., "Some observations on uncertainty propagation through a simple nonlinear system," *Journal of Sound and Vibration*, vol. 288, no. 3, pp. 601–621, 2005.

[108] YUEN, K., BECK, J., and KATAFYGIOTIS, L., "Unified probabilistic approach for model updating and damage detection," *Journal of Applied Mechanics*, vol. 73, pp. 555–564, July 2006.

[109] YUEN, K., BECK, J. L., and AU, S. K., "Structural damage detection and assessment by adaptive markov chain monte carlo simulation," *Structural Control and Health Monitoring*, vol. 11, no. 4, pp. 327–347, 2004.

[110] YUEN, K. and KATAFYGIOTIS, L., "Bayesian modal updating using complete input and incomplete response noisy measurements," *Journal of Engineering Mechanics*, vol. 128, pp. 340–350, March 2002.

[111] YUEN, K. and KATAFYGIOTIS, L. S., "Model updating using noisy response measurements without knowledge of the input spectrum," *Earthquake Engineering and Structural Dynamics*, vol. 34, no. 2, pp. 167–187, 2005.

[112] YUEN, K. V., AU, S. K., and BECK, J. L., "Two-stage structural health monitoring approach for phase I benchmark studies," *Journal of Engineering Mechanics*, vol. 130, pp. 16–33, 2004.

[113] ZADEH, L. A., "Fuzzy sets," *Information and Control*, vol. 8, pp. 338–353, June 1965.

[114] ZHANG, R. and MAHADEVAN, S., "Bayesian methodology for reliability model acceptance," *Reliability and System Safety*, vol. 80, pp. 95–103, April 2003.

VITA

Giorgio M. Calanni Fraccone was born and raised in Italy, before venturing to Luxembourg and the United States of America. Besides this doctorate (2008), he holds a Master of Science degree in Mechanical and Aerospace Engineering (2001) from the University of Virginia in Charlottesville, Virginia, USA; a *Laurea* in Aerospace Engineering (2004) from Politecnico di Milano in Milan, Italy; and a Master of Science in Aerospace Engineering (2004) from the Georgia Institute of Technology in Atlanta, Georgia, USA.

Giorgio never dreamed of becoming an astronaut, but his passion lies in space applications and his research interests are in the realms of structural analysis, vibrations of structures, satellite design and space mission analysis, aerospace systems design methodologies, system dynamics modeling, statistical methods and multidisciplinary optimization techniques.